

**U.S. DEPARTMENT OF COMMERCE
National Technical Information Service**

N79-29832

**CELFE: COUPLED EULERIAN-LAGRANGIAN FINITE
ELEMENT PROGRAM FOR HIGH VELOCITY IMPACT
PART I THEORY AND FORMULATION**

C. H. Lee

Lockheed Missiles & Space Company, Inc.

January 1978

NASA CR 159395
LMSC-HREC TR D497204-1

**CELFE: COUPLED EULERIAN-LAGRANGIAN
FINITE ELEMENT PROGRAM
FOR HIGH VELOCITY IMPACT**
PART I THEORY AND FORMULATION

C. H. Lee

**LOCKHEED MISSILES & SPACE COMPANY, INC.
HUNTSVILLE RESEARCH & ENGINEERING CENTER**

REPRODUCED BY
NATIONAL TECHNICAL
INFORMATION SERVICE
U.S. DEPARTMENT OF COMMERCE
SPRINGFIELD, VA. 22161

prepared for

NATIONAL AERONAUTICS AND SPACE ADMINISTRATION

**NASA Lewis Research Center
Contract NAS3-18908**

C. C. Chamis, Project Manager

(NASA-CR-159395) CELFE: COUPLED HC AD8/MF A01 N79-29832
EULERIAN-LAGRANGIAN FINITE ELEMENT PROGRAM
FOR HIGH VELOCITY IMPACT. PART 1: THEORY
AND FORMULATION Final Report, Jun. 1975 - Unclas
Sep. 1977 (Lockheed Missiles and Space Co.) G3/61 29089

1 Report No NASA CR 159395	2. Government Accession No	3 Recipient's Catalog No	
4. Title and Subtitle CELFE: Coupled Eulerian Lagrangian Finite Element Program for High Velocity Impact, Part I Theory and Formulation		5 Report Date January 1978	
		6 Performing Organization Code	
7 Author(s) C. H. Lee		8. Performing Organization Report No. LMSC-HREC TR D497204-1	
9. Performing Organization Name and Address Lockheed Missiles and Space Company, Inc. Huntsville Research and Engineering Center P. O. Box 1103 Huntsville, AL 18908		10 Work Unit No.	
12. Sponsoring Agency Name and Address National Aeronautics and Space Administration Washington DC 20546		11. Contract or Grant No NAS 3-18908	
15 Supplementary Notes Project Manager, C. C. Chamis Materials and Structures Division NASA Lewis Research Center Cleveland, OH 44135		13. Type of Report and Period Covered Final 7-75 to 12-77	
16. Abstract <p>The theoretical formulation of the Coupled Eulerian-Lagrangian Finite Element (CELFE) computer program for high velocity impact analysis is described. The formulation includes the development of a 3-D finite element program capable of simulating the dynamic behavior in the vicinity of the impact point, together with predicting the dynamic response in the remaining part of the structural component subjected to high velocity impact. The finite element algorithm is formulated in a general moving coordinate system. In the vicinity of the impact point contained by a moving failure front, the relative velocity of the coordinate system will approach the material particle velocity. The dynamic behavior inside the region is described by Eulerian formulation based on a hydroelasto-viscoplastic model. The failure front which can be regarded as the boundary of the impact zone is described by a transition layer. The layer will change the representation from the Eulerian mode to the Lagrangian mode outside the failure front by varying the relative velocity of the coordinate system to zero. The dynamic response in the remaining part of the structure described by the Lagrangian formulation can thus be treated using advanced structural analysis. An interfacing algorithm for coupling CELFE with NASTRAN is constructed to provide computational capabilities for large structures. The coupled CELFE-NASTRAN system also covers the computations of the structural response for a large time after the impact process is completed. Locally, the system has provisions for projectile rebound and for projectile sliding due to oblique impact.</p>			
17. Key Words (Suggested by Author(s)) High velocity impact, 3-D finite element, Eulerian, Lagrangian, Coupled Eulerian-Lagrangian, nonlinear analysis, material anisotropy, material flow, penetration, sliding, rebound, weak solutions algorithm.		18. Distribution Statement Unclassified, Unlimited	
19. Security Classif. (of this report) Unclassified	20. Security Classif. (of this page) Unclassified	21. No. of Pages 168	22. Price*

* For sale by the National Technical Information Service, Springfield, Virginia 22161

FOREWORD

This two part final report summarizes the efforts and accomplishments of the second phase of the subject contract covering the period June 1975 through September 1977. The study was conducted for the NASA-Lewis Research Center, Cleveland, Ohio, by personnel in the Engineering Sciences Section, Lockheed-Huntsville Research & Engineering Center, Huntsville, Alabama. The NASA-LeRC Project Engineer was Dr. C. C. Chamis, Mail Stop 49-3.

C. H. Lee was the principal investigator for the study, and the study was supervised by B. H. Shirley.

Work was begun on this contract on 28 June 1974. Phase I of the study was completed in June 1975 and an interim report was submitted and published as NASA CR-134933. Efforts on the study were directed toward the local analysis of three-dimensional high velocity impact problems based on Eulerian representation. The follow-on study in Phase II was directed toward the global finite element analysis of the problem by coupling the Eulerian mode, based on the results obtained in Phase I, with the Lagrangian mode. An interfacing procedure for coupling the presently developed program, CELFE, with NASTRAN was also accomplished to increase the range of applicability for the program.

Preceding page blank

ABSTRACT

The theoretical formulation of the Coupled Eulerian-Lagrangian Finite Element (CELFE) program for high velocity impact analysis is described. The formulation comprises the development of general objective of the present study, a 3-D finite element program capable of simulating the dynamic behavior in the vicinity of the impact point, together with predicting the dynamic response in the remaining part of the structural component subjected to high velocity impact.

The finite element algorithm is formulated in a general moving coordinate system. In the vicinity of the impact point contained by a moving failure front, the relative velocity of the coordinate system will approach the material particle velocity. The dynamic behavior inside the region will thus be described by Eulerian formulation based on a hydroelasto-viscoplastic model. The failure front which can be regarded as the boundary of the impact zone is described by a transition layer. The layer will change the representation from the Eulerian mode to the Lagrangian mode outside the failure front by varying the relative velocity of the coordinate system to zero. The dynamic response in the remaining part of the structure described by the Lagrangian formulation can thus be treated using advanced structural analysis.

An interfacing algorithm for coupling CELFE with NASTRAN is constructed to provide computational capabilities for large structures. The coupled CELFE/NASTRAN system also covers the computations of the structural response for a large time after the impact process is completed. Locally, the system has provisions for projectile rebound and for projectile sliding due to oblique impact.

CONTENTS

Section	Page
FOREWORD	ii
ABSTRACT	iii
LIST OF SYMBOLS	xi
1 INTRODUCTION	1-1
2 A HYDROELASTO-VISCOPLASTIC MODEL FOR HIGH VELOCITY IMPACT ANALYSIS	2-1
2.1 General Discussions of the Impact Process	2-1
2.2 Hydroelasto-Viscoplastic Model	2-2
2.3 Coupled Eulerian-Lagrangian Representation	2-5
3 BASIC EQUATIONS AND PROBLEM FORMULATION IN THE IMPACT ZONE	3-1
3.1 Local Representation of Dynamic Systems Under an Arbitrary Frame	3-1
3.2 Conservation Equations	3-3
3.3 Constitutive Equations	3-5
3.4 Failure Criteria	3-12
3.5 Equation of State	3-20
3.6 Initial and Boundary Conditions	3-23
4 BASIC EQUATIONS IN LAGRANGIAN ZONE	4-1
4.1 The Choices of Coupling Variables and Basic Equations in Lagrangian Zone	4-1
4.2 Elastodynamic Equations for Linear Anisotropic Materials	4-2
4.3 A General Transient Analysis	4-3
5 A FINITE ELEMENT ALGORITHM BASED ON THE THEOREM OF WEAK SOLUTIONS	5-1
5.1 On the Theorem of Weak Solutions	5-2
5.2 Finite Element Analogue of Weak Solutions	5-6

Section		Page
	5.3 Isoparametric Elements and Numerical Integration	5-12
	5.4 Generalized Two-Step, Time-Splitting Scheme	5-19
6	COUPLED EULERIAN-LAGRANGIAN FINITE ELEMENT (CELFE) CODE	6-1
	6.1 Basic Ideas and Formulation	6-1
	6.2 Finite Element Formulation for Transient Analysis	6-9
	6.3 Relevant Criteria In CELFE System	6-13
	6.4 Numerical Procedure for the Complete CELFE System	6-18
	6.5 Interfacing Procedure for CELFE/NASTRAN	6-19
7	TEST PROBLEMS AND NUMERICAL RESULTS	7-1
	7.1 Inviscid Hydrodynamic Model in Eulerian Mode	7-1
	7.2 Hydroelasto-Viscoplastic Model	7-30
	7.3 CELFE Analysis of Three-Dimensional Impact Problem	7-47
8	SUMMARY AND DISCUSSION	8-1
9	REFERENCES	9-1
Appendix		
	RANKINE-HUGONIOT RELATIONS	A-1

LIST OF TABLES

Table		Page
3-1	Nominal Properties for Some Typical Unidirectional Composites	3-18
3-2	Values of the Parameters in Tillotson's Equation	3-21

Table		Page
3-3	Values of the Parameters in the Los Alamos Equation of State for Various Materials	3-22
6-1	Classifications of Various Zones in High Velocity Impact	6-5
7-1	Propagation Velocity of Pressure Waves in Target at Various Times After Impact (with 30 Linear Elements)	7-29
7-2	Physical Properties for a Graphite HM/ERLA4617 Target Hit by an Aluminum Projectile	7-38
7-3	Physical Properties for a Boron AVCO 5505 Plate Hit by a Silastic Projectile	7-51

LIST OF FIGURES

Figure		Page
2-1	High Velocity Impact Process	2-3
2-2	A Three-Dimensional Region at $t = 0$	2-5
2-3	A Typical Configuration in Coupled Eulerian-Lagrangian Representation	2-8
3-1	Orthotropic Axes Stress Notation	3-17
3-2	Variation of Pressure vs Ratio of Densities for Aluminum	3-24
5-1	Location of Nodal Points in Three-Dimensional Elements	5-14
6-1	Typical Finite Element Sketch in Global Analysis of High Velocity Impact	6-3
6-2	CELFE Procedure	6-20
6-3	Interfacing Procedure for CELFE/NASTRAN	6-23
7-1	A Typical Finite Element Mesh of the Projectile-Target Configuration	7-3
7-2	Boundary Conditions	7-5

Figure		Page
7-3	Variation of Pressure with Internal Energy (Aluminum $\rho_o = 0.0976 \text{ lb/in}^3$, $\rho_\epsilon = 15.0 \text{ Mpa}$)	7-6
7-4	Variation of Pressure with Internal Energy (Aluminum $\rho_o = 0.0976 \text{ lb/in}^3$, $\rho_\epsilon = 27 \text{ to } 75 \text{ Mpa}$)	7-6
7-5	Variation of Pressure with Internal Energy (Aluminum $\rho_o = 0.0976 \text{ lb/in}^3$, $\rho_\epsilon = 405 \text{ to } 430 \text{ Mpa}$)	7-7
7-6	One-Dimensional Impact Problem	
	a. Configuration of Plates at Time of Impact	7-9
	b. Numbering of Nodes in the Finite Element (16 Linear Elements)	7-10
7-7	Time History of Pressure at Interface for 1-D Impact Problem Using Least Squares Scheme with 16 Linear Elements ($v_o = 0.00315 \text{ in}/\mu\text{sec}$, $\rho_o = 0.10 \text{ lb/in}^3$)	7-11
7-8	Pressure Distributions at Various Times for 1-D Impact Problem Using Least Squares Scheme with 16 Linear Elements ($v_o = 0.00315 \text{ in}/\mu\text{sec}$, $\rho_o = 0.10 \text{ lb/in}^3$)	7-12
7-9	Pressure Development at the Intensity Interface with 16 Linear Elements ($a = 0.5$, $\alpha = 0.00$)	7-14
7-10	Pressure Distributions at Various Times with 16 Linear Elements ($a = 0.5$, $\alpha = 0.0$)	7-15
7-11	Pressure Development at the Interface with 16 Linear Elements ($a = 2.0$)	7-16
7-12	Pressure Development at the Interface with 16 Linear Elements ($a = 4.0$)	7-17
7-13	Pressure Distributions at Various Times with 16 Linear Elements ($a = 2.0$)	7-18
7-14	Pressure Distributions at Various Times with 16 Linear Elements ($a = 4.0$)	7-19

Figure		Page
7-15	Pressure Development at the Interface Using 30 Linear Elements ($a = 2.0$, $\alpha = 0.0$ and 0.25)	7-20
7-16	Pressure Development at the Interface Using 30 Linear Elements ($a = 4.0$, $\alpha = 0.0$)	7-21
7-17	Pressure Distributions at Various Times Using 30 Linear Elements ($a = 2.0$, $\alpha = 0.0$)	7-22
7-18	Pressure Distributions at Various Times Using 30 Linear Elements ($a = 4.0$, $\alpha = 0.0$)	7-23
7-19	Pressure Development at the Interface Using 16 Quadratic Elements ($a = 2.0$, $\alpha = 0.0$ and 0.25)	7-24
7-20	Pressure Development at the Interface Using 16 Quadratic Elements ($a = 4.0$, $\alpha = 0.0$ and 0.25)	7-25
7-21	Pressure Distributions at Various Times Using 16 Quadratic Elements ($a = 2.0$, $\alpha = 0.0$)	7-27
7-22	Pressure Distributions at Various Times Using 16 Quadratic Elements ($a = 4.0$, $\alpha = 0.0$)	7-28
7-23	Momentum and Total Energy Distributions at $t = 30.0 \mu\text{sec}$ (16 Linear Elements; $a = 2.0$, $\alpha = 0.0$)	7-31
7-24	Momentum and Total Energy Distributions at $t = 30.0 \mu\text{sec}$ (30 Linear Elements; $a = 2.0$, $\alpha = 0.0$)	7-32
7-25	Momentum and Total Energy Distributions at $t = 30 \mu\text{sec}$ (16 Quadratic Elements; $a = 2.0$, $\alpha = 0.0$)	7-33
7-26	Axial Stress and Pressure Developments at the Interface Using 30 Linear Elements ($a = 4.0$, $\alpha = 0.0$) - Purely Plastic Case	7-35
7-27	Axial Stress and Pressure Developments at the Interface Using 30 Linear Elements ($a = 4.0$, $\alpha = 0.0$) - Viscoplastic Case	7-36

Figure	Page
7-28 Finite Element Mesh and Node Numbering for a Two-Dimensional Problem (Using Three-Dimensional Elements)	7-37
7-29 Stresses and Pressure Developments at Node No. 155 (Target - Graphite HM _η ERLA4617, Projectile - Aluminum, $V_o = 630 \text{ ft/sec}$)	7-40
7-30 Stresses and Pressure Developments at Node No. 177 (Target - Graphite HM/ERLA4617, Projectile - Aluminum, $V_o = 630 \text{ ft/sec}$)	7-41
7-31 Axial Stress and Pressure Distributions at $t = 1.0 \mu\text{sec}$; (a) on (Y, Z)-Plane at Y = 0, Z = 3.0315 in.; (b) on the Axis of Symmetry (i.e., X = Y = 0) (Target - Graphite HM/ERLA 4617, Projectile - Aluminum, $V_o = 630 \text{ ft/sec}$)	7-42
7-32 Axial Stress Distribution at Time $t = 0.2 \text{ sec}$ ($V_o = 24610.0 \text{ ft/sec}$)	7-43
7-33 Predicted Fracture Failure of Unidirectional Composites Due to High Velocity Impact ($V_o = 24610 \text{ ft/sec}$)	7-44
7-34 Finite Element Mesh of CELFE for 1-D Problem	7-46
7-35 Axial Stress Distributions at $t = 5.0 \mu\text{sec}$ Using 30 Linear Elements	7-48
7-36 Axial Stress Distributions at $t = 12.0 \mu\text{sec}$ Using 30 Linear Elements	7-49
7-37 Sketch of Three-Dimensional Impact Problem of a Unidirectional Boron AVCO 5505 Composite by a Silastic Particle	7-50
7-38 CELFE Finite Element Mesh for In-Core Model	7-52
7-39 Propagation of Failure Front with Respect to Time	7-54
7-40 Pressure Developments at Various Nodal Points	7-55
7-41 Stress Distributions Along x-Direction with $y = 0.0$, $z = 0.041$ at $t = 0.07 \mu\text{sec}$	7-56
7-42 CELFE Finite Element Model in the CELFE/NASTRAN Runs	7-57

Figure

- 7-43 NASTRAN Finite Element Model in CELFE/NASTRAN Runs 7-58

7-44 An Illustration of Connecting CELFE Model to NASTRAN
Model 7-59

LIST OF SYMBOLS

<u>Symbol</u>	<u>Description</u>
a	multiplier in multi-step time marching scheme defined in Eq. (5.24)
A, B	matrices
C_{ijkl}	stiffness coefficients
C_s	speed of sound
d_{ij}	strain rate tensor
d'_{ij}	deviatoric strain rate tensor
e	total specific energy
E	total energy
E_{ij}	Young's modulus
E_{ijkl}	elastic constants
$F(\Phi)$	function of plastic potential
F	body or applied force (Eqs. (312 and 313))
F, G, H, \dots	arbitrary functions
G_{ij}	shear modulus
K	stiffness matrix
J	Jacobian
\dot{J}	Time rate change of J
J_2	second invariant of stress tensor
n_j	j^{th} component of unit normal vector
N_j	shape function
P	pressure function
q	heat transfer rate
Q	dynamic pressure
R	an open set in (x, t) space
S	surface of a volume
S_{ij}	deviatoric stress tensor
\hat{S}_{ij}	deviatoric stress flux
t	time

<u>Symbol</u>	<u>Description</u>
Δt	time increment
T	temperature function
T_j	j^{th} component of surface traction
u_j	j^{th} component of linear displacement
v_j	j^{th} component of velocity
v_o	impact velocity
v_p	particle velocity
v_s	shock velocity
V_j	j^{th} component of momentum
$x, y, z, \text{ or } x_j$	Cartesian coordinates
\bar{Y}	yield stress
 <u>Greek</u>	
α	relaxation factor in multi-step scheme
γ	material parameters
δ	pressure ratio in equations of state or displacement vector
δ_{ij}	Kronecker delta
Δ	increment of the quantity following it
ϵ	specific internal energy
ϵ_p	generalized plastic strain
ϕ	primary variables in governing equations
Φ	plastic potential
θ_j	j^{th} component of angular displacement
Θ	divergence of velocity field
κ	hardening (or softening) parameter
λ	Lames' constant
μ	viscosity
ν	Poisson ratio
$\xi, \eta, \zeta \text{ or } \xi_j$	local coordinates in finite elements
$\zeta(x, t)$	C^∞ function with compact support on a subset of (x, t) space
π	dissipative component of pressure function

<u>Symbol</u>	<u>Description</u>
ρ	density
σ_{ij}	stress tensor
$\hat{\sigma}_{ij}$	stress flux
T	an interval in time
ψ	arbitrary function
Ψ	plastic potential
ω_{ij}	rigid body rotation tensor
Ω	open subset in Euclidean space
Ω	relative velocity of moving coordinate system with respect to material particle

Notations

$[A]$	matrix A
$\{A\}$	column matrix A
\tilde{A}	vector A
$\tilde{\tilde{A}}$	tensor A
$\llbracket A \rrbracket$	jump value of function A across a shock
∂A	boundary of a set A
∇	volume
\cup	union
∇A	gradient of scalar function A
∇^2	Laplacian operation
\dot{A}	time rate of change of A

Subscripts and Superscripts

C	pertaining to CELFE zone
i, j, k	pertaining to the coordinate axis i, j, k
o	pertaining to the initial value
p	pertaining to plastic materials
s	pertaining to the shock propagation
E _l	pertaining to elastic materials
E-L	pertaining to the E-L zone
N	pertaining to NASTRAN substructure
R-H	pertaining to the Rankine-Hugoniot relation
vp	pertaining to the viscoplastic materials
(n)	n th time step

1. INTRODUCTION

Over the last two decades considerable interest has been shown in the study of high velocity impact problems. This is primarily because of the extensive development of space vehicles and the need for information concerning the meteoroid hazard to these vehicles. Current interest in high velocity impact studies is largely due to the concern over the impact of interplanetary debris on space vehicles. These research results also have other industrial, as well as military, applications; for instance, in the high velocity impact on turbine blades of foreign objects such as rocks, birds or metal projectiles.

Motivated by military applications, seven symposiums were held on the subject during 1955-65 [1-7] under the sponsorship of the Army, Air Force and Navy. The bulk of the material presented at these symposiums consisted of experimental results and very little appeared on the theories explaining the high velocity impact phenomena. During the late 1960s efforts were expended toward formulating realistic theories to explain the complex dynamic and mechanical response of materials in hypervelocity impact [8-12].

The term "hypervelocity" (or high velocity) refers to the impact velocity regime in which the maximum stress developed by the primary shock wave greatly exceeds the material strengths of both the target and the projectile. During the early stages of the impact process, the target and the projectile behave essentially as compressible fluids and, consequently, several researchers [13-16] have employed pure hydrodynamic models to analyze the hypervelocity impact problems. However, these shock stresses decay very rapidly as the wave propagates away from the impact point and reach values comparable to the material yield strengths. From this point onward the material strengths become important in determining the stress and velocity fields in the target material and, consequently, due to more

involved material response to these rapidly applied stresses, the process gets more complicated. Hence, the purely hydrodynamic model cannot adequately describe the complex physical phenomena [17] and a more realistic model must be employed to account for all aspects of the high velocity impact phenomena. Several researchers have included the strength effects (e.g., see [18]) and there appeared many computer codes using more realistic hydrodynamic-elastic-viscoplastic models, [10] and [19-23]. The numerical techniques were largely based on the finite difference method, and they appear to be suited for problems with relatively simple geometries.

Since a hydrodynamic-elastic-viscoplastic model is basically a structural model, it would be appropriate to use structural techniques to solve the problem. Also, during the impact process, the geometry involved is generally very complicated, which would necessarily require a versatile and flexible technique in order to treat it accurately and realistically. The finite element method, which has proved to be highly successful in analyzing structural problems, is considered such a candidate. Leimbach and Prozan [24] have shown the superiority of the finite element method over the finite difference method for a simple impact problem, although their model is rather simple and unable to predict the actual dynamical response of materials in the impact region.

The general objective of the present study is to develop a three-dimensional finite element code to analyze structural components subjected to high velocity impact, using governing equations based on Eulerian and Lagrangian formulations. In particular, the impact point with its vicinity is to be represented by an Eulerian hydrodynamic-elasto-viscoplastic model, while the remaining structural components are to be analyzed with existing computer programs such as NASTRAN, for structural analysis. To bridge the gap between the Eulerian mode used for the impact region and the Lagrangian mode generally employed in structural analysis, a finite element code based on coupled Eulerian and Lagrangian formulation is developed.

This report contains the development of the complete system of the Coupled Eulerian-Lagrangian Finite Element (CELFE) program, including the interfacing procedure with NASTRAN, for handling a given structure subjected to high velocity impact. The report is divided into two parts: Part I includes a mathematical model for the impact process, together with the theoretical aspects of the CELFE algorithm. Part II presents listings and user's manual of the CELFE program and an illustration of the CELFE/NASTRAN interfacing procedure.

Following this introduction, Section 2 will present a preliminary discussion on the mathematical model to be developed, the basic idea of the associated simulation procedure, together with the geometric description of the Eulerian, Lagrangian and the coupled Eulerian-Lagrangian formulations. According to the simulation procedure, the geometry of the entire structure subjected to high velocity impact is divided into two parts, namely, the impact zone covering the impact point and its vicinity, and the Lagrangian (structure) zone for the remaining part. In the impact zone, the dynamic behavior induced by the impact is described by a hydroelasto-viscoplastic model represented in a general moving coordinate system. The development of the model and the associated governing equations are discussed in Section 3. By assuming the small deformation theory, on the other hand, the dynamic response due to the impact in the Lagrangian formulation is predicted using classical structural dynamic analyses. Section 4 summarizes briefly the related elastodynamic equations. In Section 5, a finite element algorithm for a general system of quasilinear equations with conservation form is formulated. The finite element analog of the equations is constructed as a direct consequence of the theorem of weak solutions. Thus, the entropy condition can be satisfied automatically in the formulation. The algorithm is formulated mainly for simulating the viscoplastic flow in the impact zone. In the same section, a generalized two-step scheme for time integration is also proposed to remedy the numerical instabilities and at the same time to speed up the computations. This scheme is applied for the entire CELFE procedure. A description of the complete CELFE procedure, the mechanisms coupling the

Eulerian-Lagrangian modes in particular, is presented in Section 6. The coupling mechanisms consist of an in-core coupling procedure to smoothly translate the coordinate system from Eulerian into Lagrangian, and an interfacing procedure for the CELFE/NASTRAN system. The complete CELFE system covers the computations for large time after the impact process is completed; it also simulates the rebound of the projectile from the target, and the sliding due to oblique impact. The criteria for the various cases are also discussed in Section 6. Section 7 summarizes results from numerical experiments for various test problems. The test problems include an inviscid hydrodynamic model with Eulerian description; a hydroelasto-viscoplastic model in Eulerian and the general moving coordinate system; and a complete CELFE model. Section 8 summarizes the present study and describes possible improvements and extensions of CELFE as related to computational efficiency, capability, and application.

2. A HYDROELASTO-VISCOPLASTIC MODEL FOR HIGH VELOCITY IMPACT ANALYSIS

The high velocity impact of a projectile with a solid target results in extremely complex phenomena. A complete description of this problem would involve considerations of all phases in the theory of continuum mechanics. This includes not only the compressible fluid flow, dynamics of elasticity and plasticity, but also other behavior such as melting and solidification, vaporization and condensation, and the kinetics of phase change. As a consequence, certain simplification is needed for tackling the problems. Several models have been proposed for various stages of the problem (see, e.g., [13, 16], [19-23]). In this section, a brief introduction of a hydrodynamic-elastic-viscoplastic model coupling the Eulerian and Lagrangian modes is presented.

2.1 GENERAL DISCUSSIONS OF THE IMPACT PROCESS

The analysis of high velocity projectile mechanics can be divided into two parts: (1) dynamic behavior of the projectile and target during the penetration process, and (2) structural response of the target after the penetration process is completed. The complex phenomena occur mostly during the penetration process. The following discussions are directed primarily toward this stage.

During the short period of time in which the projectile contacts the target, a plane shock wave is generated in the projectile as well as in the target. The pressure and hence the temperature behind these shock fronts are the highest that exist throughout the entire impact process, and may cause material failure in both the target and the projectile in the vicinity of the impact point.

Immediately after the impact, due to the high pressure, the material strength of the target can be ignored, and the material can be assumed to

behave essentially as an inviscid, compressible fluid. The shock waves generated in the projectile and target travel away from the interface (see Fig. 2-1). If the projectile is finite (in diameter), rarefaction waves will be generated and transmitted toward the axis of symmetry.

Formulation of rarefaction waves results in the ejection of target and projectile material particles. Moreover, the rarefaction waves weaken the shock wave and change its plane shape to approximately spherical. The strength of the shock continues to decrease due to the spherical attenuation and additional rarefaction waves, and the influence of the material strength and the strain rate effects must be taken into account. At the same time, the failure region grows following the outgoing shock until the penetration process is completed. In this stage, the dynamic behavior in the impact zone covering the failure region can be considered practically as a compressible, non-Newtonian flow; and the structural response in the remaining part of the target begins to appear as the disturbances propagate through the material.

2.2 HYDROELASTO-VISCOPLASTIC MODEL

Based on the discussions presented in the previous subsection, an anisotropic, hydroelasto-viscoplastic model for high velocity impact analysis can be set up as follows:

During a certain time period covering the penetration process, the dynamic behavior in the vicinity of the impact point containing a failure zone with moving front is regarded to be characterized by a compressible flow. The flow is governed by the Navier-Stokes equations (i.e., the conservation equations of mass, momentum and energy), in conjunction with an appropriate equation of state and the constitutive equations for both the target and projectile materials. In addition, a system of well established [25], hydrodynamic-elastic-viscoplastic constitutive equations based on Prandtl-Reuss theory is adopted to describe the material properties.

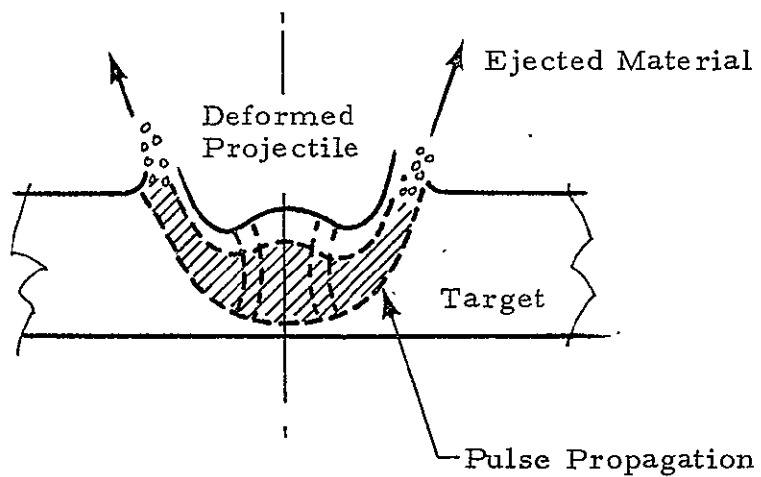
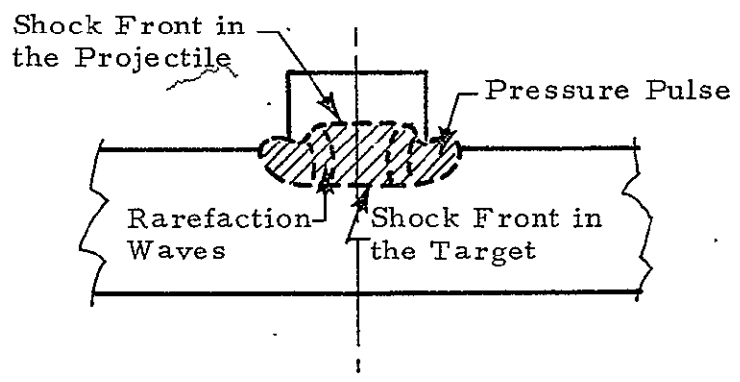
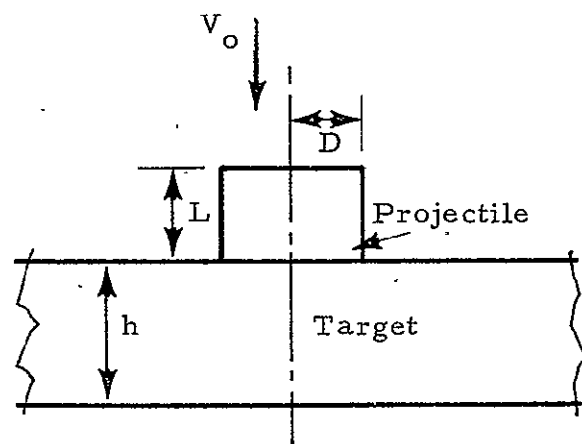


Fig. 2-1 - High Velocity Impact Process

If there is no substantial heat flux across the boundary of the body, the possible heat transfer will be induced only by heat source generated during the impact process. This heat transfer is generally not important because:

- There is a large temperature gradient across the failure front;
- A large part of the heat produced during the impact process, inside the failure zone, is converted to latent heat absorbed by the material for possible phase change.

Thus, at the present stage, the heat transfer will not be considered. Whenever the thermal effects between the body and its environment become important, these effects may be added into the energy equation in a straightforward manner.

The phase change, on the other hand, is assumed to be included into the equation of state as an approximation. There will be no attempt at this stage to incorporate the diffusion equation governing the phase change into the impact problem due to the above mentioned complexity. From a practical viewpoint, an accurately correlated, empirical equation of state would provide a better result on accounting the phase change in the present stage of development.

For three-dimensional problems, the formulation consists of five conservative equations and nine constitutive equations that are nonlinear partial differential equations in space and time. These equations will be solved using the finite element method in conjunction with an appropriate equation of state. The failure of the material caused by the impact is computed by various criteria depending on the material as well as the numerical scheme. In the present task where the failure zone is simulated using the Eulerian mode, criteria for the onset of viscoplastic flow are used. For composite materials, the failure prediction follows Chamis' criterion developed using micromechanics structure theory [26-28]; for metals, the plastic yielding is predicted in accordance with von Mises criterion.

Away from the impact zone, however, the structural response of the material is expected to be small compared to the one in the impact zone, and can be described essentially by the classical theories in structural dynamics. If the above mentioned system of 14 equations were to be retained for computing the dynamic response in this region, some of the equations become practically redundant, and thus a massive computation which occupies a large computer storage turns out to be trivial. In view of this inefficiency, the classical elastodynamic analyses are adopted for this portion.

The governing equations in this part depends on the choice of the analytic techniques. They may vary from the displacement, stress (or force), and energy finite element method, to the mixed variables and hybrid finite element method. The choice of analytic technique follows not only the type of structure under consideration, but it is also required to meet the following objectives: it must have the computational efficiency and simplicity to couple the analysis with that in the impact zone (i.e., in coupling the Eulerian and Lagrangian modes); and it must be capable of incorporation with available structural analysis programs such as NASTRAN.

2.3 COUPLED EULERIAN-LAGRANGIAN REPRESENTATION

2.3.1 Geometric Considerations

Consider an open (i.e., not including its boundary) bounded region Ω_0 at a time $t = 0$ in three-dimensional Euclidean space with its boundary $\partial\Omega$ (see Fig. 2-2). The union of Ω_0 and its boundary $\partial\Omega$ is the complete region (occupied by a body at time $t = 0$) and is denoted by

$$\bar{\Omega}_0 = \Omega_0 \cup \partial\Omega$$

where \cup denotes the union of two sets. In Ω_0 , there is a region Ω_1 with moving boundary $\partial\Omega_1$. Let Ω_2 denote the complement of $\bar{\Omega}_1$ in Ω_0 . Note that the region Ω_2 has two boundaries: one external boundary $\partial\Omega$ and one internal (the interface) boundary $\partial\Omega_1$.

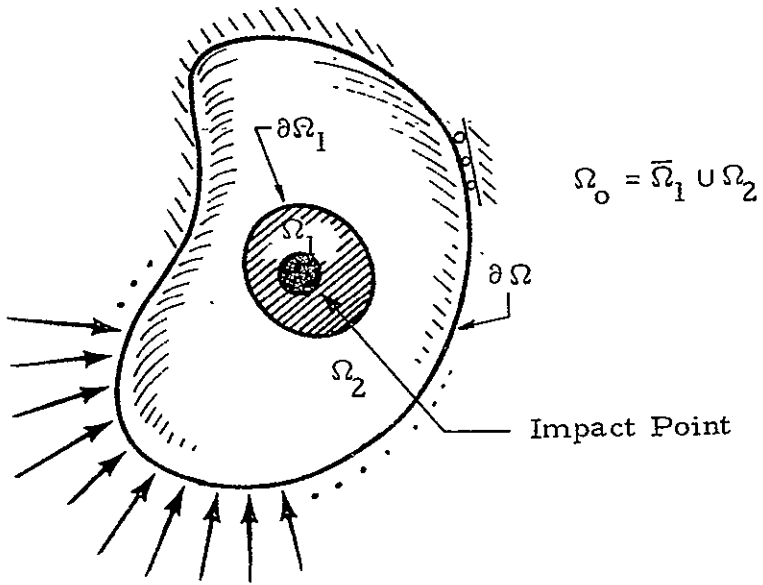


Fig. 2-2 - A Three-Dimensional Region at $t = 0$

Suppose that we are given, at time $t = 0$, the state of the fluid (or solid) occupying the region Ω_0 , the external forces acting on the boundary, and the boundary conditions. We are then required to determine the state of the fluid and the shape of the region at a subsequent time, $t = T$. Since we plan to analyze the impact point and the surrounding region, Ω_1 , separated from the remaining region, it is convenient to consider two different fluids (or materials) occupying two different portions, Ω_1 and Ω_2 , of Ω_0 ; that is

$$\Omega_0 = \bar{\Omega}_1 \cup \Omega_2, \quad \bar{\Omega}_1 = \Omega_1 \cup \partial\Omega_1$$

The surface $\partial\Omega_1$ is the material interface of the two regions, and it moves, as time advances, in such a manner that there are jumps on the pressure (or stresses) and velocity components over the surface.

According to this specification, we may define:

- $\bar{\Omega}_1$ to be the Impact Zone which contains the impact point and the failure zone with a moving boundary $\partial\Omega_1$; and
- Ω_2 to be the Structure Zone.

2.3.2 Euler and Lagrange Descriptions

There are two basic descriptions well known in continuum mechanics with respect to which the governing equations can be derived and computations can be carried out. In the Lagrange description, mostly used in solid and structural problems, a coordinate system is fixed in the body or configuration Ω_0 to be studied. The deformation of the projectile-target configuration is then measured with respect to this coordinate system. Consequently, the positions of the boundary $\partial\Omega$ and of the material interface $\partial\Omega_1$ are automatically determined. The description also permits the use of constitutive relations for the material in which the stress history of each portion of the body is taken into account. However, the Lagrange description is totally unsatisfactory for calculating a large deformation, and a flow in which turbulence develops or in which new material interfaces develop. In this case the nodal points of the mesh will attempt to follow the motion and the material particles which were initially adjacent to each other in Ω_0 no longer remain so.

In the Eulerian description, mostly used in fluid mechanic problems, the coordinate system is fixed in the space rather than in the body or configuration, and the calculations follow the material point that happens to be in a given location at that particular time. In this case the large distortions do not cause any problems; however, more than one material cannot be treated accurately. The curves approximating $\partial\Omega$ and $\partial\Omega_1$ move with the body and therefore create irregular, time-dependent boundary zones in the fixed Eulerian mesh.

2.3.2 Coupled Eulerian-Lagrangian Description

Obviously, neither Lagrange description nor Eulerian description alone is ideally suited for the analysis of impact problems. It is both natural and desirable to combine the use of Eulerian and Lagrangian modes depending on whether the material is in a fluid state (Eulerian mode) or solid state (Lagrangian mode). In doing so, there will be a great deal of flexibility in approximating the problem, thus enhancing the solution process regarding

accuracy and computational efficiency. The idea is very similar to the well known substructuring technique, but now with different descriptions (or modes) used in various regions. More specifically, in analyzing the impact problem of structural components, the existing NASTRAN program (in Lagrangian mode) can be used to advantage for the structure part, while an Eulerian description is necessary for the impact point and its vicinity.

The basic idea of coupling the Eulerian and Lagrangian modes is to approximate the structure in consideration, Ω_0 , into the combination of Eulerian and Lagrangian subregions separated by a transition zone. Figure 2-3 shows a configuration consisting of these different subregions.

As shown in Fig. 2-3, the structure zone, Ω_2 , can be identified with the Lagrangian subregion. Thus, it may also be called the Lagrangian zone, and denoted as L zone. In this subregion, the problem will be formulated according to the classical theory of elastodynamics under the Lagrangian coordinate system.

The impact zone, on the other hand, consists of the Eulerian subregion and the transition zone. We denote the Eulerian zone as E zone, and the transition zone as E-L zone represented by a moving coordinate system having varied local velocity with respect to the material particles. The relative velocity varies in such a way that, for each fixed t , it becomes identical to the local velocity within the E zone, and decreases monotonically toward the moving boundary $\partial\Omega_1$ through the E-L zone, and vanishes on $\partial\Omega_1$. This implies that the moving boundary $\partial\Omega_1$ is now described by the Lagrangian system.

The formulation thus enables us to trace the propagation of the failure front at each t on one hand, and couple the Eulerian mode in the E zone and the Lagrangian mode in the L zone smoothly for all $t > 0$ on the other hand.

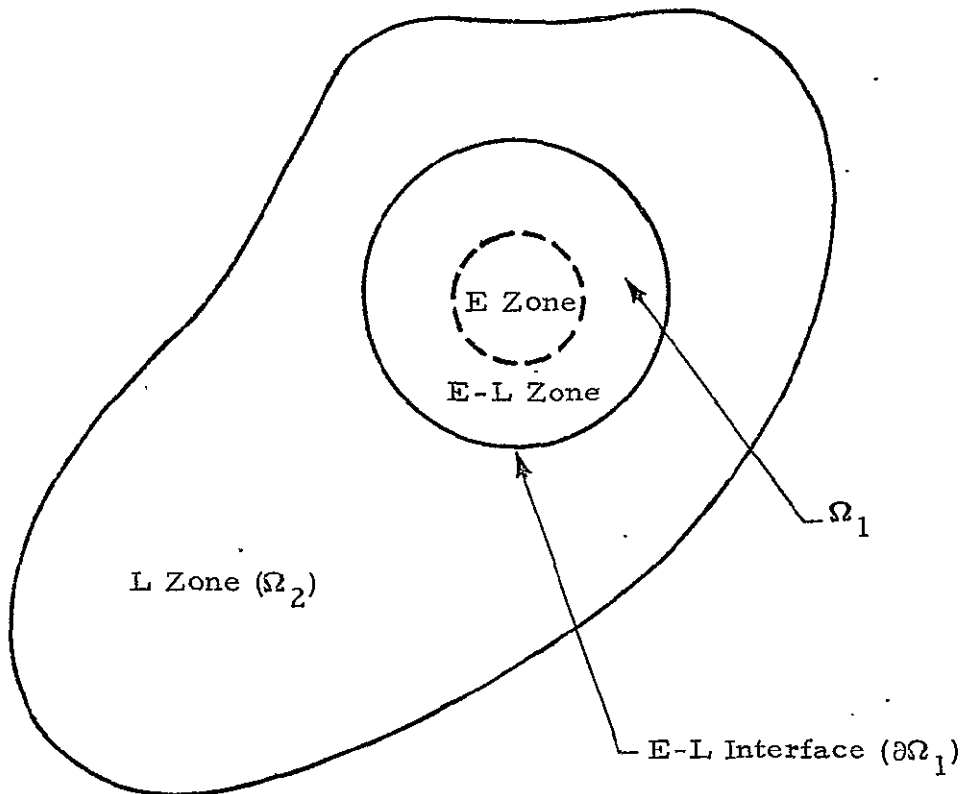


Fig. 2-3 - A Typical Configuration in Coupled Eulerian-Lagrangian Representation

3. BASIC EQUATIONS AND PROBLEM FORMULATION IN THE IMPACT ZONE

In this and the following section, the basic equations for various zones based on the model discussed in Section 2 will be formulated. As mentioned previously, these equations may be composed of different sets of primary variables. A prerequisite of choosing the equations for each zone is that there must exist at least one set of primary variables, i.e., the coupling variables, either common or directly related to the ones in the remaining zones. Since the final objective of this study is to couple the CELFE program with the NASTRAN program in which the displacement vector is used in the dynamic analysis of structures, the displacement will be chosen exclusively as our coupling variables in developing the CELFE code.

To couple the Eulerian and Lagrangian modes smoothly as outlined in Section 2, it is more convenient to represent the governing equations for the entire impact zone in a general moving coordinate system, instead of using the Eulerian mode in the E zone and the moving coordinates in the transition (E-L) zone. Mathematically, this representation can provide an identical approximation on changing the system from Eulerian to Lagrangian for all time as the finite element approximation of the physical problem itself. From a computational viewpoint, this representation cannot only simplify the programming, but can at the same time handle the movement of the free surface automatically.

3.1 LOCAL REPRESENTATION OF DYNAMICAL SYSTEMS UNDER AN ARBITRARY FRAME

Let $x = (x_1, x_2, x_3)$ be a Cartesian coordinate system moving with a certain velocity relative to the motion of the physical field, and let $X = (X_1, X_2, X_3)$ be the reference system. Then, the two coordinate systems can be related as

$$\underline{\underline{x}} = \underline{\underline{x}}(\underline{\underline{X}}, t) \quad (3.1)$$

When we know such a relation for every material particle in the medium, we say that the history of the motion is known at time t . We assume that the motion is continuous, single valued and that (3.1) can be inverted to give the initial position or material coordinates, $\underline{\underline{X}}$. A necessary and sufficient condition for the inverse to exist is that the Jacobian should not vanish:

$$J = \left| \frac{\partial \underline{\underline{x}}_i}{\partial \underline{\underline{X}}_j} \right| \neq 0, \quad 0 < J < \infty \quad \forall t \geq 0 \quad (3.2)$$

Let $\underline{\underline{\Omega}}$ denote the velocity of a material element relative to the $\underline{\underline{x}}$ system, i.e.,

$$\underline{\underline{\Omega}} = \frac{d \underline{\underline{x}}}{dt} = \underline{\underline{v}} - \dot{\underline{\underline{x}}} \quad (3.3)$$

where $\underline{\underline{v}}$ is the velocity of the material element, and $\dot{\underline{\underline{x}}} = \partial \underline{\underline{x}} / \partial t$ is the local time rate of change of the $\underline{\underline{x}}$ system. If F represents a certain physical quantity satisfying a dynamical system, then the total time derivative follows the equality

$$\frac{dF}{dt} = \frac{\partial F}{\partial t} + (\underline{\underline{\Omega}} \cdot \nabla) F \quad (3.4)$$

Clearly, when $\dot{\underline{\underline{x}}} = 0$, the systems $\underline{\underline{x}}$ and $\underline{\underline{X}}$ are identical, and $\underline{\underline{x}}$ represents the Eulerian system; when $\dot{\underline{\underline{x}}} = \underline{\underline{v}}$, on the other hand, it represents the Lagrangian system.

Following the implicit differentiation rule, the divergence of the local rate of change of $\underline{\underline{x}}$ system can be related to the Jacobian as

$$\nabla \cdot \dot{\underline{\underline{x}}} = \dot{J}/J \quad (3.5)$$

thus, (3.3) yields

$$\nabla \cdot \underline{\Omega} = \nabla \cdot \underline{v} - \dot{J}/J \quad (3.6)$$

Suppose now that there is a dynamic system with physical quantity F satisfying the equation

$$\frac{dF}{dt} = G(\underline{x}, t) \quad (3.7)$$

In particular, the continuity equation in \underline{x} system is readily obtained as

$$\frac{d\rho}{dt} + \rho \nabla \cdot \underline{v} = 0 \quad (3.8)$$

where ρ is the density of the material. Then, the dynamic system (3.7) can be deduced by applying (3.3), (3.6) and (3.8) into the following form:

$$\frac{\partial (\rho F)}{\partial t} + \rho F \Lambda + \nabla \cdot (\underline{\Omega} \rho F) = \rho G \quad (3.9)$$

where

$$\Lambda = \dot{J}/J \quad (3.10)$$

It is clear that the dynamic system (3.9) would reduce to the Eulerian form when $\dot{\underline{x}} = 0$; and to the Lagrangian form when $\underline{\Omega} = 0$.

3.2 CONSERVATION EQUATIONS

Let F , defined in Eq. (3.9), be 1, \underline{v} , and e , then the conservation of mass, momentum and energy can be obtained and written, respectively, in tensor form as

$$\frac{\partial \rho}{\partial t} + \frac{\partial(\Omega_k \rho)}{\partial x_k} + \rho \Lambda = 0 \quad (3.11)$$

$$\frac{\partial v_j}{\partial t} + \frac{\partial(\Omega_k v_j)}{\partial x_k} + v_j \Lambda = - \frac{\partial \sigma_{jk}}{\partial x_k} + F_j \quad (3.12)$$

$$\frac{\partial E}{\partial t} + \frac{\partial(\Omega_k E)}{\partial x_k} + E \Lambda = - \frac{\partial(v_j \sigma_{jk})}{\partial x_k} + v_j F_j \quad (3.13)$$

for $j, k = 1, 2, 3$, where

$$v_j = \rho v_j, \quad E = \rho e$$

denote the momentum and total energy, respectively, σ_{ij} , $i, j = 1, 2, 3$ denote the stresses, and F_j now denotes applied or body force.

When $\Omega_j = v_j$, $j = 1, 2, 3$, $\Lambda = 0$. Thus, Eqs. (3.11) through (3.13) reduce to the well-known continuity, momentum and energy equations, respectively, in the Eulerian description with conservation form:

$$\frac{\partial \rho}{\partial t} + \frac{\partial(v_k \rho)}{\partial x_k} = 0 \quad (3.14)$$

$$\frac{\partial v_j}{\partial t} + \frac{\partial(v_k v_j)}{\partial x_k} = - \frac{\partial \sigma_{jk}}{\partial x_k} + F_j \quad (3.15)$$

$$\frac{\partial E}{\partial t} + \frac{\partial(v_k E)}{\partial x_k} = - \frac{\partial(v_j \sigma_{jk})}{\partial x_k} + v_j F_j \quad (3.16)$$

When $\Omega_j \equiv 0$, $j = 1, 2, 3$, Eqs. (3.11) through (3.13) become the Lagrangian representation:

$$\frac{\partial \rho}{\partial t} + \rho \Lambda = 0 \quad (3.17)$$

$$\frac{\partial v_i}{\partial t} + v_j \Lambda = - \frac{\partial \sigma_{jk}}{\partial x_k} + F_j \quad (3.18)$$

$$\frac{\partial E}{\partial t} + E \Lambda = - \frac{\partial(v_j \sigma_{jk})}{\partial x_k} + v_j F_j \quad (3.19)$$

Here, Λ defined in Eq. (3.10) yields

$$J = \rho_0 / \rho \quad (3.20)$$

which is clearly equivalent to the continuity equation (3.17).

3.3 CONSTITUTIVE EQUATIONS

When the medium under consideration is inviscid, there are no shearing stresses. The stress tensor then becomes

$$-\sigma_{ij} = -P \delta_{ij}$$

where P is the thermodynamic pressure, and δ_{ij} is the Kronecker delta. In general, the stress tensor σ_{ij} can be decomposed into a (dynamic) pressure term and viscous terms that depend on the stress versus strain-rate relation. Accordingly, the stress tensor and the associated strain rate tensor are related to their respective deviatoric tensors by the following forms:

$$S_{ij} = \sigma_{ij} - 1/3 \sigma_{kk} \delta_{ij} \quad (3.21)$$

$$d'_{ij} = d_{ij} - 1/3 d_{kk} \delta_{ij} \quad (3.22)$$

where S_{ij} is the deviatoric stress tensor, d_{ij} is the strain rate tensor defined by

$$d_{ij} = \frac{1}{2} \left(\frac{\partial v_i}{\partial x_j} + \frac{\partial v_j}{\partial x_i} \right) \quad (3.23)$$

and d'_{ij} is the deviatoric tensor of strain rate. The normal components of S_{ij} are directly related to the pressure induced by the impact; the viscous effect, on the other hand, stems from a constitutive relation of S_{ij} toward d'_{ij} .

3.3.1 Deviatoric Stresses-Pressure Relation

Let us denote the mean of the principal components of stress by

$$Q \equiv -1/3 \sigma_{kk} \quad (3.24)$$

The quantity Q is called the dynamic pressure. The rate of dynamic pressure dQ/dt may, in general, be decomposed into a thermodynamical reversible component dP/dt and a dissipative component $d\pi/dt$, i.e.,

$$\frac{dQ}{dt} = \frac{dP}{dt} + \frac{d\pi}{dt} \quad (3.25)$$

In general, the rate at which the local thermodynamic equilibrium is attained is much greater than the rate at which a disturbance can be propagated. It is then reasonably accurate to assume that the local thermodynamic equilibrium exists at each instant. Hence, the reversible rate of pressure, dP/dt , is not path-dependent, and its integral P follows the equation of state which can be expressed as a function of density ρ and internal energy ϵ , i.e., $P = P(\rho, \epsilon)$. The dissipative component $d\pi/dt$, on the other hand, is generally a path-dependent function related to the bulk viscosity and the volume rate of change. It characterizes the physical dissipative rate of dilatation. For isotropic materials,

$$\pi = -(\lambda + 2/3 \mu) d_{kk} \quad (3.26)$$

The coefficient of bulk viscosity is defined by

$$\mu' = (\lambda + 2/3 \mu) = (P - Q)/d_{kk} \quad (3.27)$$

If the volumetric changes of the materials are elastic, the change of dynamic pressure is reversible which implies that $dQ/dt \equiv dP/dt$. Then the path-independent nature of P yields

$$Q = P = P(\rho, \epsilon) \quad (3.28)$$

Noting that for incompressible materials $d_{kk} = 0$, Eq. (3.28) follows immediately from Eq. (3.27). Equation (3.28) is also true for compressible fluids for which

$$(\lambda + 2/3 \mu) = 0 \quad (3.29)$$

Condition (3.29), known as Stoke's hypothesis, is a reasonable assumption for flow of monatomic gases; however, it is not valid for polyatomic gases or liquids, and distinction must be made between the mean stress Q and the thermodynamic pressure P .

For high velocity impact problems, the thermodynamic pressure is very high, and as aforementioned, the dynamic response in the material can thus be considered as an isentropic process. This implies that the material under high velocity impact can be assumed to possess elastic changes in volume, and (3.28) follows. Thus, (3.21) can be written as

$$S_{ij} = \sigma_{ij} + P \delta_{ij} \quad (3.30)$$

3.3.2 Hydrodynamic-Elastic-Viscoplastic Constitutive Relation

For linear elastic materials, the constitutive equation for stress and deformation rate is given by

$$S_{ij} = E_{ijkl} d_{kl} \quad (3.31)$$

where E_{ijkl} is a fourth-order tensor of material parameters. If the stress components σ_{ij} are symmetric, E_{ijkl} is also symmetric, i.e., $E_{ijkl} = E_{ijlk} = E_{jilk}$, etc. In general, there are 21 independent elastic constants. For orthotropic materials, the number of independent constants reduces to 9, and for

isotropic materials it reduces to 2. The isotropic constitutive relation is given by

$$S_{ij} = 2\mu d_{ij} + \lambda d_{kk} \delta_{ij} \quad (3.32)$$

where λ and μ are the Lame's (or viscous) constants.

Unfortunately, there does not exist a constitutive relation that describes all aspects (elastic, viscous and plastic) of mechanical behavior in a single expression. Constitutive relations of plasticity and viscoelasticity are essentially dynamical in nature. The constitutive relation in classical plasticity involves tensors of stress and rate of deformation, and describes rigid, perfectly plastic behavior. When elastic effects are to be considered in the analysis, this relation applies to the plastic part of the rate of deformation tensor. Similarly, the constitutive equation for viscoelastic material involves stress, elastic rate of deformation and the rate of deformation of a viscous fluid. In both cases, the elastic component of the rate of deformation tensor is usually written as a function of stress rate. Although the stress tensor is objective (axiom of objectivity requires that if a stressed continuum performs a rigid body motion and the stress field is independent of time when referred to a coordinate system attached to and moving with the material, the stress rate must vanish identically), the stress-rate tensor is not. Therefore, the stress rate $d\sigma_{ij}/dt$ should not occur in this form in the constitutive relation. An objective tensor containing the stress rate must be defined. Several objective tensors containing the stress rate can be constructed. One such tensor is due to Jaumann (see [29]) and is given by

$$\hat{\sigma}_{kl} \equiv \frac{d\sigma_{kl}}{dt} + \sigma_{km} \omega_{ml} - \sigma_{ml} \omega_{km} \quad (3.33)$$

where

$$\omega_{ij} = \frac{1}{2} \left(\frac{\partial v_i}{\partial x_j} - \frac{\partial v_j}{\partial x_i} \right) \quad (3.34)$$

The tensor $\hat{\sigma}_{kl}$ is called a stress flux. Other stress fluxes may be obtained by adding objective tensors such as $\underline{\underline{\sigma}}_{km} \underline{d}_{ml}$ to the right-hand side of (3.23):

$$\begin{aligned}\hat{\sigma}_{kl} &= \frac{d\sigma_{kl}}{dt} + \sigma_{ml} v_{m,k} + \sigma_{km} v_{m,l} \\ \hat{\sigma}_{kl} &= \frac{d\sigma_{kl}}{dt} - \sigma_{ml} v_{k,m} - \sigma_{km} v_{l,m} \\ \hat{\sigma}_{kl} &= \frac{d\sigma_{kl}}{dt} - \sigma_{ml} v_{k,m} - \sigma_{km} v_{l,m} + \sigma_{kl} v_{m,m}\end{aligned}\quad (3.35)$$

The stress flux $\hat{\sigma}_{kl}$ measures the rate of change of the stress component with respect to a rectangular Cartesian system that participates in the rotation of the material, and $\hat{\sigma}_{ij} = 0$ implies that the invariants of stress tensor are stationary.

From Eqs. (3.21) and (3.34), it is clear that the stress in Eq. (3.33) can be replaced by the deviatoric stress flux \hat{S}_{ij} . In general, the stress flux $\hat{\sigma}_{ij}$ and thus the deviatoric stress flux \hat{S}_{ij} are balanced by certain forcing functions Φ . Symbolically, we have

$$\hat{S}_{ij} = \Phi(S_{ij}, d_{ij}, v_j; x_j, t) \quad (3.36)$$

Here, the functional Φ of S_{ij} , d_{ij} and v_j may be regarded as a generalized material potential. The form of the potential depends on the material under consideration as well as its failure criterion, and may also include the effects of phase changes and related properties.

Assume that the materials under consideration are linear and follow the Prandtl-Ruess flow rule [25]. In accordance with the rule, the rate of deformation tensor (strain-rate tensor) d_{ij} can be split into two parts, i.e.,

$$d_{ij} = d_{ij}^e + d_{ij}^{vp} \quad (3.37)$$

where d_{ij}^e is the elastic component and d_{ij}^{vp} is the viscoplastic component of the deformation rate tensor. Here it is assumed that the medium is initially unstressed. The plastic part of the strain-rate tensor is at any instant proportional to the deviatoric stresses, i.e.,

$$d_{ij}^{vp} = \lambda_{ijkl} S_{kl} \quad (3.38)$$

where $\lambda_{ijkl} > 0$ and is in general a function of both time and spatial coordinates. The elastic part, on the other hand, is related to the stress flux \hat{S}_{ij} as

$$\hat{S}_{ij} = C_{ijkl} d_{kl}^e \quad (3.39)$$

Here the coefficient matrix C_{ijkl} depends on E_{ijkl} of Eq. (3.31). In this study we are concerned mainly with the fiber composite (orthotropic) and the isotropic materials.

For generally orthotropic materials, the local stiffness matrix C_{ijkl} can be expressed as

$$C_{\alpha\beta} = \begin{bmatrix} C_{11} & C_{12} & C_{13} & 0 & 0 & 0 \\ C_{21} & C_{22} & C_{23} & 0 & 0 & 0 \\ C_{31} & C_{32} & C_{33} & 0 & 0 & 0 \\ 0 & 0 & 0 & C_{44} & 0 & 0 \\ 0 & 0 & 0 & 0 & C_{55} & 0 \\ 0 & 0 & 0 & 0 & 0 & C_{66} \end{bmatrix} \quad (3.40)$$

where the subscripts α, β represent the location in the array with α indicating the effect and β indicating the cause. Comparing with subscripts $ijkl$, we note that $1 \leftrightarrow 11, 2 \leftrightarrow 22, 3 \leftrightarrow 33, 4 \leftrightarrow 23, 5 \leftrightarrow 31, 6 \leftrightarrow 12$ as α versus ij and β versus kl ; and

$$C_{\alpha\beta} = C_{\beta\alpha}, \quad \text{or} \quad C_{ijkl} = C_{klji}$$

In terms of engineering constants, the complete stiffness matrix with respect to the (x_1, x_2, x_3) -system with x_1 parallel to the fibers is given by

$$\begin{aligned}
 C_{11} &= (1 - \nu_{23} \nu_{32}) H E_{11}, \quad C_{22} = (1 - \nu_{31} \nu_{13}) H E_{22}, \\
 C_{33} &= (1 - \nu_{12} \nu_{21}) H E_{33}, \\
 C_{12} &= (\nu_{21} + \nu_{23} \nu_{31}) H E_{11}, \quad C_{13} = (\nu_{31} + \nu_{21} \nu_{32}) E_{11} \\
 C_{23} &= (\nu_{32} + \nu_{12} \nu_{31}) H E_{22}, \\
 C_{44} &= G_{23}, \quad C_{55} = G_{13}, \quad C_{66} = G_{12} \\
 H &= (1 - \nu_{12} \nu_{21} - \nu_{23} \nu_{32} - \nu_{31} \nu_{13} - 2 \nu_{12} \nu_{23} \nu_{31})^{-1}
 \end{aligned} \tag{3.41}$$

where E represents Young's modulus, G the shear modulus, and ν the Poisson ratio. The subscripts ij in E, G , and ν represent the measure of the strain in the x_j direction under uniaxial normal stress in the x_i direction.

For isotropic materials, the stiffness matrix becomes

$$C_{ijkl} = 2 \mu \delta_{ik} \delta_{jl} + \lambda \delta_{ij} \delta_{kl} \tag{3.42}$$

where μ and λ are Lame constants. Thus, Eq. (3.39) can be deduced further as

$$\begin{aligned}
 \hat{S}_{ij} &= \frac{d S_{ij}}{dt} + S_{im} \omega_{mj} - S_{mj} \omega_{im} \\
 &= 2 \mu d_{ij}^{e^1}
 \end{aligned} \tag{3.43}$$

Under the general moving coordinate system discussed in Section 3.1 (cf., Eq. (3.4)), Eq. (3.39) can be written as

$$\frac{\partial S_{ij}}{\partial t} + \Omega_k \frac{\partial S_{ij}}{\partial x_k} = C_{ijkl} d_{kl}^{e^1} - S_{im} \omega_{mj} + S_{mj} \omega_{im} \tag{3.44}$$

Similarly, by letting $\Omega_k = v_k$ for all $k = 1, 2, 3$, (3.44) can be deduced to the Eulerian mode as

$$\frac{\partial S_{ij}}{\partial t} + v_k \frac{\partial S_{ij}}{\partial x_k} = C_{ijkl} d_{kl}^{e'} - S_{im} \omega_{mj} + S_{mj} \omega_{im} \quad (3.45)$$

and to the Lagrangian mode by $\Omega_k = 0$ as

$$\frac{\partial S_{ij}}{\partial t} = C_{ijkl} d_{kl}^{e'} - S_{im} \omega_{mj} + S_{mj} \omega_{im} \quad (3.46)$$

3.4 FAILURE CRITERIA

Notice that the elastic part of the deviatoric strain-rate tensor, $d_{ij}^{e'}$, in Eq. (3.39) can be related to $d_{ij}^!$ and its viscoplastic counterpart as shown in Eq. (3.37). The viscoplastic part, which is in turn related to the deviatoric stresses, depends on the failure criteria of various materials.

3.4.1 Plastic Yield for Isotropic Materials

For isotropic materials, the plastic behavior is assumed to take place when a certain function of deviatoric stresses vanishes. This function is called the yield function. The yield function is constructed based on the following assumptions:

1. The yield surface is convex (or smooth).
2. The plastic component of the deformation rate tensor is normal to the yield surface at a smooth point.

If a yield condition is given by

$$\hat{F}(\sigma_{ij}, \kappa) = f(\sigma_{ij}, \kappa) - Y(\kappa) = 0 \quad (3.47)$$

with $\hat{F} < 0$ denoting the purely elastic region, then the deformation rate tensor will be a function of positive values of f . Here Y is a yield stress and κ is a

history dependent hardening (or softening) parameter. We now introduce the notion of "plastic potential" $\psi(\sigma_{ij})$ defined as

$$d_{ij}^{vp} = \gamma \langle \phi(f/f_o) \rangle \frac{\partial \psi}{\partial \sigma_{ij}} \quad (3.48)$$

where γ is a fluidity parameter which may depend on time, invariants of the rate of deformation, etc., and f_o denotes a reference value of f that makes the expression non-dimensional. To ensure no viscoplastic flow below the yield limit we write

$$\langle \phi(f/f_o) \rangle = \begin{cases} 0 & \hat{F} \leq 0 \\ \phi(f/f_o), & \hat{F} > 0 \end{cases} \quad (3.49)$$

A sufficiently general expression for $\phi(f/f_o)$ is given by a power law

$$\phi(f/f_o) = (f/f_o)^n \quad (3.50)$$

Various yield criteria and plastic potentials can be introduced depending on the material under study. For isotropic materials, for example, there are two well-known yield criteria: the Tresca yield criterion assumes that the yielding occurs when the greatest difference between any pair of the principal stresses σ_1 , σ_2 and σ_3 , reaches a specific value, Y . Usually, Y is taken to be the yield stress in uniaxial tension. The von Mises yield criterion for plastic yield is

$$(\sigma_1 - \sigma_2)^2 + (\sigma_2 - \sigma_3)^2 + (\sigma_3 - \sigma_1)^2 = 2 Y^2$$

or expressing in terms of σ_{ij} , we have

$$(\sigma_{11} - \sigma_{22})^2 + (\sigma_{22} - \sigma_{33})^2 + (\sigma_{33} - \sigma_{11})^2 + 6(\sigma_{12}^2 + \sigma_{13}^2 + \sigma_{23}^2) = 2 Y^2 \quad (3.51)$$

In what follows we shall take a more general yield function that is defined in terms of stress invariants as

$$f(\sigma_{ij}) = f(J_1, J_2, J_3) \quad (3.52)$$

where J_1 , J_2 and J_3 are the stress invariants,

$$J_1 = S_{ii}, \quad J_2 = \frac{1}{2} S_{ij} S_{ji}, \quad J_3 = \frac{1}{3} S_{ij} S_{jk} S_{ki}$$

Clearly, von Mises yield criterion, Eq. (3.51), is a special case of (3.47), where \hat{F} is given by

$$\hat{F}(\sigma_{ij}) = \sqrt{3 J_2} - Y \equiv \hat{F}(S_{ij}) \quad (3.53)$$

where Y is the uniaxial yield stress.

For a special case in which $\psi = \hat{F}$ and Y is independent of σ_{ij} , we have from (3.48)

$$d_{ij}^{VP} = \gamma(f/f_o)^n \partial \hat{F} / \partial \sigma_{ij} = \gamma(f/f_o)^n \partial f / \partial S_{ij}$$

and for $n = 1$, and f given by Eq. (3.53), this reduces to

$$d_{ij}^{VP} = \frac{3}{2} (\gamma/f_o) S_{ij} \quad (3.54)$$

After normalizing the yield surface by the von Mises yield stress, i.e., letting $F = \hat{F}/Y$, a more general form analogous to (3.54) follows from (3.53), namely

$$d_{ij}^{VP} = \gamma \Phi(F) S_{ij} / \sqrt{J_2} \quad (3.55)$$

where

$$F = \hat{F}/Y = \sqrt{\frac{\frac{2}{3} S_{mn}^2}{Y^2}} - 1$$

and the plastic potential

$$\Phi(F) = \begin{cases} 0 & \text{for } F \leq 0 \\ \Phi(S_{ij}) & \text{for } F > 0 \end{cases}$$

Thus, the stress flux for this case becomes upon substituting (3.55) into (3.43), while noting $d_{kk}^{vp} = 0$,

$$\hat{S}_{ij} = 2\mu(d_{ij}' - \gamma\phi(F) S_{ij}/\sqrt{J_2}) \quad (3.56)$$

Here, the material parameter γ and the plastic potential ϕ have to be found from experiments. For example, γ and $\phi(F)$ of 2024-T3 aluminum are readily obtained as

$$\phi = e^{F/\theta} - 1 \quad \text{for } \phi < \phi_o$$

$$\phi = \phi_o + \frac{\phi_o + 1}{\theta} (F - F_o) \quad \text{for } \phi > \phi_o$$

and $\gamma = 0.15 \sqrt{3} \text{ sec}^{-1}$, where $\phi_o = 10^6$, $F_o = \theta \log(\phi_o + 1)$, and θ is a new material function which depends on the generalized plastic strain ϵ_p as

$$\begin{aligned} \theta(\epsilon_p) &= 0.0003 + 0.0214 \epsilon_p - 0.0243 \epsilon_p^2 \quad \text{for } \epsilon_p \leq 0.4 \\ &= 0.005 \quad \text{for } \epsilon_p > 0.4 \end{aligned}$$

Here, the generalized plastic strain is

$$\epsilon_p = \int_0^t \sqrt{\frac{2}{3} d_{mn}^p d_{nm}^p} dt$$

3.4.2 Three-Dimensional Failure Criterion for Fiber Composites

It has been found from experimentation that unidirectional fibrous composites exhibit five primary failure stresses, namely, the longitudinal tensile, longitudinal compressive, transversal tensile, transversal compressive, and intralaminar (in-plane) shearing stresses. In addition, experimental observations also show that unidirectional fiber composites under combined loading fail at stress levels considerably different from those under simple loadings [30]. For generally orthotropic materials, there are four more basic material strengths relative to the normal axis, i.e., the normal

tensile and compressive, and two normal plane shearing stresses. These nine stresses are illustrated in Fig. 3-1. Accordingly, nine simple strengths and a combined-stress strength criterion are needed to fully describe the strength (limit) behavior of the materials. The strength depends not only on the properties of the constituents, but also the particular fabrication process (such as void content, size and distribution, filament spacing, residual stress, etc.). These effects must be included into the formulation of the criterion.

Various mathematical models have been proposed to describe the strength (limit) behavior (cf., Chapter 2 of Ref. 30 for detailed discussions). In this study, we adopt the formulation constructed by Chamis based on a two-level, linear, semi-empirical theory [26].

The first level is a theory to predict the simple strengths from constituent properties and fabrication process considerations. Formally, the simple strengths can be related to the constituent properties and the fabrication process as follows:

$$S_f = f[(k, d, N, A)_{f, v}, k_m, (E, \nu, G, S, \epsilon_p)_{f, m}, S_B, S_R] \quad (3.57)$$

where S_f in (3.57) denotes a certain uniaxial simple strength; $(k, d, N, A)_{f, v}$ denotes volume content, size, number, and distribution of filaments and voids; k_m denotes the volume content of the matrix; $(E, \nu, G, S, \epsilon_p)_{f, m}$ represents the elastic and strength properties of the filaments and matrix; and S_B and S_R denote interface bond strength and residual stress, respectively. The void content, the bond strength, and the residual stresses are dependent on the filament surface treatment. They also depend on various matrix additives, hardeners, temperature, and pressure during fabrication and on the fabrication method of making the composite. The simple strengths, S_f , for various cases can be obtained either from the appropriate tests directly, or by evaluation of the function in (3.57) utilizing the micromechanics structure theory [26]. These strengths, together with other material properties, for some typical materials are listed in Table 3-1.

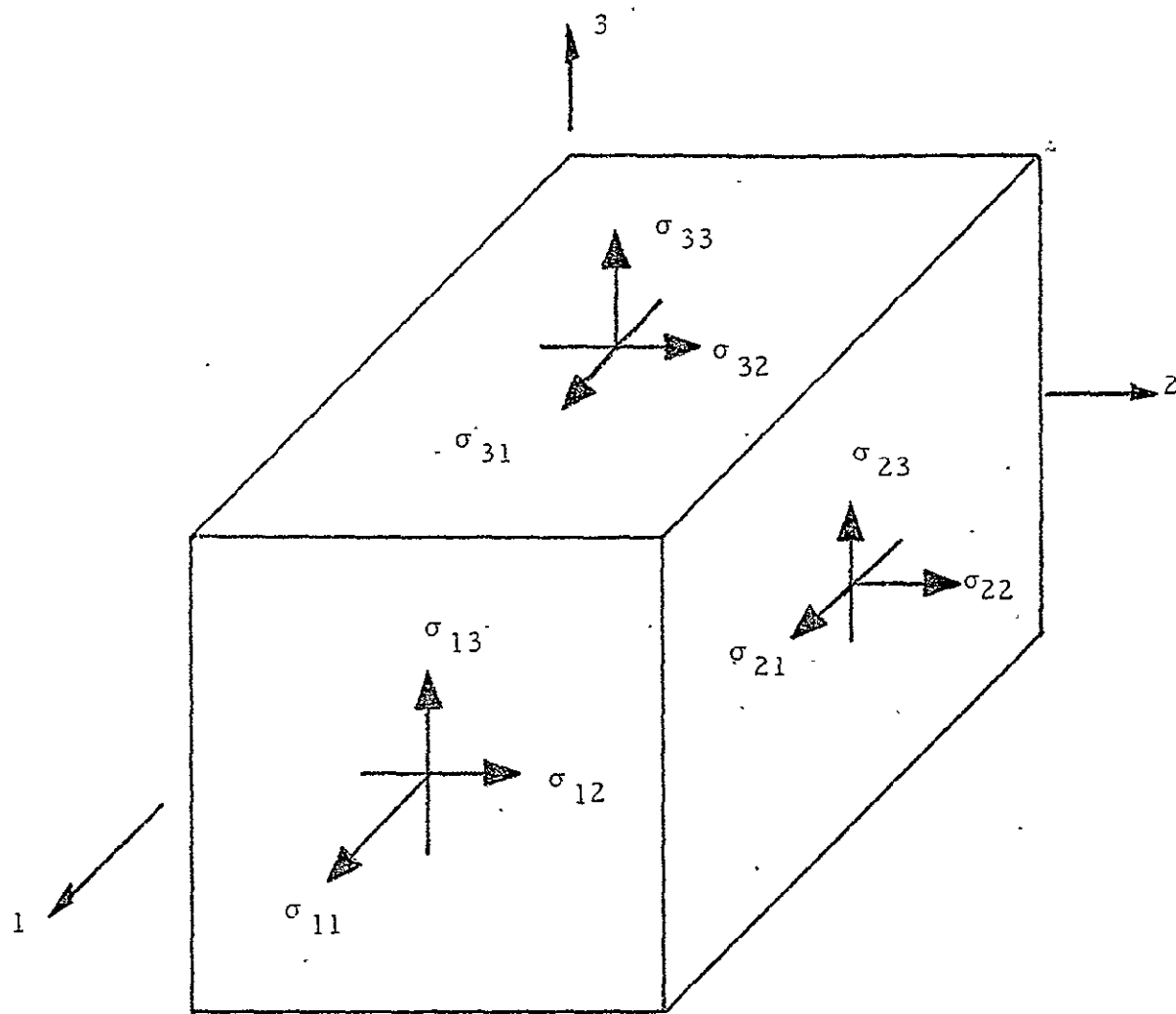


Fig. 3-1 - Orthotropic Axes Stress Notation

Table 3-1
NOMINAL PROPERTIES FOR SOME TYPICAL UNIDIRECTIONAL COMPOSITES

Properties	Symbols	Units	Graphite HM/ERLA4617	Graphite AS/PR5208	Kevlar 49/ERLA4617	S-Glass/ERLA461	Boron/Avco 5505
Density	ρ	lb/in ³	0.056	0.057	0.055	0.077	0.073
Elasticity Modulus	$E_{\ell 11}$	10 ⁶ psi	27.5	18.5	10.0	7.2	29.2
	$E_{\ell 22}, E_{\ell 33}$	10 ⁶ psi	1.0	2.0	0.6	2.8	3.15
Shear Modulus	$G_{\ell 12}, G_{\ell 13}$	10 ⁶ psi	0.9	0.6	0.4	1.0	0.78
	* $G_{\ell 23}$	10 ⁶ psi	0.4	0.4	0.2	0.5	0.60
Poisson's Ratio	$\nu_{\ell 12}, \nu_{\ell 13}$	—	0.1	0.2	0.4	0.3	0.17
	* $\nu_{\ell 23}$	—	0.4	0.5	0.4	0.5	0.53
Thermal Coefficient of Expansion	$\alpha_{\ell 11}$	10 ⁻⁶ in/in/F	-0.5	3.3	-1.4	2.1	3.40
	$\alpha_{\ell 22}, \alpha_{\ell 33}$	10 ⁻⁶ in/in/F	25.6	16.2	32.0	19.9	18.0
Uniaxial Failure Stresses	$S_{\ell 11T}$	ksi	122.0	181.0	206.0	257.0	199.0
	$S_{\ell 11C}$	ksi	128.0	165.0	28.0	146.0	232.0
	$S_{\ell 22T}, S_{\ell 33T}$	ksi	6.1	8.0	0.8	11.0	8.1
	$S_{\ell 22C}, S_{\ell 33C}$	ksi	28.5	25.0	9.2	26.5	17.9
	$S_{\ell 12}, S_{\ell 13}$	ksi	8.9	13.0	3.5	10.2	9.1
	* $S_{\ell 23}$	ksi	5.6	9.1	2.7	11.5	8.9
Ply Thickness	t_{ℓ}	in.	0.0050	0.0049	0.0046	0.0046	0.0051

*These values were estimated using composite micromechanics.

The second level is a theory to predict the onset of failure in terms of simple strengths predicted in the first level theory. The governing equation for the failure criterion is derived from the following two postulates:

- At the onset of failure, the distortion energy under simple as well as combined loads remains invariant; and
- The tensile and compressive properties of the materials are the same up to the onset of failure but may be different thereafter.

The formal derivations are given in detail in Ref. 27, and the resulting equation is presented as follows.

Chamis' Failure Criterion for Fiber Composites: Let σ_ℓ denote the stress, S_ℓ the uniaxial strength ($S > 0$). Then the functional describing the three-dimensional, combined-stress failure criterion in fiber composites is given by

$$F(\sigma_\ell, S_\ell, K_\ell) = 1 - \left[\left(\frac{\sigma_{\ell 11\alpha}}{S_{\ell 11\alpha}} \right)^2 + \left(\frac{\sigma_{\ell 22\beta}}{S_{\ell 22\beta}} \right)^2 + \left(\frac{\sigma_{\ell 33\gamma}}{S_{\ell 33\gamma}} \right)^2 + \left(\frac{\sigma_{\ell 23S}}{S_{\ell 23S}} \right)^2 + \left(\frac{\sigma_{\ell 13S}}{S_{\ell 13S}} \right)^2 + \left(\frac{\sigma_{\ell 12S}}{S_{\ell 12S}} \right)^2 \right. \\ \left. - K_{\ell 23\beta\gamma} \frac{\sigma_{\ell 22\beta}}{S_{\ell 22\beta}} \frac{\sigma_{\ell 33\gamma}}{S_{\ell 33\gamma}} - K_{\ell 13\alpha\gamma} \frac{\sigma_{\ell 11\alpha}}{S_{\ell 11\alpha}} \frac{\sigma_{\ell 33\gamma}}{S_{\ell 33\gamma}} - K_{\ell 12\alpha\beta} \frac{\sigma_{\ell 11\alpha}}{S_{\ell 11\alpha}} \frac{\sigma_{\ell 22\beta}}{S_{\ell 22\beta}} \right] \quad (3.58)$$

which states that

$$\begin{aligned} F(\sigma_\ell, S_\ell, K_\ell) &> 0 && \text{No failure} \\ F(\sigma_\ell, S_\ell, K_\ell) &= 0 && \text{Incipient failure} \\ F(\sigma_\ell, S_\ell, K_\ell) &< 0 && \text{Failure} \end{aligned} \quad (3.59)$$

Here, K_ℓ are certain coupling coefficients; the subscript ℓ denotes unidirectional composite (or ply, layer, lamina) properties; the subscripts α, β, γ denote T for tension or C for compression; the subscript S denotes shear; and the numerical subscripts 1, 2, 3 refer to an orthogonal coordinate system with 1 taken along the fiber direction, 2 transverse to it and 3 through the thickness.

In the application of Eq. (3.58), it is assumed that the coupling coefficients, K_{ℓ} , the stresses, σ_{ij} , and the unidirectional strength, S_{ℓ} are known. Following the derivations given in Ref. 26, the coupling coefficients, K_{ℓ} , can be expressed in terms of engineering material constants as

$$\begin{aligned} K_{\ell 12} &= \frac{(1 + 4\nu_{\ell 23} - \nu_{\ell 21}) E_{\ell 22} + (1 - \nu_{\ell 23}) E_{\ell 11}}{[E_{\ell 11} E_{\ell 22} (2 + \nu_{\ell 12} + \nu_{\ell 13}) (2 + \nu_{\ell 21} + \nu_{\ell 23})]^{1/2}} \\ K_{\ell 23} &= \frac{(1 + 4\nu_{\ell 31} - \nu_{\ell 32}) E_{\ell 33} + (1 - \nu_{\ell 31}) E_{\ell 22}}{[E_{\ell 22} E_{\ell 33} (2 + \nu_{\ell 23} + \nu_{\ell 21}) (2 + \nu_{\ell 32} + \nu_{\ell 31})]^{1/2}} \\ K_{\ell 13} &= \frac{(1 + 4\nu_{\ell 31} - \nu_{\ell 32}) E_{\ell 11} + (1 - \nu_{\ell 12}) E_{\ell 33}}{[E_{\ell 33} E_{\ell 11} (2 + \nu_{\ell 31} + \nu_{\ell 32}) (2 + \nu_{\ell 13} + \nu_{\ell 12})]^{1/2}} \end{aligned} \quad (3.60)$$

where E denotes the elastic modulus, ν the Poissons' ratio. The values of E , ν , together with the unidirectional strengths S_{ℓ} are known either from measurements or from composite micromechanics; whereas, the stresses are obtained by three-dimensional analysis.

3.5 EQUATION OF STATE

Since the governing equations contain the pressure (implicitly, in σ_{ij}), a constitutive relation must be used relating the pressure to the density and the specific internal energy. This particular constitutive relation is well known as the equation of state. For high velocity impact of solid bodies, two equations of state are well known. One of these is developed by Tillotson [31] and the other is developed by Osborne and his associates at Los Alamos Scientific Laboratory.

Tillotson's Equation of State: Tillotson's equation of state (for either compression or expansion regions) is given by

$$P = \pi(\epsilon, \rho) + A\mu + B\mu^2 \quad (3.61a)$$

for $\rho > \rho_o$ with $0 < \epsilon < \epsilon_s$, and

$$P = a\epsilon\rho + \left[\frac{b\epsilon\rho}{(1 + \epsilon/\epsilon_0\eta^2)} + A\mu e^{-\beta(1/\eta - 1)} \right] e^{-\alpha(1/\eta - 1)^2} \quad (3.61b)$$

for $\rho < \rho_0$ with $\epsilon > \epsilon_s$, where

$$\mu = \eta - 1, \quad \eta = \rho/\rho_0, \quad \rho_0 = \text{initial density}$$

$$\pi(\epsilon, \rho) = \epsilon\rho \left[a + \frac{b}{\epsilon/\epsilon_0\eta^2 + 1} \right]$$

and a, b, A, B and ϵ_0 are parameters (constant) which depend on the material, and ϵ_s is the sublimation energy. Values of these parameters for some materials are given in Table 3-2.

Table 3-2
VALUES OF THE PARAMETERS IN TILLOTSON'S EQUATION

Parameter	Aluminum	Iron	Copper	Lead
ρ_0 (gm/cm ³)	2.702	7.86	8.9	11.34
a	0.5	0.5	0.5	0.4
b	1.63	1.5	1.5	2.4
A (mb)	0.752	1.28	1.39	0.466
B (mb)	0.65	1.05	1.1	0.0026
α	5.0	5.0	5.0	10.0
β	5.0	5.0	5.0	2.0
ϵ_0 (mb·cm ³ /gm)	0.05	0.095	0.325	0.02
ϵ_s (mb·cm ³ /gm)	0.03	0.0244	0.0138	0.0026

Note that (3.61) is not defined for certain states, for example when $\rho < \rho_0$ with $\epsilon < \epsilon_s$, and $\rho > \rho_0$ with $\epsilon > \epsilon_s$. Some investigators have used some kind of average of the pressures given by (3.61a) and (3.61b) for these states. At this writing Tillotson's equation is not used in the calculations.

Los Alamos Equation of State: Another equation of state that is widely employed in high velocity impact calculations was derived at Los Alamos Scientific Laboratory. The equation is given by

$$P(\epsilon, \rho) = \begin{cases} [A\mu + \delta \hat{E} (B + \delta \hat{E} C)] / (\delta \hat{E} + \varphi_o), & \mu \geq 0 \\ [\mu A_1 + \delta \hat{E} (B_o + \mu B_1 + \delta \hat{E} C)] / (\delta \hat{E} + \varphi_o), & \mu \leq 0 \end{cases} \quad (3.62)$$

where

$$\delta = \rho_o / \rho, \quad \mu = \rho / \rho_o - 1$$

$$A = A_1 + \mu A_2, \quad B = B_o + \mu (B_1 + \mu B_2)$$

$$C = C_o + \mu C_1, \quad \hat{E} = \rho \epsilon$$

and $A_1, A_2, B_o, B_1, B_2, C_o, C_1$ and φ_o are constants that depend on the material. Values of these parameters for plexiglas, graphite, aluminum, iron, copper and lead are given in Table 3-3.

Table 3-3
VALUES OF THE PARAMETERS IN THE LOS ALAMOS EQUATION
OF STATE FOR VARIOUS MATERIALS

Parameter	Plexiglas	Graphite	Aluminum	Iron	Copper	Lead
ρ_o	1.18	2.25	2.702	7.86	8.9	11.34
A_1	0.006199	0.1608	1.1867	7.78	4.9578	1.4844
A_2	0.015491	0.1619	0.763	31.18	3.6884	1.6765
B_o	0.14756	0.8866	3.4448	9.591	7.4727	8.7317
B_1	0.05619	0.5140	1.5451	15.676	11.519	0.96473
B_2	0.50504	1.4377	0.9643	4.634	5.5251	2.6695
C_o	0.5575	0.5398	0.43382	0.3984	0.39493	0.27732
C_1	0.6151	0.5960	0.54873	0.5306	0.52883	0.43079
φ_o	0.100	0.500	1.5	9.00	3.60	3.300

The parameters are fitted for gram-centimeter-microsecond system of units.

A comparison of the pressures computed from Tillotson's equation of state and Los Alamos equation of state is made for aluminum ($\rho_0 = 2.702$ gm/cm³) at $\epsilon = 0.5$ mb-cm³/gm (see Fig. 3-2). The equation of state which closely agrees with the experimental data for a given material will be used.

3.6 INITIAL AND BOUNDARY CONDITIONS

To complete the description of the high velocity impact problem, we must include the initial and boundary conditions, which, in general, are time dependent.

Initial Conditions: At time $t = 0$ values of all the dependent variables ($\rho, \mathbf{v}, \epsilon, P, S$) must be specified at the nodal points of the mesh. It is not essential to specify all these quantities at the same set of nodal points. For instance, in the analysis of target alone, the velocities, density and specific internal energy are specified at one set of points, and pressure is specified at a different set of points.

Boundary Conditions: Depending on the type of the boundary (e.g., rigid boundary, free surface, interface, plane of symmetry, etc.), there are different kinds of boundary conditions in a problem. At a rigid boundary the normal component of the particle velocity must coincide with the normal component of the velocity of the rigid boundary. For a fixed (in time) boundary, the normal component of the particle velocity must be zero at that boundary. A plane of symmetry can be interpreted as a fixed boundary. On the free surface, the total stress must vanish. Whereas, the movement of the free surface will be included as an integrated part of the coupled Eulerian-Lagrangian finite element solution of the governing equations. At an interface (as well as a contact discontinuity) the total stress and the normal component of particle velocity must be continuous, and the density, internal energy and the tangential component of particle velocity may be discontinuous (jumps).

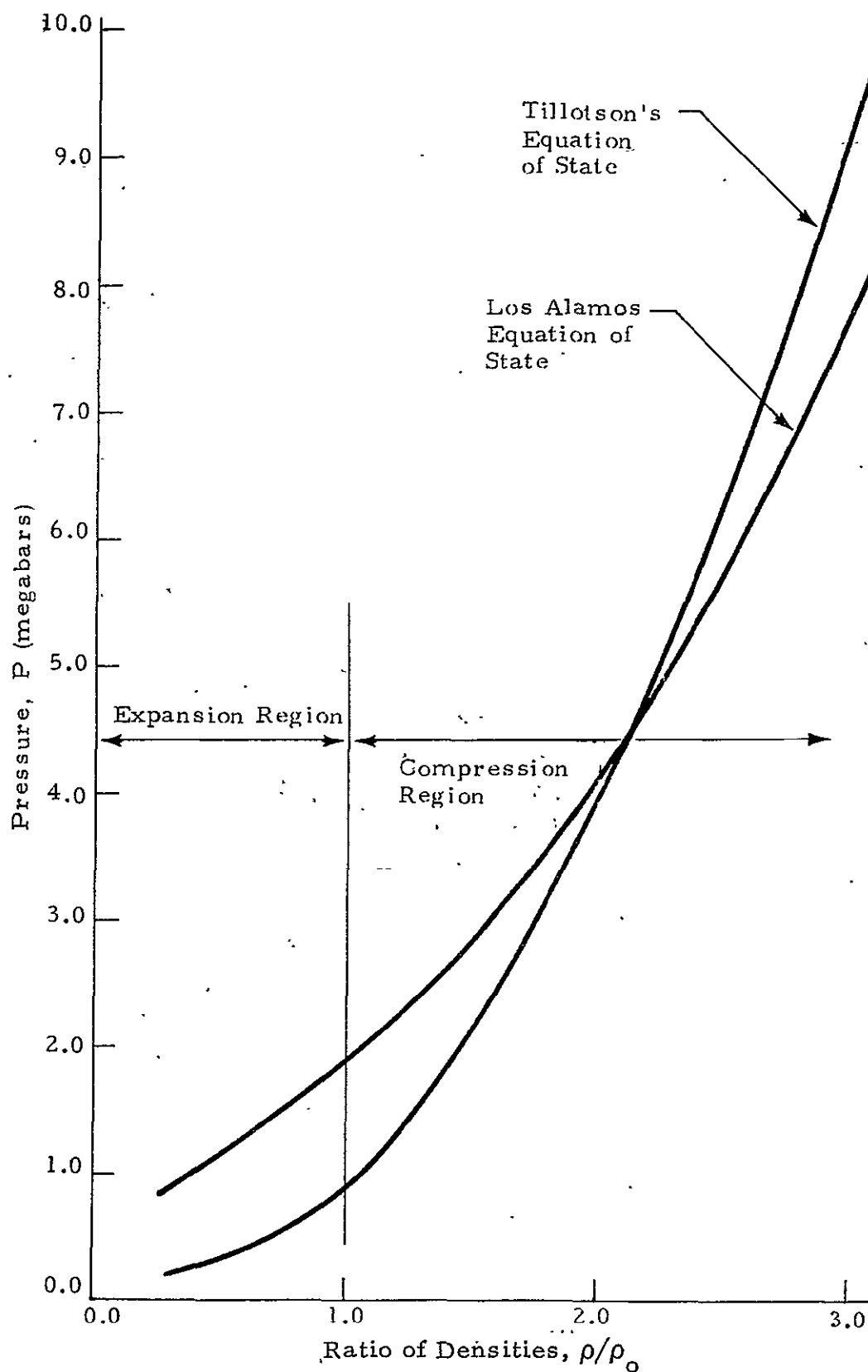


Fig. 3-2 - Variation of Pressure vs Ratio of Densities for Aluminum
 $(\rho_0 = 2.702, \epsilon = 0.5)$

4. BASIC EQUATIONS IN LAGRANGIAN ZONE

In this section, the basic equations to be adopted to describe the dynamic behavior in the Lagrangian zone are presented. It is clear that, away from the impact zone, the disturbance in the target is comparatively small. Thus, the conventional structural analysis suffices to deal with the dynamic response in this region.

4.1 THE CHOICES OF COUPLING VARIABLES AND BASIC EQUATIONS IN LAGRANGIAN ZONE

There are various forms of equations governing different types of problems in structural dynamics; yet they consist of different sets of primary variables. Hence, the choice of an appropriate set of equations with certain primary variables for the Lagrangian zone becomes important in the development of the coupling code. The governing equations and thus their finite element analog to be adopted here must not only be appropriate for tackling the dynamic response in the Lagrangian zone for a wide range of problems, but the mathematical formulation must also follow the following prerequisites:

- In the sense of "coupling," the coupling variables introduced in Section 2 must be a part of the primary variables in the governing equations, say, e.g., the displacement field, or stress field, hybrid, etc.
- The finite element analog of the equations must be compatible with the one in the impact zone, and can be coupled smoothly in the mathematical sense as well as the computational sense.
- The finite element code for its part can either be incorporated into the CELFE code as an integrated part of the complete code, or found in the existing programs for handling large structural systems such as NASTRAN.

The choice of the coupling variables is not unique in general, but can be optimized to reduce the computational efforts. Recall that the primary

variables in the impact zone consist of density, ρ , velocities v_j (or momentums $V_j = \rho v_j$), stresses σ_{ij} , and mesh coordinates x_j in a general moving system governed by Eq. (3.3). (In the Eulerian zone contained by the impact zone, the last set of variables, x_j , is of course fixed.) In structural dynamics, on the other hand, there is a well developed finite element displacement method, finite element force method, mixed models, hybrid models, and free vibration analysis, etc., that can be suitably applied for analyzing the response in the Lagrangian zone.

If the force method is used, e.g., one must choose the stresses (or deviatoric stresses) as the coupling variables for the impact zone. In this case, the approach complicates the coupling process. The complexities are caused not only by the indirect relation on forces and stresses between the Lagrangian and the impact zone, but it is also seen in the impact zone that the stresses are related to a secondary variable, P , the thermodynamic pressure. This relation may lead to a certain difficulty in formulating the coupling procedure whenever the stresses are a part of the coupling variables.

Thus, in view of the above mentioned prerequisites, the finite element displacement method appears to be a better approach. First, there is an existing module in NASTRAN based on this formulation. Second, all the primary variables of this formulation, consisting only of displacements and velocities, are taken to be the coupling variables for the Lagrangian part in the coupling process. In particular, they can be related directly to their counterpart in the impact zone. This makes the coupling process rather straightforward. Hence, in this study, we will adopt the finite element displacement approach.

4.2 ELASTODYNAMIC EQUATIONS FOR LINEAR ANISOTROPIC MATERIALS

The equations of motion for linear elastic materials are readily obtained as

$$\rho \frac{\partial^2 u_j}{\partial t^2} = \frac{1}{2} \frac{\partial}{\partial x_k} \left\{ C_{jklm} \left(\frac{\partial u_l}{\partial x_m} + \frac{\partial u_m}{\partial x_l} \right) \right\} + F_j \quad (4.1)$$

where u_j is the displacement along the x_j -axis, and F_j is the corresponding forcing term.

For fiber composites where the material stiffness coefficients, C_{ijkl} , are given in Eqs. (3.40) and (3.41), the equations of motion (Eq. (4.1)) can be deduced to the following form:

$$\rho \frac{\partial^2 u_j}{\partial t^2} = \frac{\partial}{\partial x_j} \left(C_{jjkk} \frac{\partial u_k}{\partial x_k} \right) + \frac{1}{2} \frac{\partial}{\partial x_k} \left[C_{jkjk} \left(\frac{\partial u_j}{\partial x_k} + \frac{\partial u_k}{\partial x_j} \right) \right] + F_j \quad (4.2)$$

For isotropic materials, the equations are reduced to a well-known system of wave equations:

$$\rho \frac{\partial^2 u_j}{\partial t^2} = \mu \nabla^2 u_j + (\lambda + \mu) \frac{\partial^2 u_k}{\partial x_j \partial x_k} + F_j \quad (4.3)$$

where ∇^2 is the Laplacian operator.

4.3 A GENERAL TRANSIENT ANALYSIS

It should be noted that, in three-dimensional finite element approximations of the above equations, three-dimensional solid elements must be used. Thus, it turns out to be less efficient for tackling large structures in most of the cases under consideration. In order to include the uses of special elements, such as bending, membrane, etc., the following system for general transient analysis is introduced:

$$\hat{\rho} \ddot{\delta} + F(\delta, \dot{\delta}; x, t) = G(x, t) \quad (4.4)$$

where $\hat{\rho}(x)$ may be the density or mass, $x = (x_1, x_2, x_3)$. Here, δ is the deflection vector consisting of lateral as well as rotational components, F is a specified vector valued function characterizing the elastic as well as the damping effects, and G is a forcing function.

When $\delta = (u_1, u_2, u_3)$, i.e., δ does not contain the rotational components,

$$F = \frac{1}{Z} \frac{\partial}{\partial x_k} \left[C_{jklm} \left(\frac{\partial u_l}{\partial x_m} + \frac{\partial u_m}{\partial x_l} \right) \right]$$

and

$$G = F_j$$

for $j, k, l, m = 1, 2, 3$, Eq. (4.1) follows from Eq. (4.4). For general linear materials, Eq. (4.4) yields

$$\ddot{\rho}\delta + B\dot{\delta} + K\delta = G \quad (4.5)$$

where B is the damping factor, K the spring constant, and

$$\delta = \begin{cases} u_j; j = 1, 2, 3 \\ \theta_j; j = 1, 2, 3 \end{cases}$$

Here, θ_j , $j = 1, 2, 3$, are angular displacements.

5. A FINITE ELEMENT ALGORITHM BASED ON THE THEOREM OF WEAK SOLUTIONS

When shocks, compression waves, or other types of discontinuities occur in the material, the gradients of the dependent variables in the governing equations become very large in the neighborhoods of discontinuities. These large gradients lead the effective diffusion terms in the equations to be negative in some regions, and cause numerical instabilities in the interaction process during the numerical computations if conventional methods such as Galerkin's, least squares, etc., are used. To overcome these difficulties, an alternative finite element formulation is proposed in this section. The procedure is utilized primarily for analyzing the dynamic behavior in the impact zone.

The present formulation consists of two primary portions. First, the finite element formulation is constructed based on the theorem of weak solutions, so that the jump conditions can be satisfied automatically to take care of shock propagations. Second, a generalized two-step, time-splitting, shock capturing scheme is developed and implemented. The scheme so construed has a capability to remedy the spurious oscillations arising due to numerical instabilities.

In Section 5.1, a general discussion on the theorem of weak solutions will be presented without proof. The governing equations in conservation form and the finite element analog of these equations, are presented in the subsequent subsection. The formulation of a two-step scheme is discussed in Section 5.3.

5.1 ON THEOREM OF WEAK SOLUTIONS

The results from the theorem of weak solutions have been frequently applied in developing finite difference schemes for solving first order, nonlinear hyperbolic equations. In most of these schemes, the advantages of the resulting forms deduced from the theorem are not fully utilized, since they are always in the integral form. This fact, however, can be implemented in a simple way into a finite element scheme, and the advantages can be fully utilized.

Various works on finite difference have indicated that, when the results of the theorem of weak solutions are to be used in the numerical scheme, the governing equations need to be converted into a conservation form (cf. Ritchmyer and Morton [32]). In what follows, therefore, we restrict ourselves in considering the system of hyperbolic equations in conservation form. It is obvious that all the conservation equations can be written in this form. The constitutive equations, however, are not in the conservation form but can be recast into such form as shown in subsection 5.2.

5.1.1 Theorem of Weak Solutions for First Order Quasilinear Equations

Consider a Cauchy problem of a system of quasilinear hyperbolic equations

$$\frac{\partial \phi}{\partial t} + \frac{\partial F^k}{\partial x_k} = G, \quad k = 1, 2, 3 \quad (5.1)$$

on a cylinder $R = \Omega(x) \times T(t)$, where $x = (x_1, x_2, x_3)$, $F^k = F^k(x, t, \phi)$, and $G = G(x, t, \phi)$. A class of piecewise smooth and piecewise continuous, vector valued functions ϕ in R for $t > 0$ are called the weak solutions of (5.1) if the following relation is satisfied:

$$\iint_R \zeta \left(\frac{\partial \phi}{\partial t} + \frac{\partial F^k}{\partial x_k} \right) d\Omega dt = \iint_R \zeta G d\Omega dt \quad (5.2)$$

where $\zeta \in C^\infty$ with compact support on R , i.e., ζ is any continuously differentiable function that vanishes on ∂R , the boundary of R .

Lax [33], Oleinik [34] et al., have shown that, if the following conditions are satisfied:

1. For each $k = 1, 2, 3$, F^k has a continuous partial derivative with respect to ϕ , and $\frac{\partial F^k}{\partial \phi}$ is bounded for $(x, t) \in R$;
2. For bounded ϕ , $\frac{\partial^2 F^k}{\partial \phi \partial x_k}$, $\frac{\partial^2 F^k}{\partial \phi^2}$ are continuous, and $\frac{\partial^2 F^k}{\partial \phi^2} \geq 0$;
3. The function $G(x, t, \phi)$ has a continuous partial derivative with respect to ϕ ,

the generalized solution of Eq. (5.1) with a piecewise continuous initial condition is unique, and satisfies Eq. (5.2).

The proof of the theorem can be found in the aforementioned references, and will not be presented here. However, we will discuss in what follows some immediate consequences of the theorem directly related to our proposed formulation.

5.1.2 Jump Condition

Following the Green's theorem, Eq. (5.2) can be deduced to a form

$$\iint_R \left(\phi \frac{\partial \zeta}{\partial t} + F^k \frac{\partial \zeta}{\partial x_k} \right) d\Omega dt$$

$$\begin{aligned}
&= \iint_R \frac{\partial}{\partial t} [\zeta(x, t) \phi(x, t)] d\Omega dt + \iint_{\partial\Omega \times T} \zeta F^k n_k dS dt \\
&- \iint_R \zeta G d\Omega dt
\end{aligned} \tag{5.3}$$

where n_k is the k^{th} component of the outward unit normal vector on $\partial\Omega$, the boundary of Ω .

Observe now the integrals

$$I_v = \iint_R \frac{\partial}{\partial t} [\zeta(x, t) \phi(x, t)] d\Omega dt \tag{5.4}$$

for some $t_1 \in T$, $x \in \bar{\Omega}$; and

$$I_s = \iint_{\partial\Omega \times T} \zeta(x, t) F^k(x, t) n_k dS dt \tag{5.5}$$

for all $x \in \partial\Omega$, and $t \in T$. Since $\zeta(x, t)$ is piecewise continuous function with compact support in R , it is obvious that $I_s = 0$ if there is no discontinuity in R . Otherwise, we may deduce without difficulty the jump of the function F^k across the discontinuity, i.e.,

$$I_s = \iint_{\partial\Omega_s \times T} \zeta [[F^k]] n_k dS dt \tag{5.6}$$

where $\partial\Omega_s$ is the surface of the shock layer, $[[F^k]]$ denotes the jump of F^k , the k^{th} component of F , across the shock.

For the integral I_v , if there is no discontinuity on \bar{R} , Eq. (5.4) can be reduced to

$$I_v = \int_{\Omega} \zeta(x, t) \phi(x, t) d\Omega - \int_{\Omega} \zeta(x, 0) \phi(x, 0) d\Omega$$

Across a shock, however, the Leibnitz's rule yields

$$\begin{aligned} I_v &= \int_{\Omega} \zeta(x, t) \phi(x, t) d\Omega - \int_{\Omega} \zeta(x, 0) \phi(x, 0) d\Omega \\ &\quad + \int_T \zeta(x_1, \xi) \phi(x_1, \xi) \int_{\partial\Omega_s(t)} C_s(\eta, \xi) dS(\eta) d\xi \\ &\quad - \int_T \zeta(x_2, \xi) \phi(x_2, \xi) \int_{\partial\Omega_s(t)} C_s(\eta, \xi) dS(\eta) d\xi \end{aligned}$$

where the subscripts 1, 2 denote the values upstream and downstream of the shock, respectively. Here, the speed of sound is defined as

$$C_s = \left| \frac{\partial S^k}{\partial t} n_k \right|$$

The last two terms in the above integral are no more than the jump of ϕ , i.e.,

$$I_v = \int_{\Omega} \zeta(x, t) \phi(x, t) d\Omega - \int_{\Omega} \zeta(x, 0) \phi(x, 0) d\Omega$$

$$+ \int_{\partial\Omega_s \times T} \zeta(x, t) C_s(x, t) [[\phi]] dS dt \quad (5.7)$$

Since the entropy condition requires that

$$C_s [[\phi]] - [[F^k]] n_k = 0 \quad (5.8)$$

The substitution of (5.6) and (5.7) into (5.3) then yields

$$\begin{aligned} & \iint_R (\phi \frac{\partial \zeta}{\partial t} + F^k \frac{\partial \zeta}{\partial x_k}) d\Omega dt \\ &= - \int_{\Omega} \zeta(x, 0) \phi(x, 0) d\Omega - \iint_R \zeta G d\Omega dt \end{aligned} \quad (5.9)$$

This consequence implies that (5.9) satisfies the jump condition (5.8) automatically.

5.2 FINITE ELEMENT ANALOGUE OF WEAK SOLUTIONS

Recall that we are considering a system of equations

$$\frac{\partial \phi}{\partial t} + \frac{\partial F^k}{\partial x_k} = G \quad (5.1)$$

where $F^k = F^k(x, t, \phi)$, $k = 1, 2, 3$ and $G = G(x, t, \phi)$. In this section, we shall formulate the finite element analog of equations in the form of (5.1). As aforementioned, the present formulation is developed primarily to deal with the behavior in the impact zone. Thus, we have to write the conservation equations and the constitutive equations for the impact zone in the above form.

5.2.1 Governing Equations of Conservation Form in Impact Zone

It is obvious that the conservation equations (3.11) through (3.13) are in the conservation form. The constitutive equations (3.39), however, are not in the form of (5.1). Therefore, we recast the constitutive equations as

$$\frac{\partial S_{ij}}{\partial t} + \frac{\partial (\Omega_k S_{ij})}{\partial x_k} = \Theta S_{ij} + C_{ijkl} d_{kl}^{e'} - S_{im} \omega_{mj} + S_{mj} \omega_{im} \quad (5.10)$$

where $\Theta = \operatorname{div} \Omega$. Here, an additional term ΘS_{ij} appears on the right-hand side, which is considered as the forcing term.

In view of (3.11) through (3.13) and (5.10), we may replace the forcing function $G(x, t, \phi)$ in (5.1) by $\Lambda\phi + G(x, t)$ without causing any confusion. Thus, instead of (5.1), we have

$$\frac{\partial \phi}{\partial t} + \frac{\partial F^k}{\partial x_k} = \Lambda\phi + G(x, t) \quad (5.11)$$

For the impact zone, the vector valued functions in (5.11) represent, respectively, the following physical quantities:

$$\phi = \begin{Bmatrix} \rho \\ V_j; j = 1, 2, 3 \\ E \\ S_{ij}; i, j = 1, 2, 3 \end{Bmatrix} .$$

$$F^k = \begin{Bmatrix} \Omega_k \rho \\ \Omega_k V_j - \sigma_{jk}; j = 1, 2, 3 \\ \Omega_k E - \sigma_{\ell k} v_\ell \\ \Omega_k S_{ij}; i, j = 1, 2, 3 \end{Bmatrix}; k, \ell = 1, 2, 3$$

$$\Delta\phi = \left\{ \begin{array}{l} \rho \frac{\partial}{\partial x_k} (\Omega_k - v_k) \\ v_j \frac{\partial}{\partial x_k} (\Omega_k - v_k); j = 1, 2, 3 \\ E \frac{\partial}{\partial x_k} (\Omega_k - v_k) \\ S_{ij} \frac{\partial \Omega_k}{\partial x_k}; i, j = 1, 2, 3 \end{array} \right\}; k = 1, 2, 3$$

$$G = \left\{ \begin{array}{l} 0 \\ F_j; j = 1, 2, 3 \\ F_\ell v_\ell \\ C_{ijkl} d_{kl}^{e'} - S_{im} \omega_{mj} + S_{mj} \omega_{im}; i, j = 1, 2, 3 \end{array} \right\}; k, \ell = 1, 2, 3 \quad (5.12)$$

5.2.2 Finite Element Formulation

Suppose that the discrete approximation is constructed by appropriate interpolation functions in each element, and take $\zeta(x, t)$ defined in (5.9) to be the weighting function with compact support in the cylinder $\Delta R = \Omega_e \times T$. Here, Ω_e is the volume of an element e , $T = [0, \Delta t]$ and Δt is the time step in the time-split scheme. In order to utilize integral relation (5.9) to minimize the error, we have to approximate the (weighting) function ζ by the shape function at the previous time step, i.e.,

$$\zeta_r = (1 - \frac{t}{\Delta t}) N_r, r = 1, 2, \dots, m \quad (5.13)$$

where m is the number of nodes in the element e . Also, approximate the solution to (5.11) as

$$\phi = N_s \left[(1 - \frac{t}{\Delta t}) \phi_s^{(n)} + \frac{t}{\Delta t} \phi_s^{(n+1)} \right], s = 1, \dots, m \quad (5.14)$$

With these expressions, we obtain a matrix equation in the form of

$$\left(\begin{bmatrix} A_{rs} \\ B_{rs} \end{bmatrix} - \frac{\Delta t}{3} \begin{bmatrix} B_{rs} \\ B_{rs} \end{bmatrix} \right) \left\{ \phi_s^{(n+1)} \right\} = \left(\begin{bmatrix} A_{rs} \\ B_{rs} \end{bmatrix} + \frac{2\Delta t}{3} \begin{bmatrix} B_{rs} \\ B_{rs} \end{bmatrix} \right) \left\{ \phi_s^{(n)} \right\} + t \left\{ C_r \right\} \quad (5.15)$$

where

$$\begin{aligned} A_{rs} &= \int_{\Omega_e} N_r N_s d\Omega \\ B_{rs} &= \int_{\Omega_e} \left[\Omega_k \frac{\partial N_r}{\partial x_k} + \Lambda N_r \right] N_s d\Omega \\ C_r &= \int_{\Omega_e} \left[H^k \frac{\partial N_r}{\partial x_k} + G N_r \right] d\Omega \end{aligned} \quad (5.16)$$

Here, the vector $\underline{H} = \underline{E} - \phi \underline{\Omega}$.

5.2.3 Finite Element Analogs of Equation (5.11) in Eulerian and Lagrangian Modes

Eulerian Representation: When $\Omega_k = v_k$, $k = 1, 2, 3$, the conservation form (5.11) becomes

$$\frac{\partial \phi}{\partial t} + \frac{\partial F^k}{\partial x_k} = G \quad (5.17)$$

with

$$\phi = \left\{ \begin{array}{l} \rho \\ V_j; j = 1, 2, 3 \\ E \\ S_{ij}; i, j = 1, 2, 3 \end{array} \right\}$$

$$F^k = \begin{Bmatrix} v_k \rho \\ v_k v_j - \sigma_{jk}; j = 1, 2, 3 \\ v_k E - \sigma_{\ell k} v_\ell \\ v_k S_{ij}; i, j = 1, 2, 3 \end{Bmatrix}; k, \ell = 1, 2, 3$$

$$G = \begin{Bmatrix} 0 \\ F_j; j = 1, 2, 3 \\ F_\ell v_\ell \\ C_{ijkl} d_{kl}^{e'} - S_{im} \omega_{mj} + S_{mj} \omega_{im}; i, j = 1, 2, 3 \end{Bmatrix}; k, \ell = 1, 2, 3 \quad (5.18)$$

The corresponding finite element analog of (5.17), (5.18) still retains the similar form as (5.15), but with different coefficient matrices, i.e.,

$$\left(\begin{bmatrix} A_{rs} \\ B_{rs} \end{bmatrix} - \frac{\Delta t}{3} \begin{bmatrix} B_{rs} \end{bmatrix} \right) \{ \phi_s^{(n+1)} \} = \left(\begin{bmatrix} A_{rs} \\ B_{rs} \end{bmatrix} + \frac{2\Delta t}{3} \begin{bmatrix} B_{rs} \end{bmatrix} \right) \{ \phi_s^{(n)} \} + \Delta t \{ C_r \} \quad (5.15)$$

where

$$\begin{aligned} A_{rs} &= \int_{\Omega_e} N_r N_s d\Omega \\ B_{rs} &= \int_{\Omega_e} v_k \frac{\partial N_r}{\partial x_k} N_s d\Omega \\ C_r &= \int_{\Omega_e} \left[H^k \frac{\partial N_r}{\partial x_k} + N_r G \right] d\Omega \end{aligned} \quad (5.19)$$

Lagrangian Representation: When $\Omega_k \equiv 0$, $k = 1, 2, 3$, the functions F^k and A are reduced to the following forms:

$$F^k = \begin{Bmatrix} 0 \\ -\sigma_{jk}; j = 1, 2, 3 \\ -\sigma_{\ell k} v_\ell \\ 0 \end{Bmatrix}; k, \ell = 1, 2, 3$$

$$\Lambda \phi = \left\{ \begin{array}{l} -\rho \frac{\partial v_k}{\partial x_k} \\ -V_j \frac{\partial v_k}{\partial x_k}; j = 1, 2, 3 \\ -E \frac{\partial v_k}{\partial x_k} \\ 0; i, j = 1, 2, 3 \end{array} \right\}; k = 1, 2, 3 \quad (5.20)$$

For this case, the corresponding finite element analog does not retain the original form. Instead, it yields the classical form of explicit scheme:

$$[A_{rs}] \{ \phi_s^{(n+1)} \} = [A_{rs}] \{ \phi_s^{(n)} \} + \Delta t \{ C_r \} \quad (5.21)$$

with

$$A_{rs} = \int_{\Omega_e} N_r N_s d\Omega$$

$$C_r = \int_{\Omega_e} \left[-F^k \frac{\partial N_r}{\partial x_k} + N_r G \right] d\Omega \quad (5.22)$$

5.2.4 Remarks

Instead of using Eq. (5.13), we may approximate the weighting function by $\zeta_r = t/\Delta t N_r$, $r = 1, 2, \dots, m$, as well. In this case, however, the integral formula (5.3) instead of (5.9) has to be used. Mathematically, these two formulations could achieve the same accuracy and possess a similar stability character. Nevertheless, the surface integrals appearing in (5.3) would affect the numerical computations due to the propagative nature of the hyperbolic system.

It is important to note that neither the use of $\zeta_r = t/\Delta t N_r$ nor $\zeta_r = (1 - t/\Delta t)N_r$ can always represent accurately the class of test functions having compact support on R if the conventional shape functions are used. These known classes of shape functions may not vanish or be equal to the same constant on all boundaries.

of the cylinder, R , although we have presumed that they do as required by the theorem of weak solutions. The error arising from this aspect, nevertheless, can be reduced easily by treating the boundary conditions with care during the numerical computations. Meanwhile, constructing a new class of shape functions does not seem to be practical due to the difficulties involved, and the serendipity elements will be used instead.

5.3 ISOPARAMETRIC ELEMENTS AND NUMERICAL INTEGRATION

As is seen, the use of finite elements discretizes a continuum problem and establishes a system of algorithm equations, whose coefficients are expressed in terms of the products of element shape functions. The choice of element type in finite element analysis is usually dictated by considerations of accuracy, computational efficiency, and the specific problem under study. As remarked in the previous subsection, the serendipity family will be used in the present study.

For three-dimensional finite element analysis, the "serendipity" elements with isoparametric formulation are superior to other solid elements with respect to the above considerations especially in the present problem where an adequate representation of the geometry is essential. The term "isoparametric" means that the same shape functions are used to define both the geometry and the unknown function. In the present study, use will be made of the linear, quadratic, and cubic elements of the "serendipity" family. After performing certain transformation (mapping), these brick-type elements will deform to yield curved surfaces. The following is a description of these elements.

5.3.1 Serendipity Elements

In the "serendipity" brick element, most of the nodes are located on external edges. In fact, the linear, quadratic, and cubic elements contain no internal nodes at all. The corresponding shape functions are listed on the following page:

Let

$$\xi_o = \xi\xi_i, \eta_o = \eta\eta_i \text{ and } \zeta_o = \zeta\zeta_i$$

where (ξ, η, ζ) are the local coordinates and (ξ_i, η_i, ζ_i) denote the coordinates of nodal points of the cube (see Fig. 5-1).

Linear Element (8 nodes)

The shape functions in this case are defined by

$$N_i = \frac{1}{8} (1 + \xi_o)(1 + \eta_o)(1 + \zeta_o), \quad i = 1, 2, \dots, 8$$

Quadratic Element (20 nodes)

For corner nodes

$$N_i = \frac{1}{8} (1 + \xi_o)(1 + \eta_o)(1 + \zeta_o)(\xi_o + \eta_o + \zeta_o - 2)$$

Typical mid-side node

$$\xi_i = 0, \eta_i = \pm 1, \zeta_i = \pm 1$$

$$N_i = \frac{1}{4} (1 - \xi^2)(1 + \eta_o)(1 + \zeta_o)$$

Cubic Element (32 nodes)

For corner nodes

$$N_i = \frac{1}{64} (1 + \xi_o)(1 + \eta_o)(1 + \zeta_o) \left[9(\xi^2 + \eta^2 + \zeta^2) - 19 \right]$$

Typical side node

$$\xi_i = \pm \frac{1}{3}, \eta_i = \pm 1, \zeta_i = \pm 1$$

$$N_i = \frac{9}{64} (1 - \xi^2)(1 + 9\xi_o)(1 + \eta_o)(1 + \zeta_o)$$

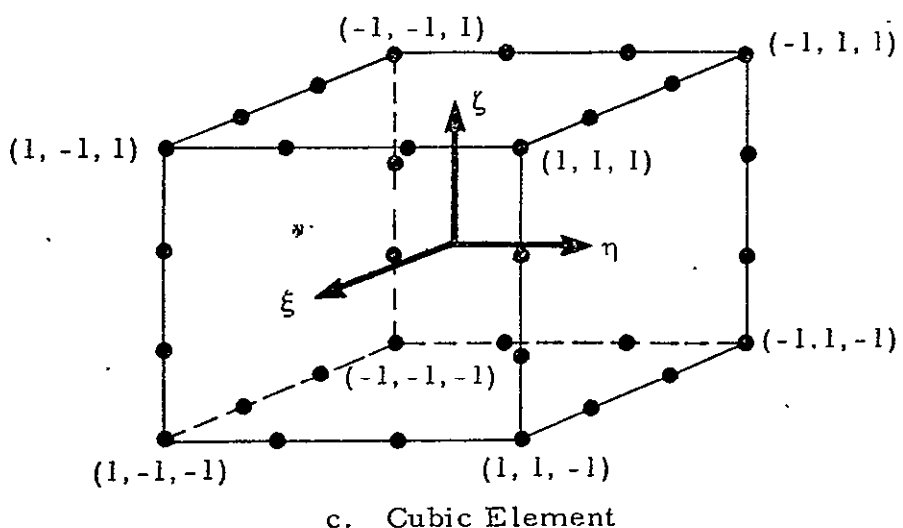
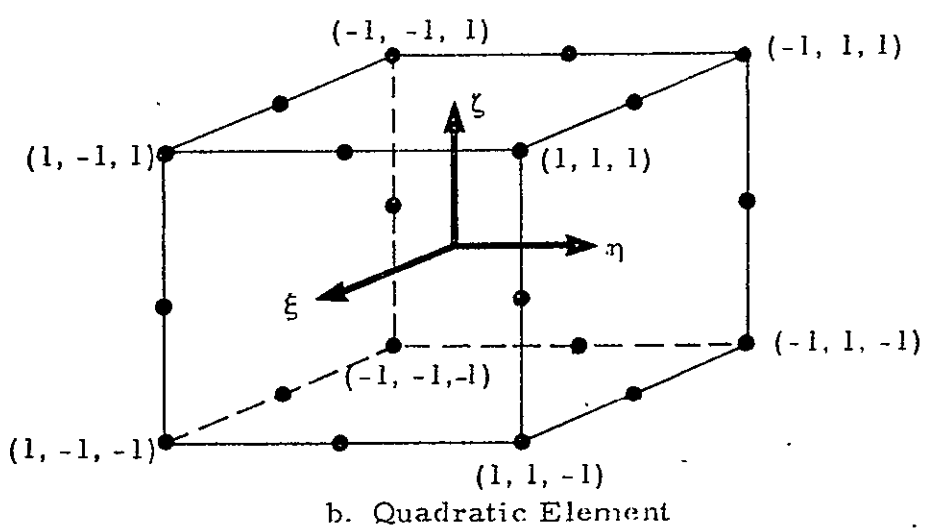
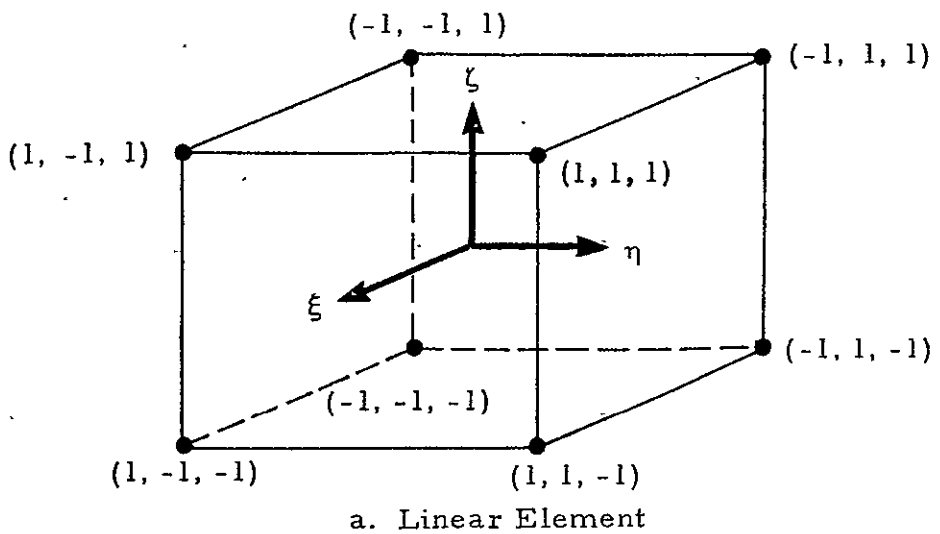


Fig. 5-1 - Location of Nodal Points in Three-Dimensional Elements

5.3.2 Numerical Integration

In finite element analysis, the matrices defining element properties, e.g., stiffness, etc., must be found. These will be of the form

$$I = \iiint [G(x, y, z)] dx dy dz \quad (5.23)$$

in which the expression G depends on the equation being solved and the shape functions N_i and/or their derivatives with respect to the global coordinate system (x, y, z) . As is seen earlier, the shape functions are written in the local coordinates (ξ, η, ζ) , therefore certain transformations must be performed so that Eq.(5.23) can be evaluated in the local coordinate system.

First, the expression $G(x, y, z)$, which involves shape functions N_i and their derivatives in the global coordinate system (x, y, z) must be transformed into those in the local coordinate system (ξ, η, ζ) . When isoparametric formulation is used, the relationship between global coordinates and local coordinates is defined by

$$\begin{aligned} x &= N_i(\xi, \eta, \zeta) x_i \\ y &= N_i(\xi, \eta, \zeta) y_i \quad (\text{sum on } i) \end{aligned} \quad (5.24)$$

and

$$z = N_i(\xi, \eta, \zeta) z_i$$

in which N_i are the shape functions as defined before and x_i, y_i, z_i represent the global nodal coordinates. By this transformation, the originally right prism in the (ξ, η, ζ) space will become distorted in the (x, y, z) space. Now, since the shape functions are defined locally in finite element analysis, no transformation is necessary. However, the derivatives of shape functions with respect to (x, y, z) must be transformed into the local coordinate system. This can be done as follows.

Using the chain rule, one has

$$\begin{Bmatrix} \frac{\partial N_i}{\partial \xi} \\ \frac{\partial N_i}{\partial \eta} \\ \frac{\partial N_i}{\partial \zeta} \end{Bmatrix} = \begin{bmatrix} \frac{\partial x}{\partial \xi} & \frac{\partial y}{\partial \xi} & \frac{\partial z}{\partial \xi} \\ \frac{\partial x}{\partial \eta} & \frac{\partial y}{\partial \eta} & \frac{\partial z}{\partial \eta} \\ \frac{\partial x}{\partial \zeta} & \frac{\partial y}{\partial \zeta} & \frac{\partial z}{\partial \zeta} \end{bmatrix} \begin{Bmatrix} \frac{\partial N_i}{\partial x} \\ \frac{\partial N_i}{\partial y} \\ \frac{\partial N_i}{\partial z} \end{Bmatrix} = [J] \begin{Bmatrix} \frac{\partial N_i}{\partial x} \\ \frac{\partial N_i}{\partial y} \\ \frac{\partial N_i}{\partial z} \end{Bmatrix} \quad (5.25)$$

where $[J]$ is the Jacobian matrix. Therefore, one obtains

$$\begin{Bmatrix} \frac{\partial N_i}{\partial x} \\ \frac{\partial N_i}{\partial y} \\ \frac{\partial N_i}{\partial z} \end{Bmatrix} = [J]^{-1} \begin{Bmatrix} \frac{\partial N_i}{\partial \xi} \\ \frac{\partial N_i}{\partial \eta} \\ \frac{\partial N_i}{\partial \zeta} \end{Bmatrix}$$

The Jacobian matrix $[J]$ and its inverse, in turn, can be determined from (5.25). More explicitly, the Jacobian matrix becomes

$$[J] = \begin{bmatrix} \frac{\partial N_1}{\partial \xi} & \frac{\partial N_2}{\partial \xi} & \dots \\ \frac{\partial N_1}{\partial \eta} & \frac{\partial N_2}{\partial \eta} & \dots \\ \frac{\partial N_1}{\partial \zeta} & \frac{\partial N_2}{\partial \zeta} & \dots \end{bmatrix} \begin{Bmatrix} x_1 & y_1 & z_1 \\ x_2 & y_2 & z_2 \\ \vdots & \vdots & \vdots \\ \vdots & \vdots & \vdots \end{Bmatrix} \quad (5.26)$$

and its inverse can be determined subsequently.

Secondly, a transformation for the volume element must also be done, that is

$$dxdydz = \det [J] d\xi d\eta d\zeta \quad (5.27)$$

By combining (5.26) and (5.27), one finally obtains, in place of (5.24), the following integral form

$$I = \int_{-1}^1 \int_{-1}^1 \int_{-1}^1 [\tilde{G}(\xi, \eta, \zeta)] d\xi d\eta d\zeta \quad (5.28)$$

Thus the integration is carried out within the right prism and not in the complicated distorted shape.

While the limits of the integration are simple in (5.28), unfortunately the explicit form of (\tilde{G}) is not. Therefore numerical integration usually has to be resorted to. Essentially, (5.28) is approximated by the following form:

$$I = \sum_{i=1}^n \sum_{j=1}^n \sum_{m=1}^n w_i w_j w_m [\tilde{G}(\xi_i, \eta_j, \zeta_m)] \quad (5.29)$$

In the above, w_i , w_j and w_m are the weighting coefficients with \tilde{G} evaluated at the point (ξ_i, η_j, ζ_m) . Herein, for simplicity, the number of integrating points in each direction was assumed to be the same. The numerical scheme presently used is the Gaussian quadrature, of which the points for evaluating \tilde{G} and hence the corresponding weights, are preselected to yield higher accuracy with a fixed number of integration points. Of course, within the isoparametric family, exact numerical Gaussian quadratures can be obtained if a sufficient number of points is used.

The surface integrals can be expressed in a similar form

$$I = \iint_S [H(x, y, z)] dS \quad (5.30)$$

in which $H(x, y, z)$ is obtained from the shape functions and/or their derivatives with respect to the global coordinate system (x, y, z) and S is a curved surface in space. Since the integrand is usually very complicated, expression (5.30) will be evaluated by numerical integration.

First, the expression $H(x, y, z)$ must be expressed in terms of the local coordinates (ξ, η, ζ) , analogous to the volume integrals, and to be evaluated on the appropriate surface. Second, a transformation for the area element must be done so that the integration is performed on the surface defined by two of the local coordinates. For instance, the area element on a surface where ζ is constant can be written as

$$dS = \det[\tilde{J}] d\xi d\eta \quad (5.31)$$

in which $[\tilde{J}]$ is the modified Jacobian matrix evaluated on the surface considered. The matrix, in turn, is defined as

$$[\tilde{J}] = \begin{bmatrix} \frac{\partial x}{\partial \xi} & \frac{\partial y}{\partial \xi} & \frac{\partial z}{\partial \xi} \\ \frac{\partial x}{\partial \eta} & \frac{\partial y}{\partial \eta} & \frac{\partial z}{\partial \eta} \\ \frac{\partial x}{\partial \zeta}/\ell & \frac{\partial y}{\partial \zeta}/\ell & \frac{\partial z}{\partial \zeta}/\ell \end{bmatrix} \quad (5.32)$$

with

$$\ell = \sqrt{\left(\frac{\partial x}{\partial \zeta}\right)^2 + \left(\frac{\partial y}{\partial \zeta}\right)^2 + \left(\frac{\partial z}{\partial \zeta}\right)^2}$$

The corresponding surface integral, through the above transformations, thus becomes

$$I = \int_{-1}^1 \int_{-1}^1 [\tilde{H}(\xi, \eta)] d\xi d\eta \quad (5.33)$$

Finally by using Gaussian quadrature, the surface integral is approximated by the following summation

$$I = \sum_{i=1}^n \sum_{j=1}^n w_i w_j [\tilde{H}(\xi_i, \eta_j)] \quad (5.34)$$

in which H is evaluated at the Gaussian points (ξ_i, η_j) , w_i, w_j are the corresponding weighting coefficients, and n denotes the total number of Gaussian points to be used in each direction.

5.4 GENERALIZED TWO-STEP, TIME-SPLITTING SCHEME

It is well known that the finite element method with conventional assembly techniques is equivalent to the centered finite difference scheme. When the method is applied to solve flow problems containing shock waves, numerical instabilities generally arise primarily due to the lack of dissipative terms. In the finite difference approach, this difficulty can be overcome by either one, or a combination, of the following schemes:

- Introducing artificial viscosity
- Replacing the center difference by a noncentric difference scheme,
- Utilizing the two-step finite-difference scheme, or
- Introducing Lax-Wendroff's second order correction, etc.

All of the above variations except the second have been adopted in the current finite element codes to solve the impact problem. It was found that the last two approaches yielded promising results. However, due to the excessive computation time needed with the Lax-Wendroff second order scheme, we have decided to adopt the two-step, time-splitting procedure.

Consider a non-linear matrix equation

$$([A_{rs}] - \Delta t \theta [B_{rs}]) \{\phi_s^{(n+1)}\} = ([A_{rs}] + \Delta t (1-\theta) [B_{rs}]) \{\phi_s^{(n)}\} + \Delta t \{C_r\} \quad (5.35)$$

where θ is a non-negative factor, $[A_{rs}]$, $[B_{rs}]$ are square matrices, $\{C_r\}$ is a column matrix, and $\phi^{(n)}$ denotes the solution of ϕ at the n^{th} step. In the present case, the factor $\theta = 1/3$, the matrices are

$$A_{rs} = \int_{\Omega} N_r N_s d\Omega,$$

and

$$B_{rs} = \int_{\Omega} \left[\Omega_k \frac{\partial N_r}{\partial x_k} + \Lambda N_r \right] N_s d\Omega \quad r, s = 1, 2, \dots, \ell$$

and the vector

$$C_r = \int_{\Omega} \left\{ \frac{\partial N_r}{\partial x_k} H^k + N_r G \right\} d\Omega$$

where $H^k = F^k - v_k \phi$.

Following the general approach of two-step procedure (see Richtmyer and Morton [32]), the solution of (5.35) can be obtained by the following steps:

$$\left([A_{rs}] + a \Delta t \theta [B_{rs}^{(n)}] \right) \overline{\phi_s^{(n+a)}} = \left([A_{rs}] + a \Delta t (1-\theta) [B_{rs}^{(n)}] \right) \{ \phi_s^{(n)} \} + a \Delta t \{ C_r^{(n)} \} \quad (5.36)$$

$$\left([A_{rs}] - \Delta t \theta [\tilde{B}_{rs}^{(n+1)}] \right) \{ \phi_s^{(n+1)} \} = \left([A_{rs}] + \Delta t (1-\theta) [\tilde{B}_{rs}^{(n+1)}] \right) \{ \phi_s^{(n)} \} + \Delta t \{ \tilde{C}_r^{(n+1)} \}$$

where

$$\tilde{B}_{rs}^{(n+1)} = \alpha B_{rs}^{(n)} + (1-\alpha) \bar{B}_{rs}^{(n+a)}$$

$$\tilde{C}_r^{(n+1)} = \alpha C_r^{(n)} + (1-\alpha) \bar{C}_r^{(n+a)}$$

Here α is a relaxation factor, and the constant a may be an integer or a fraction multiplier of the time step. As will be seen in Section 7, the numerical

computations become more stable as the parameter α increases. The mathematical aspect of the present formulation is yet to be studied in-depth. In particular, the relation between α and the ratio of the time step size and the element size must be determined in order to obtain an optimal accuracy for the general impact problems.

6. COUPLED EULERIAN-LAGRANGIAN FINITE ELEMENT (CELFE) CODE

The complete CELFE program to be constructed follows the requirements discussed in Section 2, i.e., it contains the capabilities of

- Simulating the transient state during the impact process and right after the process is completed
- Computing the dynamic response of the entire structure for specified times after the impact process is completed, and
- Detecting various criteria during the impact process, e.g., rebounding, sliding, penetration, together with tracing the movement of the free surface, failure front, etc.

In the present study, however, we are mainly concerned with the development of the transient analysis modules. This aspect will be emphasized in the following discussions.

6.1 BASIC IDEAS AND FORMULATION

In this section, a preliminary discussion of the procedure for transient analysis is given. We shall regard the procedure as the principal CELFE procedure or simply the CELFE procedure.

The CELFE procedure can be divided into three parts: the first part contains a finite element module based on the algorithm formulated in Section 5 to simulate the dynamic behavior in the impact zone; the second part is a classical finite element procedure for analyzing the dynamic response in the Lagrangian zone; and the third part consists of a coupling (interfacing) procedure to integrate the above two separate parts to form a complete system, i.e., the complete CELFE system.

The complete CELFE system to be developed in this section consists of two options, namely, an in-core CELFE code and a coupled CELFE-NASTRAN code. The in-core option is built as a substructure of the coupled option to allow more flexibility in utilizing the computer code.

6.1.1 Definitions and Preliminary Discussions

Recall that the entire structure has been partitioned into an impact zone and a structural (Lagrangian) zone. The impact zone consists of an Eulerian zone (E zone) and a transition zone (E-L zone).

Based on the above discussions, the Lagrangian zone (L zone) can be divided into an in-core and a NASTRAN zone according to the options of the in-core CELFE code and the coupled CELFE-NASTRAN code. The zonings can be denoted as L_c zone and L_N zone, respectively. Since the in-core option is contained in the coupled option, the Lagrangian zone (L zone) may be composed solely of L_c when the in-core option is used; or composed solely of L_N or mixed L_c and L_N when the coupled option is used.

In the entire impact zone, together with the L_c zone, three-dimensional solid elements have to be used. In the remaining portion of the structure, i.e., the L_N zone, any appropriate elements (depending on the nature of the structure) can be applied. A typical arrangement of the elements is illustrated in Fig. 6-1. Here, once again we stress that:

- In the impact zone (i.e., E zone and E-L zone), the dynamic behavior will be handled by the algorithm developed in Section 5 using the hydro-elasto-viscoplastic model represented by a general moving coordinate system. The primary variables in this zone consist of the density, ρ , momentum, ρv_j , $j = 1, 2, 3$, total energy, ρe , and deviatoric stresses, S_{ij} , $i, j = 1, 2, 3$; the remaining variables, i.e., the pressure P , stresses σ_{ij} , and the displacements u_j , etc., belong to the secondary variable.
- In the Lagrangian zone composed of the L_c and L_N zones, traditional structural dynamic analyses will be applied. In this study, the displacement method is adopted, and thus the displacements

6-3

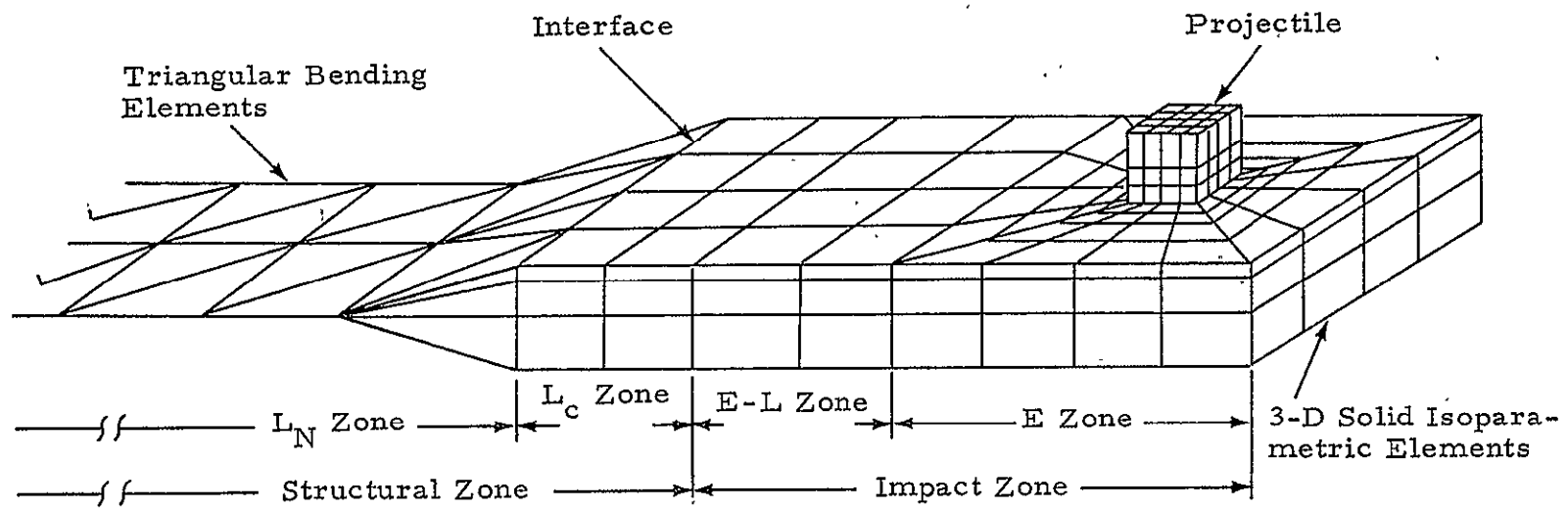


Fig. 6-1 - Typical Finite Element Sketch in Global Analysis of High Velocity Impact

(both the lateral and rotational displacements) are chosen to be the primary variables.

- Since the governing equations, coordinate systems and types of elements in the various zones are different in nature, the coupling procedure must provide two mechanisms, namely, an in-core procedure to couple the E-L and L_c zones (or L_N zone in case of empty L_c); and an interfacing procedure to couple the main CELFE program with NASTRAN. The coupling variables for the present procedure contain lateral displacement and velocity fields.

The associate variables, types of elements, and related aspects concerning the above discussions for various zones are summarized in Table 6-1.

6.1.2 Governing Equations

For the transient state, i.e., during the penetration process and right after the process is completed, the dynamic behavior in the impact zone and in the Lagrangian zone are governed by different sets of equations as discussed in Sections 3 and 4. The equations are recalled as follows:

For the impact zone, the equations are represented in a general moving coordinate system by the conservation form

$$\frac{\partial \phi}{\partial t} + \frac{\partial F^k}{\partial x_k} = \Lambda \phi + G(x, t) \quad (6.1)$$

where

$$\phi = \begin{cases} \rho \\ v_j; j = 1, 2, 3 \\ E \\ S_{ij}; i, j = 1, 2, 3 \end{cases}$$

$$F^k = \begin{cases} \Omega_k \rho \\ \Omega_k v_j - \sigma_{jk}; j = 1, 2, 3 \\ \Omega_k E - \sigma_{\ell k} v_\ell \\ \Omega_k S_{ij}; i, j = 1, 2, 3 \end{cases}; k, \ell = 1, 2, 3$$

Table 6-1
CLASSIFICATIONS OF VARIOUS ZONES IN HIGH VELOCITY IMPACT

Classification of Zones	Impact Zone		Lagrangian Zone	
	E-Zone	E-L Zone	L_c Zone	L_N Zone
	Eulerian Zone (Empty at $t=0$)	Transition Zone	In-Core Lagrangian Zone (May be Empty)	NASTRAN Zone (May be Empty)
Primary Variables	$\rho, \rho v_j, \rho e, S_{ij}; i, j = 1, 2, 3$		$u_j, \theta_j; j = 1, 2, 3$	
Secondary Variables	$u_j, P, \sigma_{ij}; i, j = 1, 2, 3$		$\dot{u}_j, \dot{\theta}_j; j = 1, 2, 3$ ($\dot{u}_j = v_j$)	
Type of Elements	3-D Isoparametric Elements		3-D Isoparametric Elements	Any Compatible Elements
Coupling Variables	$v_j, u_j; j = 1, 2, 3$			

$$\Lambda \phi = \left\{ \begin{array}{l} \rho \frac{\partial}{\partial x_k} (\Omega_k - v_k) \\ V_j \frac{\partial}{\partial x_k} (\Omega_k - v_k) \\ E \frac{\partial}{\partial x_k} (\Omega_k - v_k) \\ S_{ij} \frac{\partial \Omega_k}{\partial x_k}; i, j = 1, 2, 3 \end{array} \right\}; k = 1, 2, 3$$

$$G = \left\{ \begin{array}{l} 0 \\ F_j; j = 1, 2, 3 \\ F_\ell v_\ell \\ C_{ijkl} d_{kl}^{e'} - S_{im} \omega_{mj} + S_{mj} \omega_{im}; i, j = 1, 2, 3 \end{array} \right\}; k, \ell = 1, 2, 3 \quad (6.2)$$

For the Lagrangian zone, the small deformation is assumed in this study, and the governing equations are given as

$$\overset{\wedge}{\rho} \delta + B \dot{\delta} + K \delta = G \quad (6.3)$$

In the L_c zone where three-dimensional isoparametric elements are used (cf. Table 6-1), we have

$$\begin{aligned} \delta &= \left\{ u_j; j = 1, 2, 3 \right\} \\ \overset{\wedge}{\rho} &= \rho v_j = V_j; j = 1, 2, 3 \\ B &\equiv 0 \end{aligned}$$

$$K = \left\{ -\frac{1}{2} \frac{\partial}{\partial x_k} (C_{jklk} \frac{\partial}{\partial x_k}) \overset{\wedge}{\delta}_{kl}; j = 1, 2, 3 \right\}; k, \ell = 1, 2, 3$$

$$G = \left\{ \frac{\partial}{\partial x_j} (C_{jklk} \frac{\partial u_k}{\partial x_k}) + \frac{1}{2} \frac{\partial}{\partial x_k} (C_{jklk} \frac{\partial u_k}{\partial x_j}) + F_j; j = 1, 2, 3 \right\}; k = 1, 2, 3 \quad (6.4)$$

where δ_{ij} denotes the Kronecker delta, and the damping term has been included in the forcing term G . In the L_N zone, on the other hand,

$$\delta = \begin{cases} u_j; j = 1, 2, 3 \\ \theta_j; j = 1, 2, 3 \end{cases} \quad (6.5)$$

and $\hat{\rho}$, B , K and G are given according to the nature of the problem.

6.1.3 Coupling Procedure

As mentioned previously, the coupling variables to be used in the CELFE code are u_j and v_j , $j = 1, 2, 3$. This set of variables provides a straightforward coupling procedure, i.e., the impact zone may be considered as a substructure of the Lagrangian zone where the global finite element matrix equation for u_j and v_j contain a submatrix equation representing the impact zone. This coupling procedure is called here the direct method. One may also use the substructural approach developed by Przemieniecki (Ref. 35), which we may call an indirect method.

It will be seen that the direct method is simpler, and the in-core coupling procedure proceeds automatically in the CELFE program following the transition of the relative velocity Ω_k from v_k to 0 for $k = 1, 2, 3$. There is a drawback, however, in that its in-core capability is limited by the computer storage. Since our objective is to couple CELFE with NASTRAN in the first place, this drawback is not important.

Although the indirect method may extend the capability of the in-core CELFE option (in exchange for increasing the computation time due to the complexity in the coupling process), the size of the problems that can be handled will still be limited compared to NASTRAN. Thus, this approach turns out to be impractical for the present study.

In view of the above discussions, the direct method is chosen here for the coupling procedure of the CELFE code. By definition, the displacement

field is given as:

$$\dot{u}_j = v_j, \quad j = 1, 2, 3 \quad (6.6)$$

In the impact zone, however, the velocity field is represented by a general moving coordinate system, $\dot{u}_j \neq \dot{x}_j$, and follows the identity (Eq. (3.3)). From the expression (Eq. (3.9)), Eq. (6.6) yields a conservation form

$$\frac{\partial u_j}{\partial t} + \frac{\partial}{\partial x_k} (\Omega_k u_j) = \Lambda u_j + u_j, \quad j = 1, 2, 3 \quad (6.7)$$

where

$$\Lambda = \frac{\partial \Omega_k}{\partial x_k}$$

is the divergence of the relative velocity.

Across the impact zone, the relative velocity Ω_k , $k = 1, 2, 3$, governed by Eq. (6.7), will change from $\Omega_k = v_k$ in the E zone in such a manner that, in E-L zone,

$$\tilde{\Omega} = N_s \left[(1 - \frac{t}{\Delta t}) \tilde{\Omega}_s^{(n)} + \frac{t}{\Delta t} \tilde{\Omega}_s^{(n+1)} \right] \quad (6.8)$$

for $s = 1, \dots, m$. At the nodes on the failure front, Ω_k begins to vanish and remains at zero up to the edge of the impact zone, i.e., the interface between the impact zone and L_c (or L) zone. Then, the governing equations (6.7) are replaced by (6.3) throughout the Lagrangian zone.

Noting that Eq. (6.8) can be verified by the definition Eq. (3.3), the relation ensures that at any instance the mesh in the E-L zone will remain simply connected. In addition, since the finite element approximation is taken as the average of the solution-field element wise, Eq. (6.8) ensures that the solutions in the E-L zone will maintain the same accuracy as in the remaining part without adjusting the manipulations explicitly when intrusion of the Lagrangian mesh into the originally Eulerian mesh occur. This significantly simplifies the program for the coupling procedure compared to finite difference techniques.

6.2 FINITE ELEMENT FORMULATION FOR TRANSIENT ANALYSIS

The principal function of the CELFE code is to simulate the dynamic behavior during the penetration process and right after the process is completed. The finite element formulations to be discussed in the following are directed mainly for this principal function.

6.2.1 Finite Element Module for Impact Zone

The stated module consists of a procedure to solve the system (Eq. (6.1)) with listed primary variables (cf. Table 6-1). The finite element analog of Eq. (6.1) is readily obtained, as shown in Section 5, based on the theorem of weak solutions, i.e.,

$$([A_{rs}] - \frac{\Delta t}{3} [B_{rs}]) \{ \phi_s^{(n+1)} \} = ([A_{rs}] + \frac{2 \Delta t}{3} [B_{rs}]) \{ \phi_s^{(n)} \} + \Delta t \{ C_r \} \quad (6.9)$$

where

$$\begin{aligned} A_{rs} &= \int_{\Omega_e} N_r N_s d\Omega \\ B_{rs} &= \int_{\Omega_e} \left[\Omega_k \frac{\partial N_r}{\partial x_k} + \Lambda N_r \right] N_s d\Omega \\ C_r &= \int_{\Omega_e} \left[H^k \frac{\partial N_r}{\partial x_k} + G N_r \right] d\Omega \end{aligned} \quad (6.10)$$

with $H^k = F^k - \Omega_k \phi$, and the primary variables

$$\phi = \left\{ \begin{array}{l} \rho \\ V_j; j = 1, 2, 3 \\ E \\ S_{ij}; i, j = 1, 2, 3 \end{array} \right\}$$

The system (Eq. (6.9)) is solved independently (in the impact zone) from the remaining zone. Its solution provides a finite element approximation of the nonlinear behavior in the vicinity of the impact point due to large deformation, in particular, the failure. The momentums, v_j , $j = 1, 2, 3$, in addition, will serve as "known" functions, dividing by ρ , for the coupling procedure characterizing the velocity field in the impact substructure.

6.2.2 Finite Element Analogs for Displacements in Various Zones

Since the coupling procedure is formulated by the direct method introduced in Section 6.1.4, a global system of finite element equations is required for the displacement field covering the entire structure. This finite element system is constructed by summing up the subsystems deduced from Eq. (6.7) and Eq. (6.3) for the impact zone and Lagrangian zone, respectively.

Impact Zone: The finite element analog of Eq. (6.7) can be obtained following the weak solution formulation discussed in Section 5, namely,

$$([A_{rs}] - \frac{\Delta t}{3} [B_{rs}]) \{u_{js}^{(n+1)}\} = ([A_{rs}] + \frac{2 \Delta t}{3} [B_{rs}]) \{u_{js}^{(n)}\} + \Delta t \{C_r\} \quad (6.11)$$

Here,

$$\begin{aligned} A_{rs} &= \int_{\Omega_e} N_r N_s d\Omega \\ B_{rs} &= \int_{\Omega_e} \left[\Omega_k \frac{\partial N_r}{\partial x_k} + \Lambda N_r \right] N_s d\Omega \\ C_r &= \int_{\Omega_e} v_j N_r d\Omega \end{aligned} \quad (6.12)$$

and the velocity field v_j in C_r is determined by the formulation presented in the previous subsection.

Lagrangian Zone: Since the form (Eq. (6.3)) depends on the model used for a specific problem, it can be approximated using different types of elements with different forms associated with the model. Numerous forms have been developed and are available in the literature. Symbolically, the form is represented by

$$[\mathbf{M}] \begin{Bmatrix} \ddot{\delta} \\ \vdots \end{Bmatrix} + [\mathbf{B}] \begin{Bmatrix} \dot{\delta} \\ \vdots \end{Bmatrix} + [\mathbf{K}] \begin{Bmatrix} \delta \\ \vdots \end{Bmatrix} = \begin{Bmatrix} \mathbf{G} \\ \vdots \end{Bmatrix} \quad (6.13)$$

The integration with respect to time in Eq. (6.13) can be obtained either by a finite difference or finite element scheme. In NASTRAN, and thus in the L_N zone of the present analysis, the finite difference procedure is used (cf. Ref. 36). Whereas in the L_C zone, where three-dimensional solid elements are utilized, the finite element in time formulated by Zienkiewicz (Ref. 37, Section 16.5, pp. 335-342) is preferred.

Let p represent either finite element or finite difference discretization of d/dt . Then Eq. (6.13) yields

$$\left\{ [p^2 \mathbf{M}] + [p \mathbf{B}] + [\mathbf{K}] \right\} \begin{Bmatrix} \delta \\ \vdots \end{Bmatrix} = \begin{Bmatrix} \mathbf{G} \\ \vdots \end{Bmatrix} \quad (6.14)$$

6.2.3 Finite Element Formulation of Coupling Process

As mentioned previously, when the direct method is adopted to couple the Eulerian and Lagrangian modes, it is necessary to formulate a global system of matrix equations for the displacement field in such a way that:

- The system covers both the impact zone and the Lagrangian zone, and
- The system is constructed by summing up the finite element analog (Eq. (6.11)) when the element belongs to the impact zone and Eq. (6.14) when the element belongs to the Lagrangian zone.

Let a superscript, e , denote the element value of a given physical quantity, and subscripts E-L and L denote the corresponding quantity defined in the impact zone and Lagrangian zone, respectively. Let also

$$[K_j]_{E-L} = [A_{rs}] - \frac{\Delta t}{3} [B_{rs}]$$

$$\left\{G_j\right\}_{E-L} = ([A_{rs}] + \frac{2\Delta t}{3} [B_{rs}]) \left\{u_j^{(n)}\right\}_{s} + \Delta t \left\{C_r\right\}$$

for $j = 1, 2, 3$, where $[A_{rs}]$, $[B_{rs}]$, and $\left\{C_r\right\}$ are defined in Eq. (6.12). Then, Eq. (6.11) can be written as

$$[K_j]_{E-L} \left\{u_j\right\}_{E-L}^{(e)} = \left\{G_j\right\}_{E-L}^{(e)} \quad (6.15)$$

Similarly, we may write Eq. (6.14) in the following form

$$\left\{[p^2 M]_L + [pB]_L + [K]_L\right\} \left\{\delta\right\}_L^{(e)} = \left\{G\right\}_L^{(e)} \quad (6.16)$$

Summing Eqs. (6.15) and (6.16) over $e = 1, 2, \dots, M$, yields

$$\left\{[p^2 M] + [pB] + [K]\right\} \left\{\delta\right\} = \left\{G\right\} \quad (6.17)$$

where M is the total number of elements in the entire structure, including the projectile.

Noting that the actual coupling variables consist of lateral displacements and velocities, u_j and v_j , $j = 1, 2, 3$, in the impact zone the lateral velocity (momentum) field is categorized as primary variables, and is obtained following the procedure given in Section 6.2.1. Whereas, the lateral displacement field belongs to the secondary. In the Lagrangian zone, on the other hand, Eqs. (6.3), (6.4) and (6.5) indicate that, in general, there are six degrees of freedom (i.e., six primary variables) composed of three lateral and three angular displacements. The velocities, in turn, become secondary.

Therefore, when we sum Eqs. (6.15) and (6.16) to form (6.17), we must be aware of the arrangement of the matrices $[K_j]_{E-L}$, $j = 1, 2, 3$ and $[K]_L$, such that the elements of the matrices can follow the permutation of u_j , θ_j ,

$j = 1, 2, 3$ in the vector $\{\delta\}$ of Eq. (6.17). Furthermore, we notice that, in the matrices $[p^2 M]$ and $[pB]$, all elements corresponding to those grids in the impact zone are set to zero. Since, as formulated in Section 5, all the inertial effects appearing in Eq. (6.7) have been integrated by finite element in time a priori, and are included in $[K_j]_{E-L}$.

It is important to mention that the displacements computed by Eq. (6.17) for those grids in the impact zone do not represent the movement of the same material particles at any instance. Instead, they represent those for different material particles at various times that occupy the given grids at that instance. In the E-zone, which is composed of material failure, the grid points are fixed in the space. In the E-L zone, the grid points move with the relative velocity Ω with respect to the particles occupying those grids at that instance. Thus, in the E-L zone, the grids must be updated according to the definition (Eq. (3.3)) by letting Ω_k vary from $\Omega_k = v_k$ in the E zone to $\Omega_k = 0$ on the interface of the E-L zone and L_c zone.

The solution of Eq. (6.17) for those grids belonging to the Lagrangian zone, on the other hand, satisfy the small deformation theory. Thus, the grids in this region do not require updating, except those on the interface of the E-L and L_c zones. It can be expected, however, that the deviation on these interface nodes will be negligible compared to those in the impact zone.

6.3 RELEVANT CRITERIA IN CELFE SYSTEM

We are now ready to formulate the numerical procedure for the complete CELFE system. The principal part of the CELFE system has been concerned with the analysis of the dynamic behavior of the target during and right after the penetration process. As mentioned previously, however, the complete CELFE system must have the capability to simulate various circumstances when certain criteria are detected during the computations.

The criteria related to the CELFE procedure can be classified into two categories: (1) the criteria arising from the impact process; and (2) the criteria describing the degeneracy of the dynamic behavior with respect to time due to damping effects.

The present code consists of three possible impact cases, namely, the penetration process composed of the principal portion of the code; the rebound of the projectile from the target; and the sliding of the projectile on the target surface. It is clear that the penetration process follows the failure criterion; and the criterion for rebound is rather straightforward. Thus, in what follows, only the failure and sliding process will be presented.

6.3.1 Numerical Procedure for Predicting Material Failure

The failure criteria for fibrous composites and isotropic materials have been discussed in Section 3. The numerical procedure for predicting material failure using these criteria are different in CELFE as presented in the following.

Orthotropic Materials: For fiber composites, Chamis' criterion states that:

$$\begin{aligned} F(\sigma_\ell, S_\ell, K_\ell) &> 0 && \text{no failure} \\ F(\sigma_\ell, S_\ell, K_\ell) &= 0 && \text{incipient failure} \\ F(\sigma_\ell, S_\ell, K_\ell) &< 0 && \text{failure} \end{aligned} \quad (6.18)$$

where

$$\begin{aligned} F(\sigma_\ell, S_\ell, K_\ell) = 1 - & \left[\left(\frac{\sigma_{\ell 11\alpha}}{S_{\ell 11\alpha}} \right)^2 + \left(\frac{\sigma_{\ell 22\beta}}{S_{\ell 22\beta}} \right)^2 + \left(\frac{\sigma_{\ell 33\gamma}}{S_{\ell 33\gamma}} \right)^2 + \left(\frac{\sigma_{\ell 23S}}{S_{\ell 23S}} \right)^2 + \left(\frac{\sigma_{\ell 13S}}{S_{\ell 13S}} \right)^2 \right. \\ & + \left(\frac{\sigma_{\ell 12S}}{S_{\ell 23S}} \right)^2 - K_{\ell 23\beta\gamma} \frac{\sigma_{\ell 22\beta}}{S_{\ell 22\beta}} \frac{\sigma_{\ell 33\gamma}}{S_{\ell 33\gamma}} - K_{\ell 13\alpha\gamma} \frac{\sigma_{\ell 11\alpha}}{S_{\ell 11\alpha}} \frac{\sigma_{\ell 33\gamma}}{S_{\ell 33\gamma}} \\ & \left. - K_{\ell 12\alpha\beta} \frac{\sigma_{\ell 11\alpha}}{S_{\ell 11\alpha}} \frac{\sigma_{\ell 22\beta}}{S_{\ell 22\beta}} \right] \end{aligned} \quad (6.19)$$

(cf. Section 3.4.2). Here, the stresses are computed from Eqs. (6.9) and (3.21).

The application of Eq. (6.19) for the nonlinear analysis of material is suggested as follows (Ref. 28):

- Using the current load $\sigma_{ij}^{(n+1)}$ obtained from Eq. (6.9) and Eq. (3.21), compute F of Eq. (6.19).
- Test the value of F according to Eq. (6.18). If $F(\sigma_\ell, S, K) = 0$, then determine the minimum magnitude of the various stress ratios:

$$\text{Max}\left(\frac{\sigma_{\ell 11\alpha}}{S_{\ell 11\alpha}}, \frac{\sigma_{\ell 22\beta}}{S_{\ell 22\beta}}, \frac{\sigma_{\ell 33\gamma}}{S_{\ell 33\gamma}}, \frac{\sigma_{\ell 23S}}{S_{\ell 23S}}, \frac{\sigma_{\ell 13S}}{S_{\ell 13S}}, \frac{\sigma_{\ell 12S}}{S_{\ell 12S}}\right)$$

where α, β , and γ equal T or C.

- Assuming that the stress ratio $(\sigma_{\ell 22T}/S_{\ell 22T})$ is maximum, then in the next and subsequent time steps, let $E_{\ell 22}, v_{\ell 21}, v_{\ell 23}, K_{\ell 12}$ and $K_{\ell 23}$ be zero. The procedure is similar for other stress ratios or combinations.

Isotropic Materials: For isotropic materials, a tentative stress approach suggested in Ref. 10 is used. The procedure can be stated as follows:

- Using the current tentative stresses, $(S_{ij}^{(n+1)})^*$ computed from Eq. (6.9), test the yielding criterion. If

$$(S_{ij}^{(n+1)})^* (S_{ji}^{(n+1)})^* \geq \frac{2}{3} Y^2 \quad (6.20)$$

then, the tentative stresses are corrected according to the formula

$$S_{ij}^{(n+1)} = (1 - \beta) (S_{ij}^{(n+1)})^* \quad (6.21)$$

where

$$\beta = 1 - \frac{\sqrt{2/3} y^2}{\left[(S_{ij}^{(n+1)*}) \cdot (S_{ji}^{(n+1)*}) \right]^{1/2}}$$

6.3.2 Sliding Due to Oblique Impact

There are two types of sliding between projectile and target surfaces, i.e., the sliding of a projectile on the target surface due to oblique impact, and the separations due to spallation. Since the failure zone has been modeled by viscoplastic flow, only the sliding of the first type needs to be considered in this code.

Accordingly, the sliding due to oblique impact can be characterized by the following two factors:

- Surface friction between the target and projectile when there is no failure on the surfaces; and
- Slip flow of viscoplastic fluids when failure occurs on the surfaces.

When there is no failure immediately after the impact, only the first factor will be taken into account throughout the sliding process, and the projectile will eventually separate from the target. Otherwise, a mixed effect will arise and the projectile may either stop and adhere somewhere on the target, or rebound away depending on the process.

The criterion that covers both factors can be obtained using a modified Coulomb's friction law:

$$\begin{aligned} |f_t| &\leq \mu |f_n|, && \text{for no sliding} \\ |f_t| &= \mu |f_n| && \text{for sliding onset} \end{aligned} \tag{6.23}$$

where f_t is the tangential force on the impact surface, f_n is the normal compressive force on the surface, and μ is a friction factor. For the first case where no failure occurs, Eq. (6.19) reduces to the classical Coulomb's law,

and μ is the Coulomb friction coefficient. For the second case, μ can be correlated to the slip flow criterion. In the present case, it depends on the ratios $C_{3j}3j/C_{3333}$, $j = 1, 2$, of the target as well as the projectile, together with the surface tension on the sliding surface where material failure is detected. In general, we have $\mu = 1 + \gamma$, where γ is the specific free energy per unit area.

6.3.3 Degeneracy Due to Damping

For large t after the penetration process is completed, the damping effects of the structure may smear out the disturbances and reduce the hydrodynamic pressure to some extent, such that the nodal values of the velocity

$$\underline{v} = o(\underline{v}_0) \quad \text{in the entire structure} \quad (6.24)$$

where \underline{v}_0 is the impact velocity. It can be easily verified that the governing equations (6.1) for the impact zone are a system of degenerate equations for $t > t_d$, where t_d is some positive constant that Eq. (6.24) holds for all $t > t_d$. For $t_d < t < t_s$, where the local acceleration $\partial\underline{v}/\partial t$ remains $O(1)$, the continuity equation and energy equation in (6.1) become trivial; and the momentum equations degenerate to (6.3) with relation (6.4) after some manipulation. Thus, for all $t > t_d$, the dynamic behavior in the entire structure satisfies (6.3), i.e., the small deformation theory holds for the entire structure. As t increases further to $t > t_s$, the damping effects will lead the structure to a static state, i.e., Eq. (6.3) will finally approach the Navier equations.

Based on the formulation given in Section 5, where the conservation form Eq. (6.1) was used, the finite element analog will become singular for all $t > t_d$. In the present code, a criterion is set to specify the characteristic time t_d , so that the mesh of the entire system becomes Lagrangian for all $t > t_d$. Then, the computations will switch from coupled Eulerian-Lagrangian modes to purely Lagrangian satisfying Eq. (6.16) for the entire structure. The criterion is set in such a way that the velocity (momentum) field and/or pressure field are comparatively uniformly distributed in the

entire system (target and projectile) with maximum amplitudes reaching a certain fraction of the initial peaks, and there is no further failure.

6.4 NUMERICAL PROCEDURE FOR THE COMPLETE CELFE SYSTEM

In this subsection, the complete procedure for the CELFE system covering the previously discussed aspects is presented. The procedure includes both the in-core option and the coupled CELFE/NASTRAN option.

The CELFE procedure can be stated as follows:

1. The entire CELFE system is integrated with respect to time using the generalized two-step time integration scheme discussed in Section 5.3. For the coupled CELFE/NASTRAN option, the scheme may not be necessary to include the NASTRAN part. In the present code, it is included for the sake of simplicity in constructing the interface procedure.
2. A unique procedure composed of the following steps is used for both the in-core and coupled CELFE/NASTRAN options. For each time step:
 - Predict the solutions of primary variables in various zones from the corresponding equations using the results obtained in the previous time step.
 - Construct the global system matrix equation for the entire structure in terms of coupling variables, and solve the equation using the solution obtained in the previous time step.
 - Update the secondary variables in various zones using the above predicted values.
 - Update the mesh in the E-L zone and/or L_c zone.
 - Correct the results by repeating the process using the above predicting solutions together with the results obtained in the previous time step.
 - Test the corrected results to observe which criterion stated in the Introduction of this section will be satisfied, e.g., whether the projectile will rebound, slide, or penetrate, etc.
3. If the test shows the penetration process is still taking place, repeat the procedure stated in (2) for the next time step. Otherwise, we have:
 - After the projectile rebounds from the target, and/or disturbances in the structure are damped to a certain

fraction of the original values, the program will regard the entire structure as a Lagrangian zone and the dynamic response will be handled accordingly.

- If the projectile slides over the target due to oblique impact, the mesh for the entire structure will be set to be Lagrangian. Then repeat the procedure described in (2).

The flow chart depicted in Fig. 6-2 illustrates the above stated procedure. In order to maintain the accuracy of computations in the vicinity of the impact point, as well as a workable in-core storage and a straightforward programming, the dimension of the impact zone in this code will be appropriately chosen a priori. At $t = 0$, the entire impact zones are identical with the E-L zone, where the zone is initially discretized into Lagrangian mesh, i.e., letting $\Omega_k \equiv 0$ for all $k = 1, 2, 3$. For $t > 0$, when the failure is detected at certain nodes, the mesh containing these failure nodes is turned to Eulerian enveloped by a Lagrangian moving front. Hence, the impact zone, whose dimension has to be specified a priori, must be sufficiently large to contain the failure region up to the impact process completion. If excessively large impact zones are assigned, on the other hand, it will require unnecessary computer storage and computational time.

6.5 INTERFACING PROCEDURE FOR CELFE/NASTRAN

The interfacing procedure is constructed for solving large structural systems to remove any limitation of the size of the CELFE program due to excessive CELFE program core requirements. The procedure is built-in as a part of the coupling procedure to handle either or both of the following:

- Utilizing the matrix equation solver SOLVE of NASTRAN to obtain the solution of Eq. (6.9) in the impact zone; and/or
- Coupling the Eulerian and Lagrangian modes for the entire structural system.

6.5.1 Utilization of NASTRAN Subroutine SOLVE as Equation Solver

Symbolically, Eq. (6.9) can be rewritten for each element in the impact zone as

$$A^{(\alpha)} \phi^{(\alpha)} = B^{(\alpha)} \quad (6.25)$$

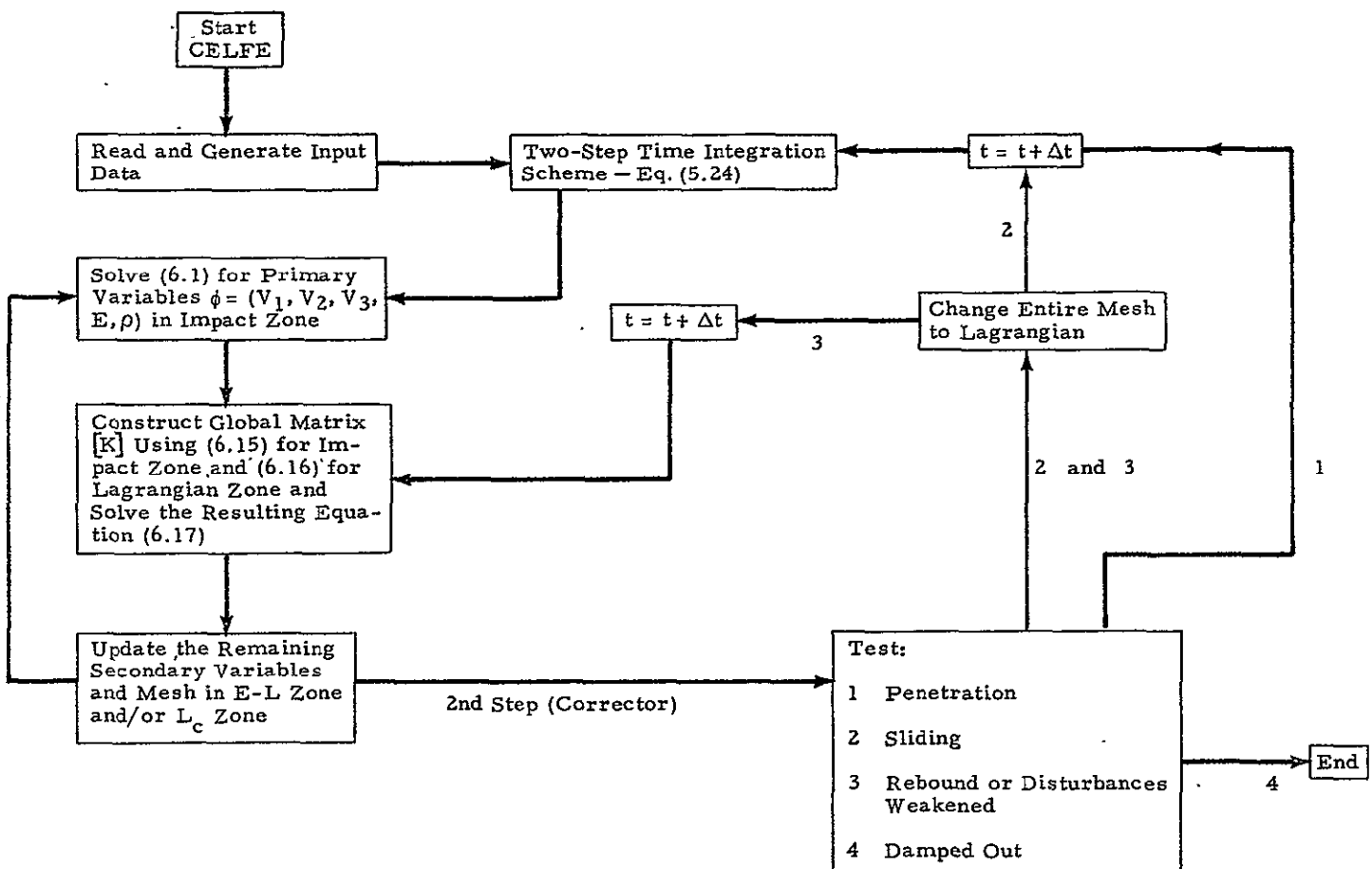


Fig. 6-2 - CELFE Procedure

where $\alpha = 1, 2, \dots, M$, and M is the total number of the primary variables. In this study, $M = 14$ in general, i.e., V_j , $j = 1, 2, 3$; E ; ρ ; and S_{ij} , $i, j = 1, 2, 3$. For orthotropic materials, it reduces to 11, since $S_{ij} = S_{ji}$.

Equation (6.25) can be solved using SOLVE for each α at a time. In order to optimize the time required for the interfacing procedure, the following scheme is used:

- At each time step, compute all $A^{(\alpha)}$ and $B^{(\alpha)}$ one at a time for each element, and for each $\alpha = 1, \dots, M$, sequentially.. For each α , these element matrices are stored subsequently in NASTRAN INPUTT2 matrix format on a disk file.
- Store all relevant data, including the solutions of the previous time step, and those of the secondary variables, etc., into a disk file before calling EXIT from CELFE.
- NASTRAN reads all the data of element matrices $A^{(\alpha)}$ and $B^{(\alpha)}$, and sums the element matrices for each α . Then solve Eq. (6.25) using SOLVE for each.
- The solutions $\phi^{(\alpha)}$, $\alpha = 1, \dots, M$, are written on a disk file using OUTPUT2 matrix format.
- CELFE reads the output disk and makes further computations.

6.5.2 Coupling Eulerian-Lagrangian Modes Using CELFE/NASTRAN

In this portion, the main task is to solve Eq. (6.17) for the entire structure. Recall that Eq. (6.17) is composed of Eq. (6.15) for the elements in the impact zone, and Eq. (6.16) for the elements in the Lagrangian zone. Furthermore, the element matrices K_j , G_j of Eq. (6.15) and p^2M , pB and K of Eq. (6.16) for the L_c zone are generated and/or computed by CELFE. These element matrices are added according to the fixed form (Eq. (6.16)) for the NASTRAN part.

The scheme used in this portion is similar to the previous one with some additional steps to incorporate the CELFE substructure into the NASTRAN substructure as discussed above. The scheme can be stated as follows:

- Compute all K_j , $j = 1, 2, 3$ in Eq. (6.15) each at a time for each element. The element matrices K_j for $j = 1, 2, 3$, are stored

subsequently on $j = 1, 2, 3$, for each element on a disk file in INPUTT2 format.

- Compute all G_j , $j = 1, 2, 3$, and reassemble in a sorted manner for all grids of CELFE substructure. Then write $G = \{G_1, G_2, G_3\}$, together with all other data and parameters, in bulk data format and punch into card images. These card images together with the CELFE grid data are stored in a breakpointed disk file.
- Store all relevant data in a disk file before calling EXIT from CELFE as in Section 6.5.1.
- NASTRAN reads all K_j , $j = 1, 2, 3$ from the disk file and adds the matrices into NASTRAN structural stiffness matrix K in Eq. (6.16) to form the coupled system matrix K_{GG} .
- Add the inertia and damping terms, together with the loading vector composed of those read from the breakpointed disk file for CELFE grids and the remaining, to form Eq. (6.17). Then solve the system and store the results in OUTPUT2 format on a disk file.
- Return to CELFE for further computations as in Section 6.5.1.

6.5.3 Remarks

As mentioned previously, the procedures utilizing SOLVE in NASTRAN as an equation solver for the impact zone, and coupling the CELFE substructure with NASTRAN can be applied separately or simultaneously. The choice depends on the specific problem under consideration. The flow chart depicted in Fig. 6-3 illustrates a combined version of the procedure. The logic for embedding the procedure into the complete CELFE system can be found in Fig. 6-2.

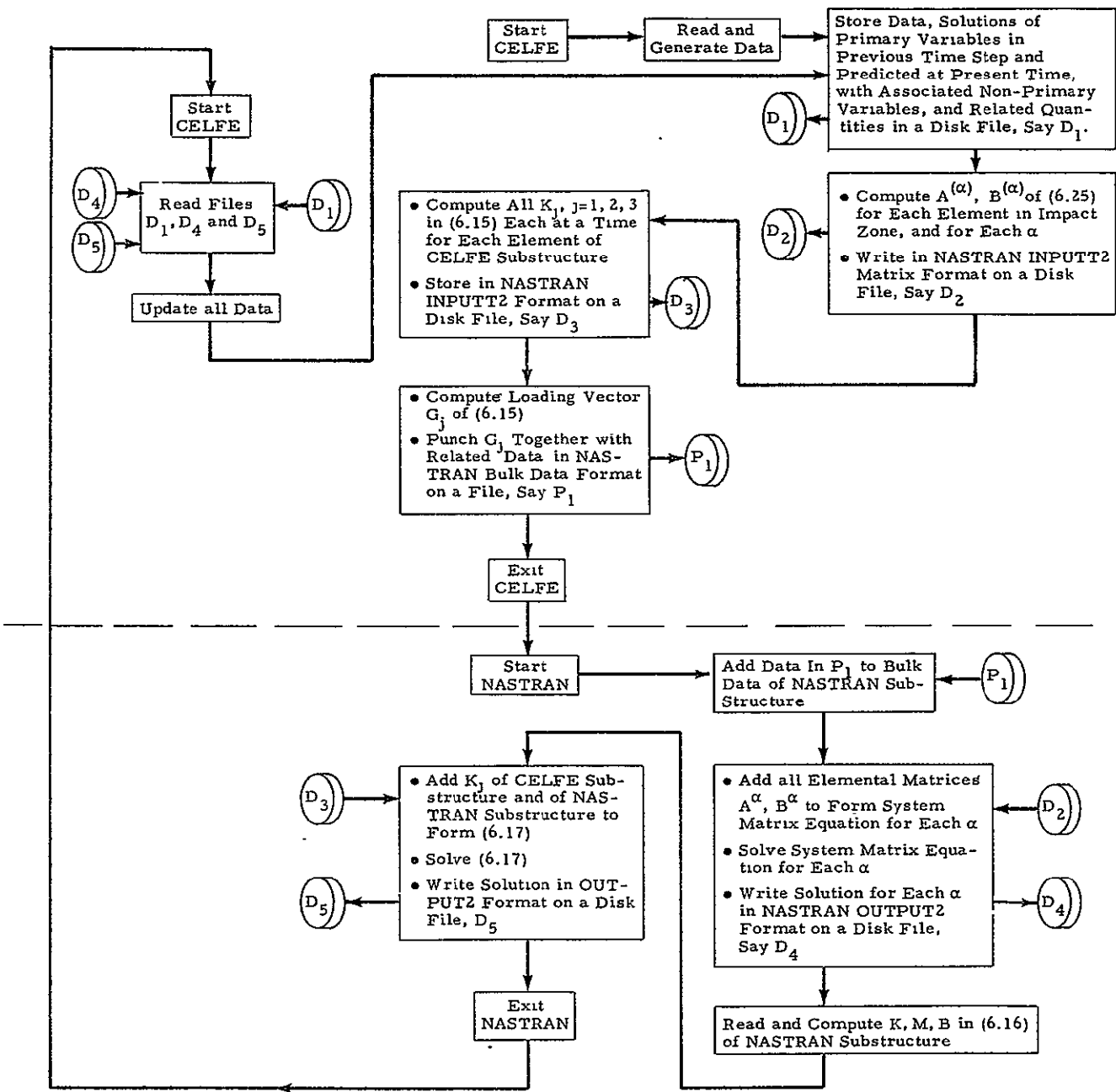


Fig. 6-3 - Interfacing Procedure for CELFE/NASTRAN

7. TEST PROBLEMS AND NUMERICAL RESULTS

In this section, some results obtained from numerical experiments of the developed code are discussed. Various test problems have been used in various stages of developing the CELFE code. The test problems include an inviscid hydrodynamic model, a hydroelasto-viscoplastic model and a complete CELFE model. The numerical experiments are carried out to serve the purpose of developing computer codes stage-by-stage on one hand, and on the other hand, to resolve the difficulties in various aspects encountered in the high velocity impact analysis.

7.1 INVISCID HYDRODYNAMIC MODEL IN EULERIAN MODE

The present problem is used mainly to develop a computer code based on the algorithm formulated in Section 5 for handling the viscoplastic flow in the impact zone.

7.1.1 Description of a Typical Impact Problem

As pointed out in our earlier discussions, a hydrodynamic model is a good approximation in the early stages of the high velocity impact process, during which the pressure is comparable to the shear strengths of the target material. As a starting point we begin with a numerical solution to the hydrodynamic equations with the inviscid adiabatic approximation. In this case the conservation equations, with $\sigma_{ij} = -P\delta_{ij}$, become

$$\begin{aligned}\frac{\partial}{\partial t}(\rho) &= -\frac{\partial}{\partial x_i}(\rho v_i) \\ \frac{\partial}{\partial t}(\rho v_i) &= -\frac{\partial}{\partial x_i}(P) - \frac{\partial}{\partial x_j}(\rho v_i v_j) + \rho f_i \\ \frac{\partial}{\partial t}(\rho e) &= -\frac{\partial}{\partial x_i}(Pv_i) - \frac{\partial}{\partial x_i}(\rho e v_i) + \rho f_i v_i\end{aligned}\quad (7.1)$$

The above equations can be written in the conservation form as

$$\frac{\partial \phi}{\partial t} + \frac{\partial F^k}{\partial x_k} = G \quad (7.2)$$

where

$$\begin{aligned}\phi &= \begin{cases} \rho \\ v_j; j = 1, 2, 3 \\ E \end{cases} \\ F^k &= \begin{cases} v_k \rho \\ v_k v_j + P; j = 1, 2, 3 \\ v_k E + v_k P \end{cases}; k = 1, 2, 3\end{aligned}$$

$$G = \begin{cases} 0 \\ F_j; j = 1, 2, 3 \\ v_\ell F_\ell \end{cases}; \ell = 1, 2, 3 \quad (7.3)$$

where $v_j = \rho v_j$, $j = 1, 2, 3$, $E = \rho e$.

Consider the impact of a cube on a semi-infinite body composed of possibly different materials at a velocity v_0 normal to the target surface. A typical finite element mesh symmetric about the z-axis is shown in Fig. 7-1.

Initial Conditions: We assume that the target is at rest at time $t = 0$. Let S_p denote the set of nodal points in the projectile and S_t denote the set of nodal points in the target. Then $S_0 = S_p \cap S_t$ denotes the set of nodal points common to the target and projectile (i.e., on the interface). For $t = 0$, we have the following initial conditions for density, pressure, and internal energy:

$$\begin{aligned}\rho_i &= \rho_{ot}, \quad i \in S_t \\ \rho_i &= \rho_{op}, \quad i \in S_p \\ p_i &= 0, \quad i \in S_p \cup S_t \\ \epsilon_i &= 0, \quad i \in S_p \cup S_t\end{aligned} \quad (7.4)$$

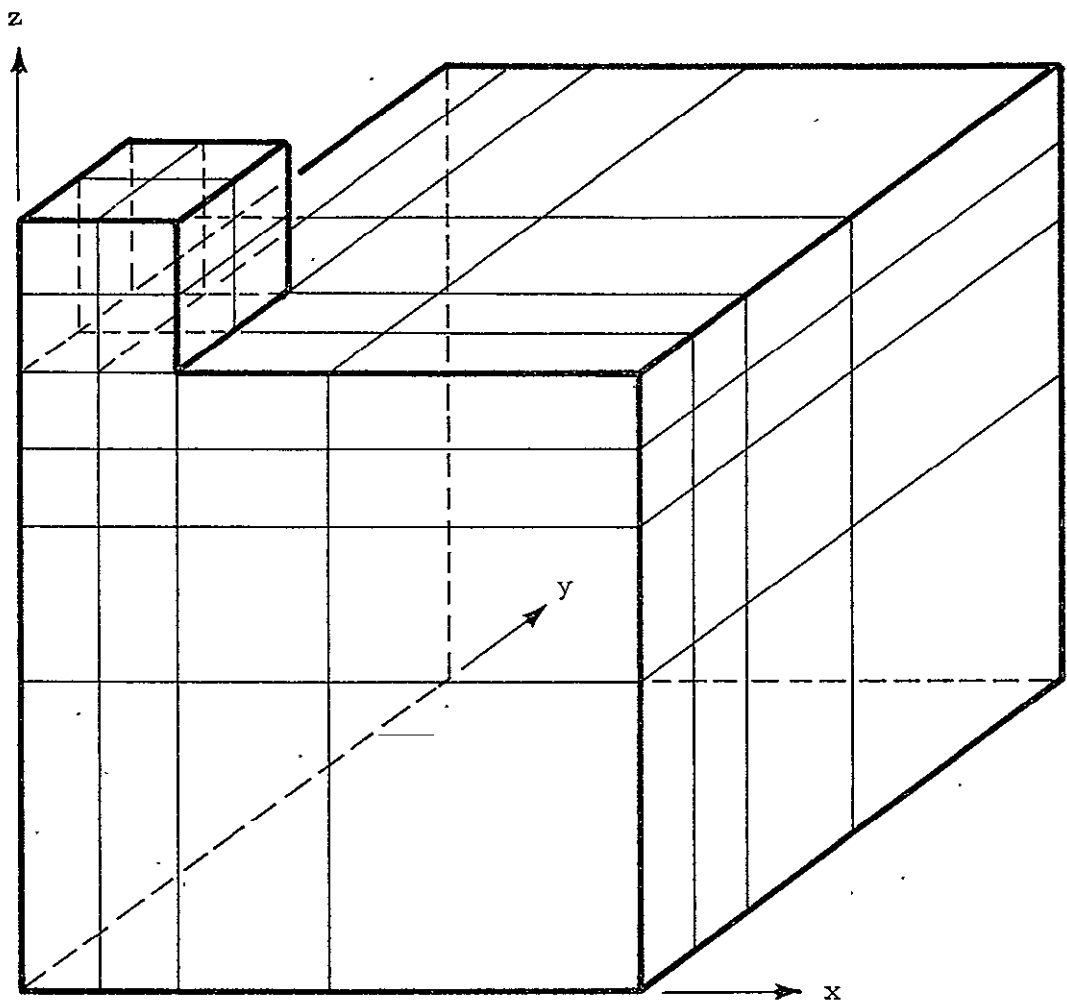


Fig. 7-1 - A Typical Finite Element Mesh of the Projectile-Target Configuration

where the subscript "i" refers to the i^{th} node, ρ_{ot} and ρ_{op} being the initial densities of the target and the projectile, respectively.

Initial conditions on the velocity components u_i , v_i and w_i in x, y, and z-directions, respectively, are

$$\begin{aligned} u_i &= v_i = 0, & i \in S_t \cap S_p \\ w_i &= 0, & i \in S_p \\ w_i &= -v_o, & i \in S_p \end{aligned} \quad (7.5)$$

Boundary Conditions: As mentioned earlier the pressure must be zero on the free surfaces. Since the target is semi-infinite, the material particles far away from the impact region are unaffected. Hence, the internal energy and velocities must be zero and the density must be undisturbed. These boundary conditions, together with conditions for the plane of symmetry, are sketched in Fig. 7-2.

Remark on the Equation of State: As mentioned earlier, there are two forms of equation of state frequently being used in high velocity impact problems. They are the Los Alamos equation of state and Tillotson's equation of state, both obtained from experiment. Obviously, values of computed pressure distribution in materials depend heavily on the particular equation of state being used, which in turn will affect the entire numerical solution. Some uncertainty apparently exists regarding the two equations as they do not appear to agree closely in general and each seems to have its own range of validity. For instance, the Los Alamos equation of state and Tillotson's equation of state differ substantially in the case of aluminum (see Figs. 7-3 and 7-4) for internal energy values below $7.875 \text{ Mpa-in}^3/\text{lbfm}$, and agree closely in the range of 42 to $45.15 \text{ Mpa-in}^3/\text{lbfm}$, as seen in Fig. 7-5. Therefore, caution must be exercised when a specific equation of state is employed in the numerical computations. It seems that a more accurate equation of state is needed.

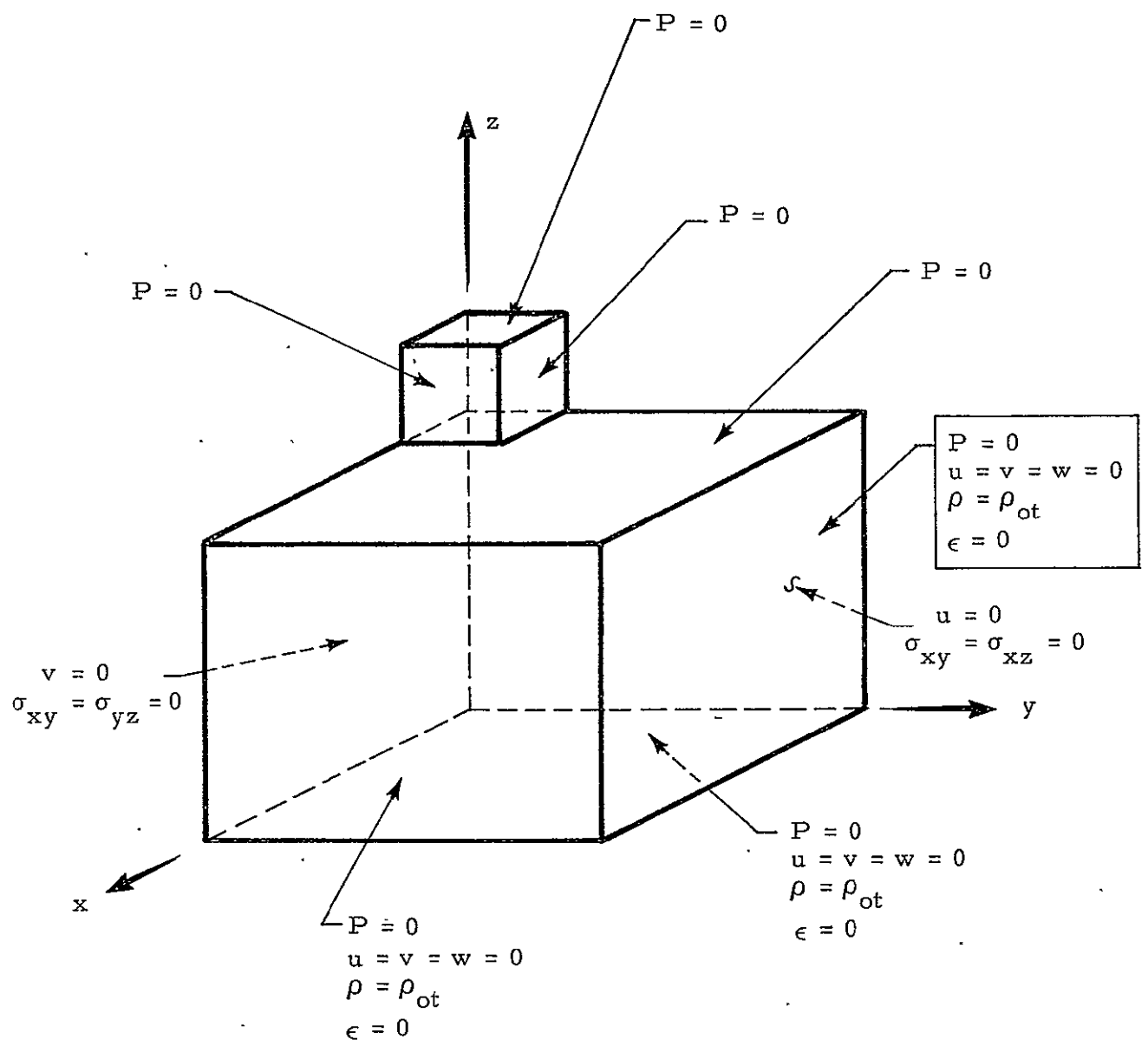


Fig. 7-2 - Boundary Conditions

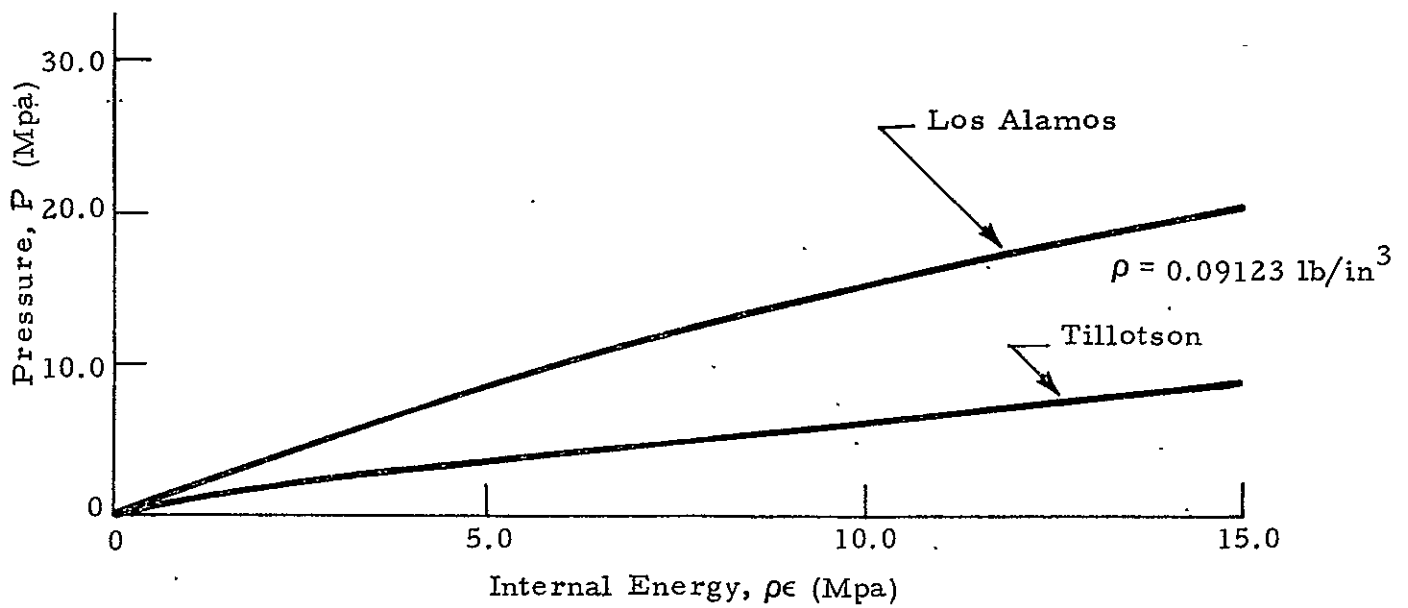


Fig. 7-3 - Variation of Pressure with Internal Energy (Aluminum
 $\rho_0 = 0.0976 \text{ lb/in}^3$, $\rho\epsilon = 0$ to 15.0 Mpa)

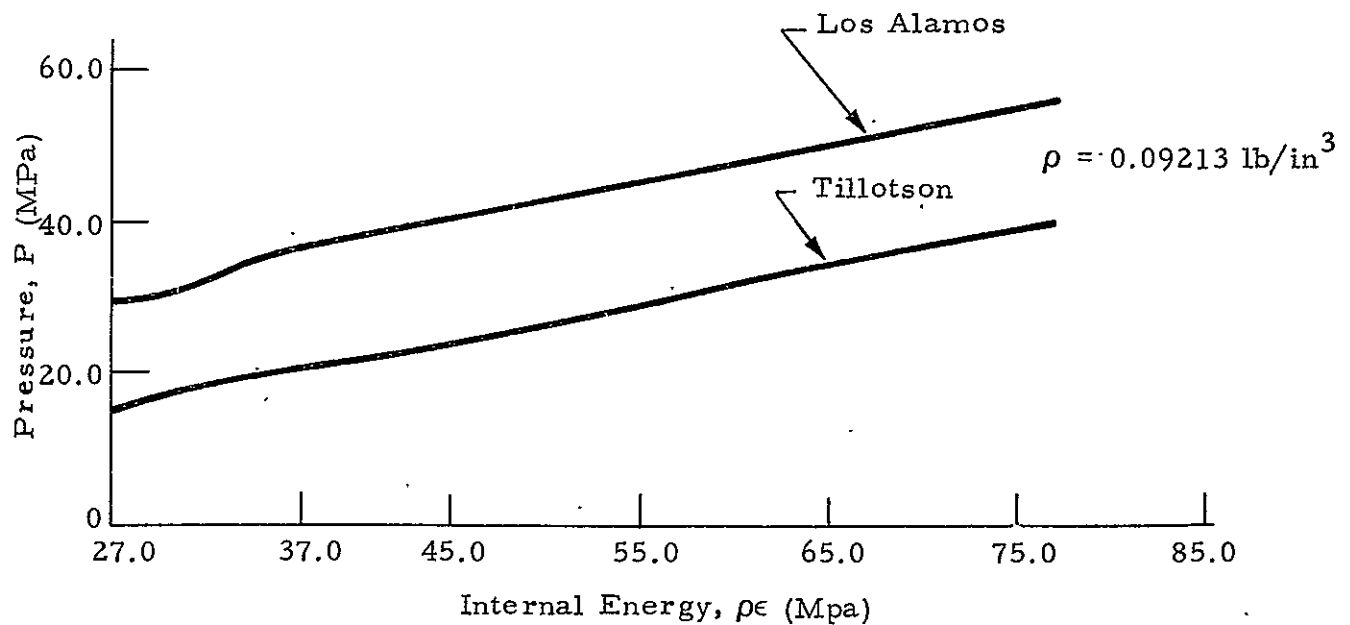


Fig. 7-4 - Variation of Pressure with Internal Energy (Aluminum
 $\rho_0 = 0.0976 \text{ lb/in}^3$, $\rho\epsilon = 27$ to 75 Mpa)

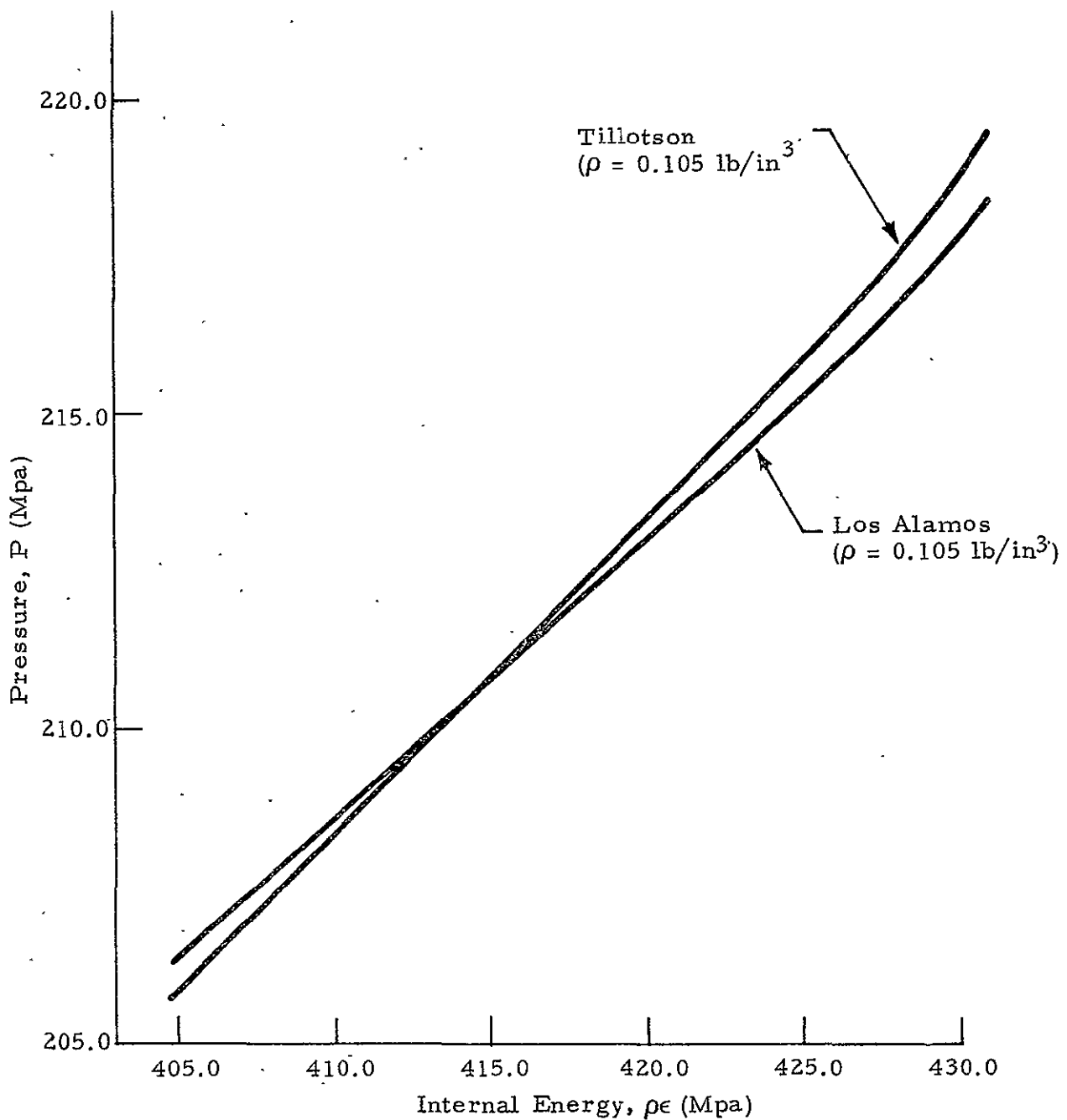


Fig. 7-5 - Variation of Pressure with Internal Energy (Aluminum, $\rho_0 \approx 0.0976 \text{ lb/in}^3$, $\rho\epsilon = 405$ to 430 Mpa)

7.1.2 One-Dimensional Impact Problem

A one-dimensional impact problem is used herein to test the validity of the formulations presented in Section 5. The problem under consideration is that an infinite plate traveling at a specified speed, v_0 , hits normally on another infinite plate at rest, as depicted in Fig. 7-6a. The two plates are 11.8 in thick, and composed of the same aluminum material with initial density $\rho_0 = 0.10 \text{ lb/in}^3$. The impact velocity is chosen to be $v_0 = 262.5 \text{ ft/sec}$ for which a solution in elastic range of impact is available for comparison (Ref. 10).

The problem was solved by the three-dimensional models described in Section 5. The mesh and nodal numbering are generated by subroutine MESH and depicted in Fig. 7-6b. The Rankine-Hugoniot pressure, P_s , is readily obtained using the Los Alamos equation of state (cf. Appendix),

$$P_s = 5.99868 \times 10^{-2} \text{ Mpa} \quad (7.6)$$

The following numerical computations are performed based on inviscid assumption together with the Los Alamos equation of state.

As was discussed in detail in Ref. 37, it is found from the numerical solution of Eq. (7.2) that the method of weighted residuals does not perform satisfactorily. The pressure development in the material computed by these schemes tends to grow indefinitely. This phenomenon becomes more severe when the impact velocity is increased. Spurious oscillations with fairly large amplitudes always gather near the wave front, and the peak pressure is seen to exceed the Hugoniot pressure by about 50% to 100% as the velocity, v , increases from 262.5 to 24610.0 ft/sec. Figure 7-7 shows the time history of pressure at interface computed by the method of least squares. The results computed by a modified Galerkin approach using mid-point Runge-Kutta scheme are found to be almost identical to those shown in Fig. 7-7. It is seen that the pressure at the interface tends to diverge as time increases. The numerical instabilities can also be detected by the spurious oscillations near the shock fronts as shown in Fig. 7-8.

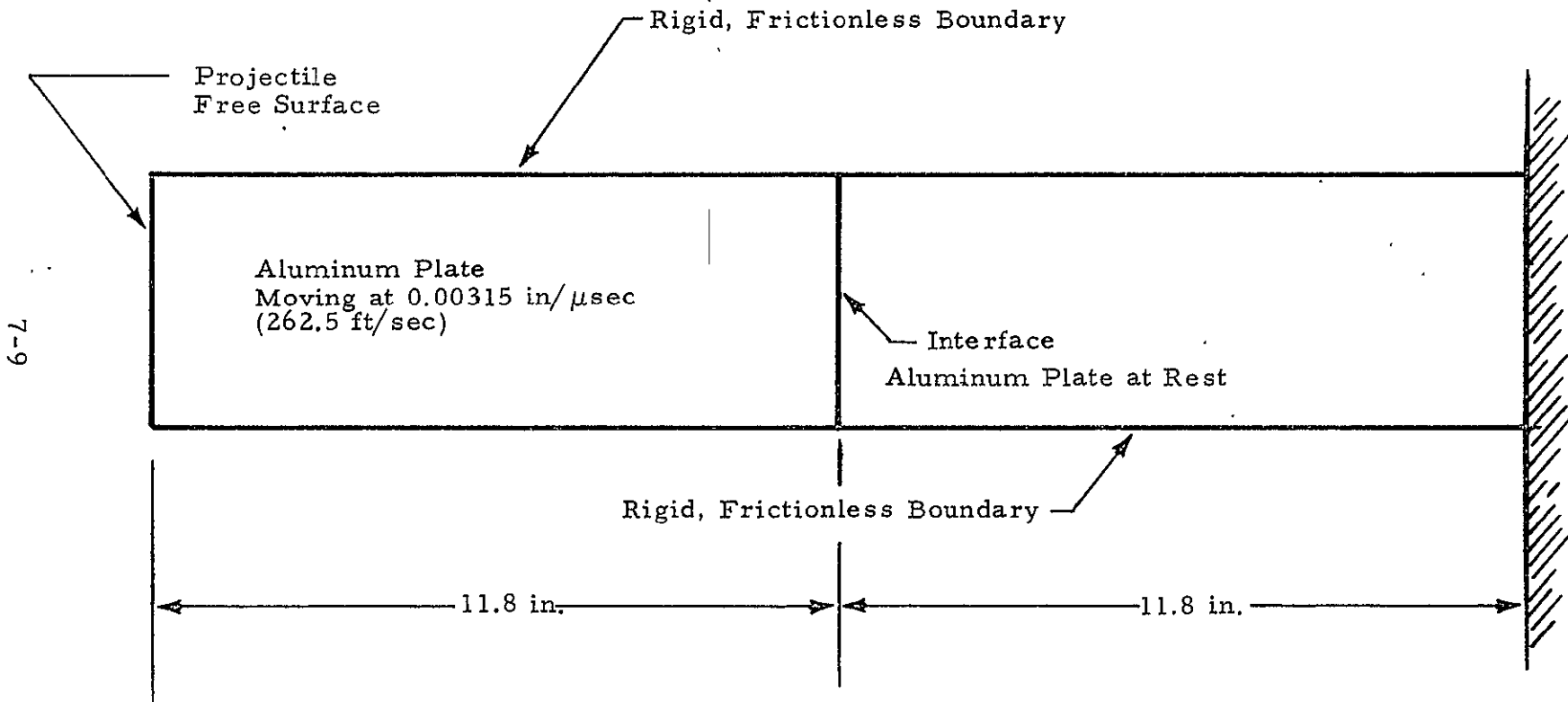


Fig. 7-6 - One-Dimensional Impact Problem
a. Configuration of Plates at Time
of Impact

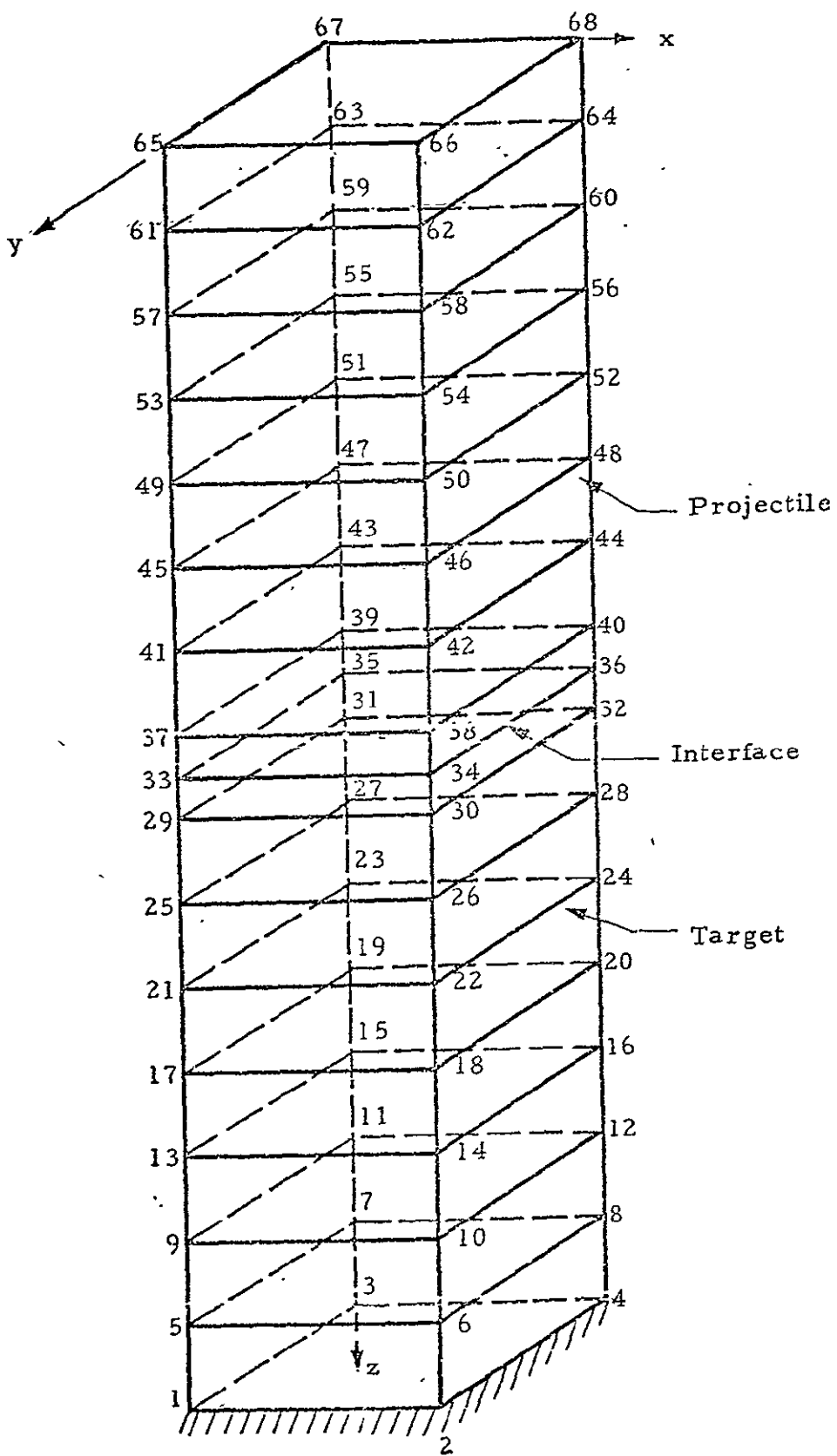


Fig. 7-6 (Concluded)
 b. Numbering of Nodes in the Finite Element (16 Linear Elements)

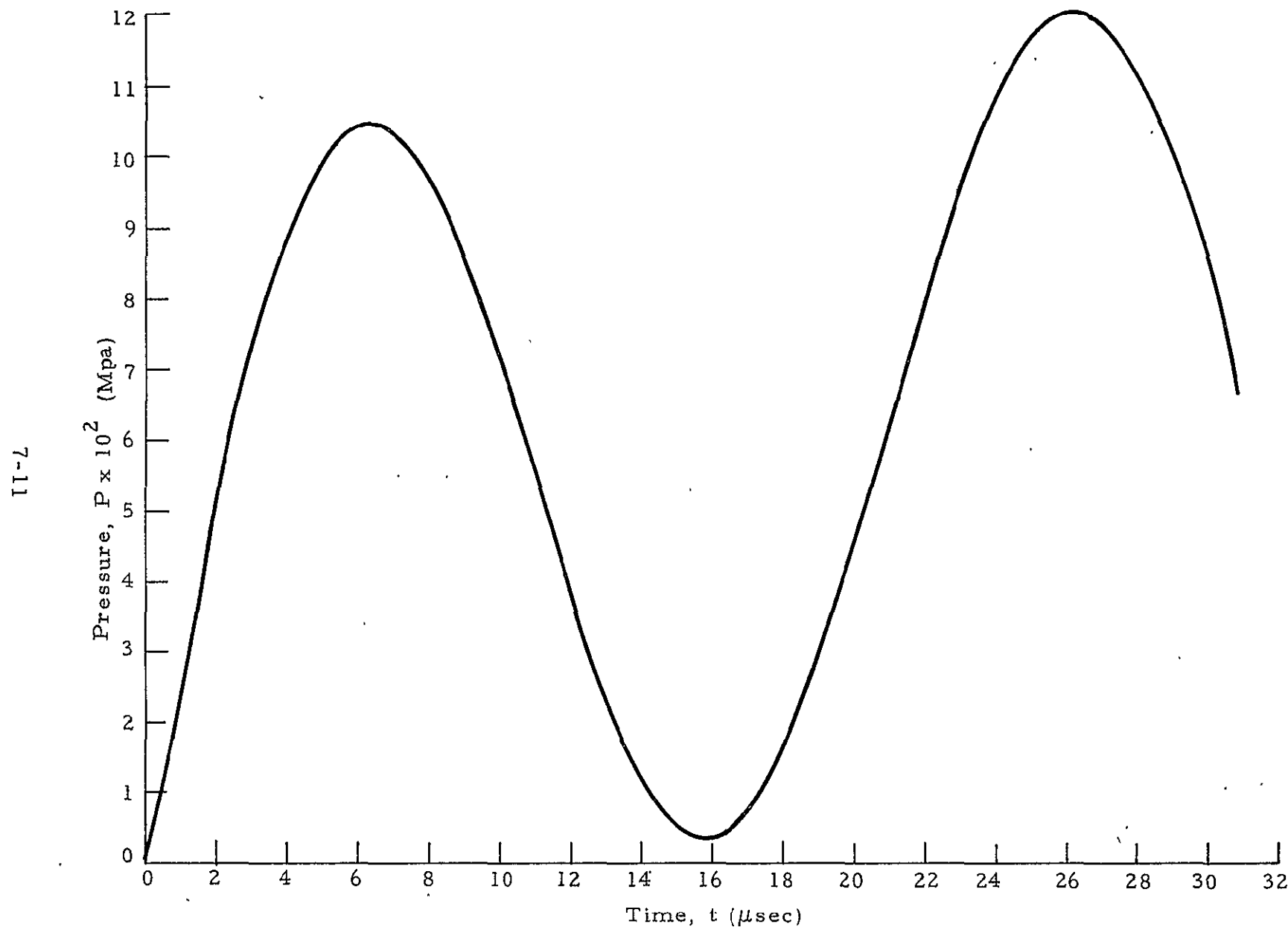


Fig. 7-7 - Time History of Pressure at Interface for 1-D Impact Problem Using Least Squares Scheme with 16 Linear Elements ($v_o = 0.00315$ in/ μ sec, $\rho_o = 0.10$ lb/in³)

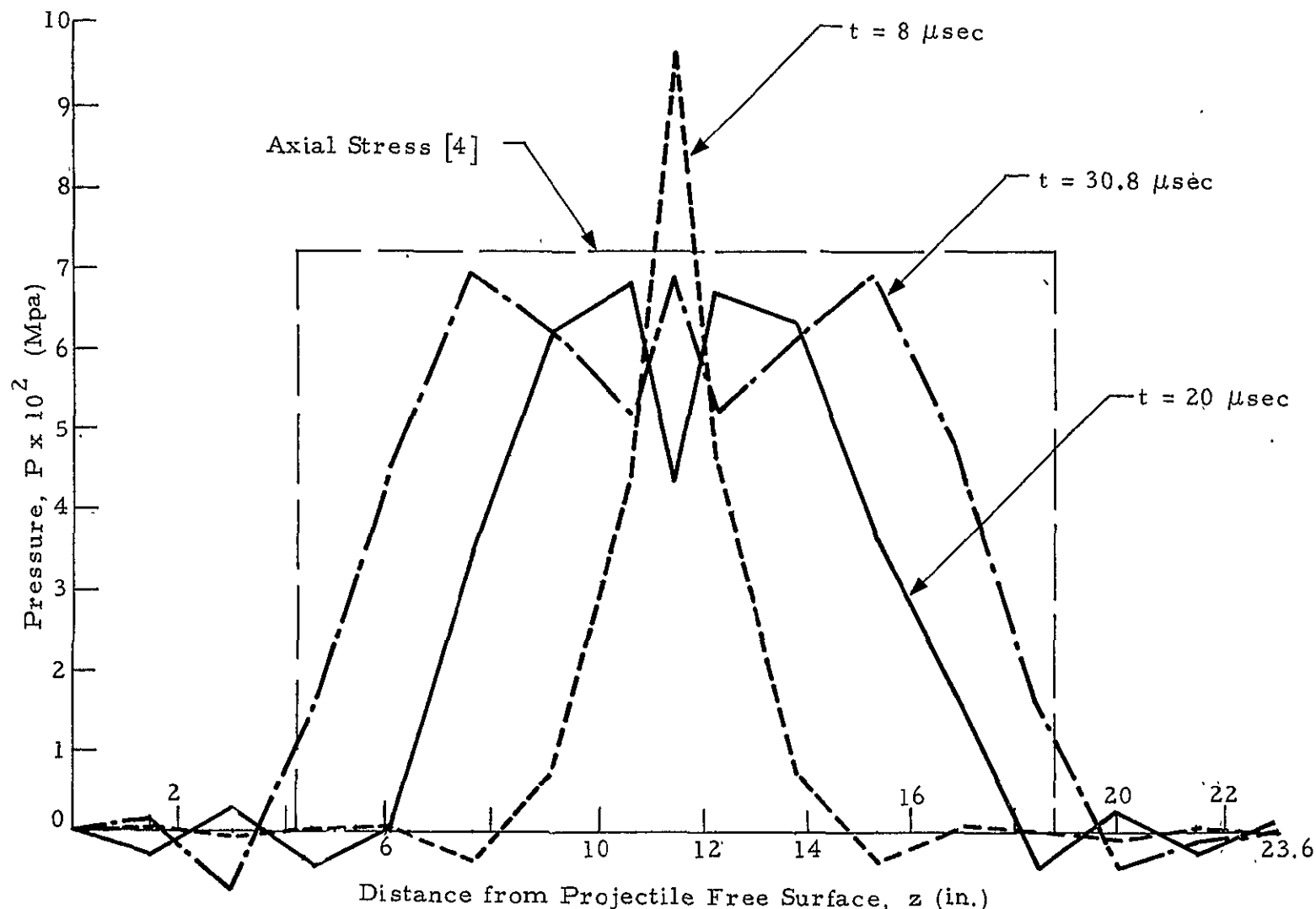


Fig. 7-8 - Pressure Distributions at Various Times for 1-D Impact Problem Using Least Squares Scheme with 16 Linear Elements ($v_o = 0.00315 \text{ in}/\mu\text{sec}$, $\rho_o = 0.10 \text{ lb/in}^3$)

Solution Computed by Weak Solution Formulation: The pressure history at the interface computed using Eq. (5.15) and Eq. (5.16) with $a = 1/2$ is depicted in Fig. 7-9, and the corresponding pressure distributions at various times are shown in Fig. 7-10. It is seen that the results are improving compared to the ones computed by the method of weighted residuals as depicted in Figs. 7-7 and 7-8. The solution may be improved even further when the parameter a in Eq. (5.15) is increased. Figures 7-11 and 7-12 show the pressure history at the interface using $a = 2$ and 4, respectively. The corresponding pressure distributions are plotted in Figs. 7-13 and 7-14.

All results discussed so far and depicted in Figs. 7-7 through 7-14 are computed using 16 linear elements. As shown in Figs. 7-10, 7-13 and 7-14, the overshoot due to the numerical instability decreases rapidly, and the zig-zag behavior near the wave front becomes less severe as the parameter a increases. These facts indicate that the numerical dissipation introduced in the scheme is proportional to the parameter a .

The plots also show some substantial differences in amplitudes of the pressure waves among different a and α values. In addition, as shown in Figs. 7-11 and 7-12, the numerical dissipation increases as α decreases, and the phase lag becomes more apparent at the same time. These imply that various errors may enter in the computations if the scheme is over-dissipated. The sensitivity of the solutions to the factor α , however, can be removed by refining the mesh as shown in Figs. 7-15 through 7-18 where 30 even spaced linear elements were used in computations. In this case, the same time step size as employed in the 16-element case was used. This verifies the statement mentioned in Section 5.3, namely, the factor α is indeed related directly to the ratio of the time step size and the element size. As the mesh size is reduced, the effect of α on the accuracy of the solution becomes less important. The results using 16 quadratic elements also show the same trend. In Figs. 7-19 and 7-20, the pressure history at the interface is depicted using $a = 2.0$ and $a = 4.0$, respectively, with different α . As expected, these results are improved compared to the cases with 16 linear elements, but are less smooth when compared with that using 30 linear elements. Similar comparisons can

7-14

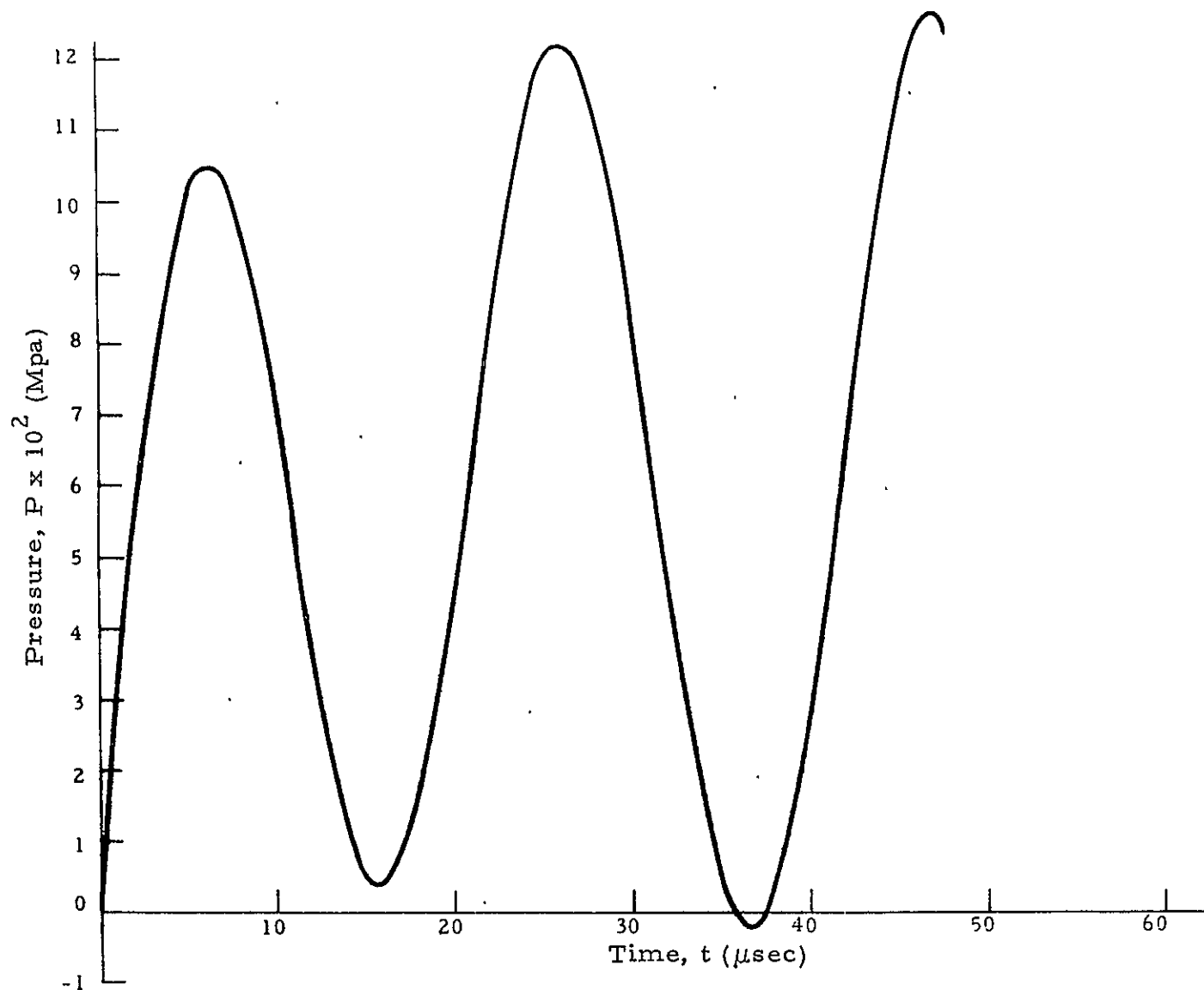


Fig. 7-9 - Pressure Development at the Intensity Interface with 16 Linear Elements ($a = 0.5$, $\alpha = 0.0$)

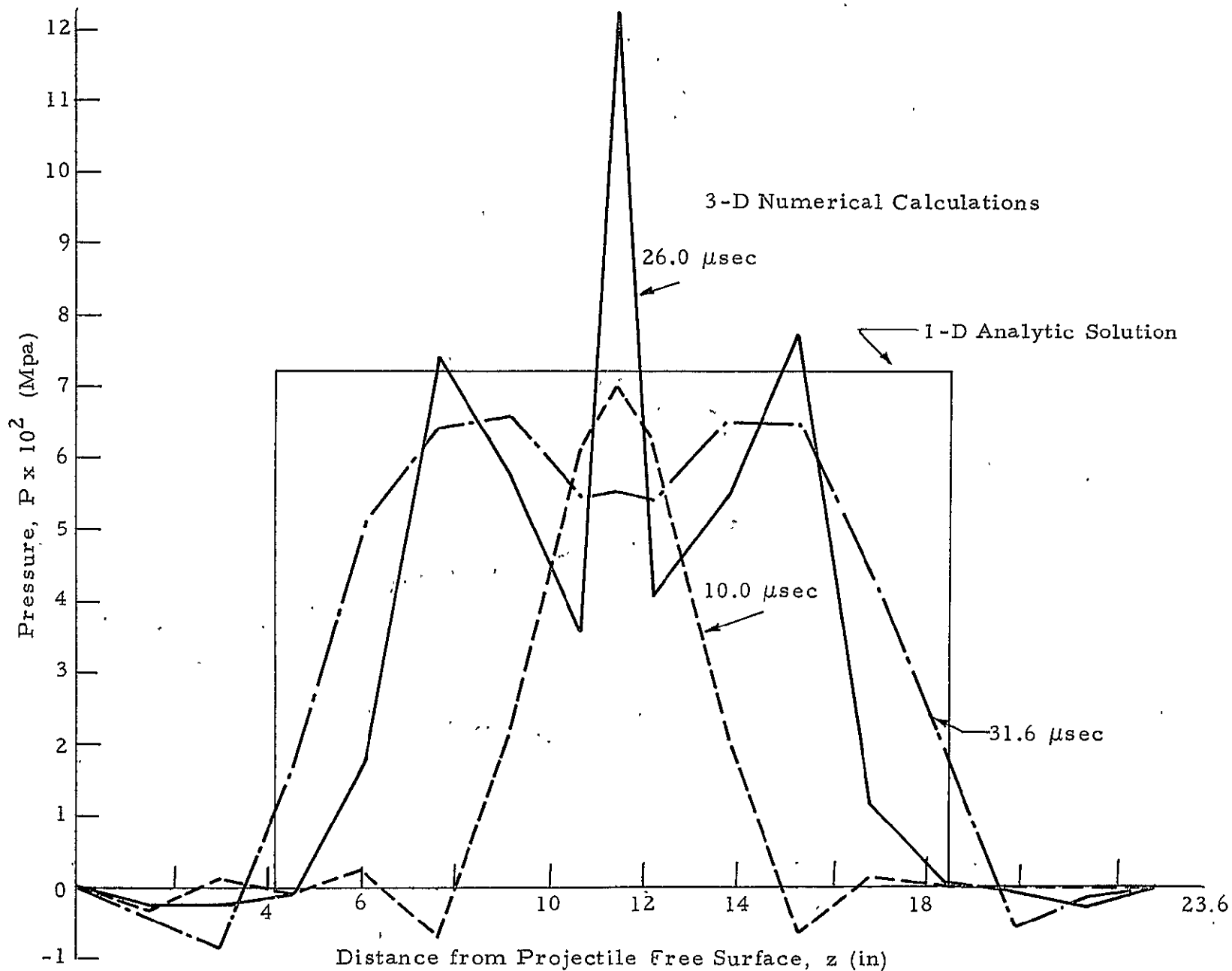


Fig. 7-10 - Pressure Distributions at Various Times
with 16 Linear Elements ($a = 0.5$, $\alpha = 0.0$)

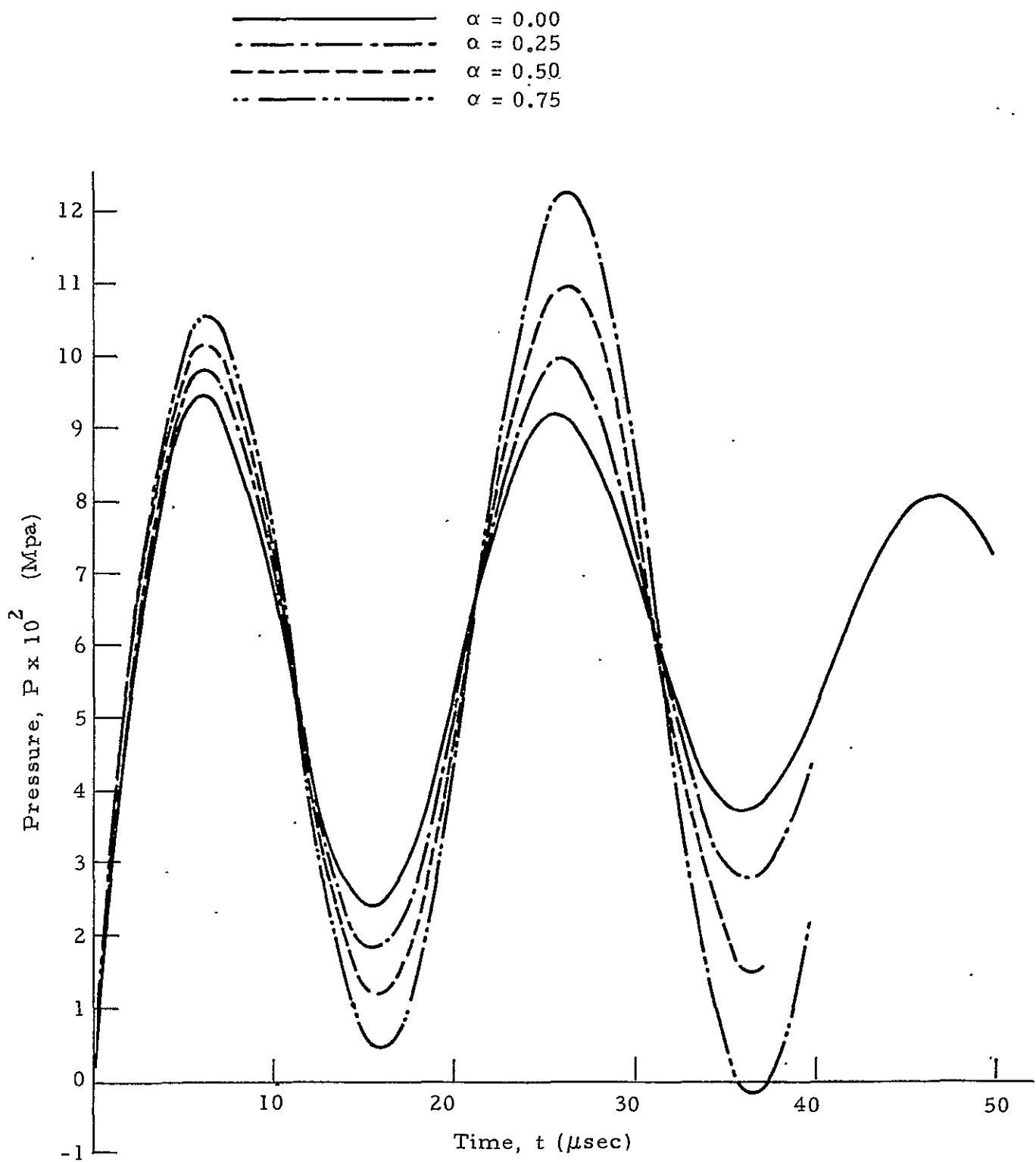


Fig. 7-11 - Pressure Development at the Interface
with 16 Linear Elements ($a = 2.0$)

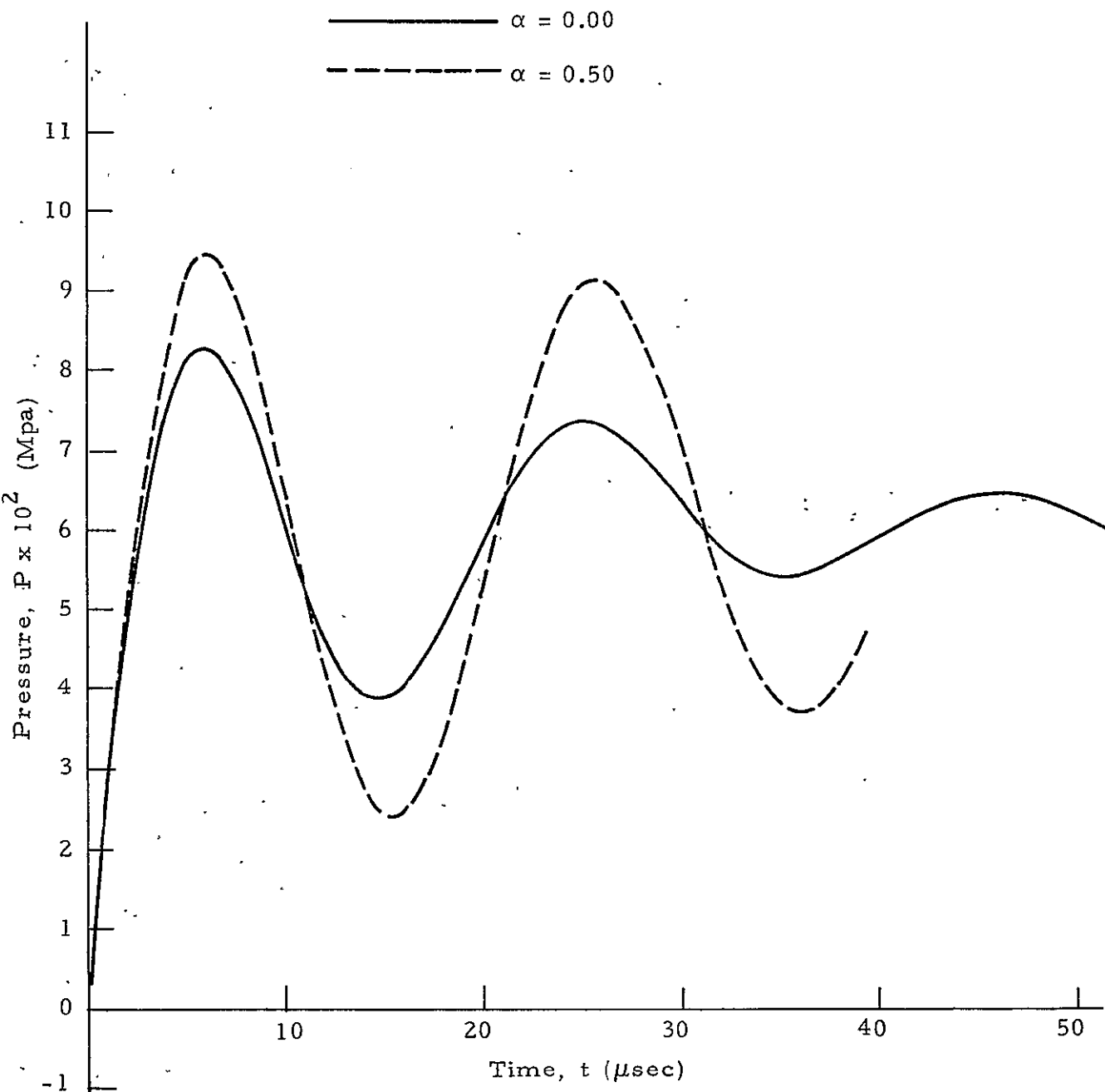


Fig. 7-12 - Pressure Development at the Interface
with 16 Linear Elements ($a = 4.0$)

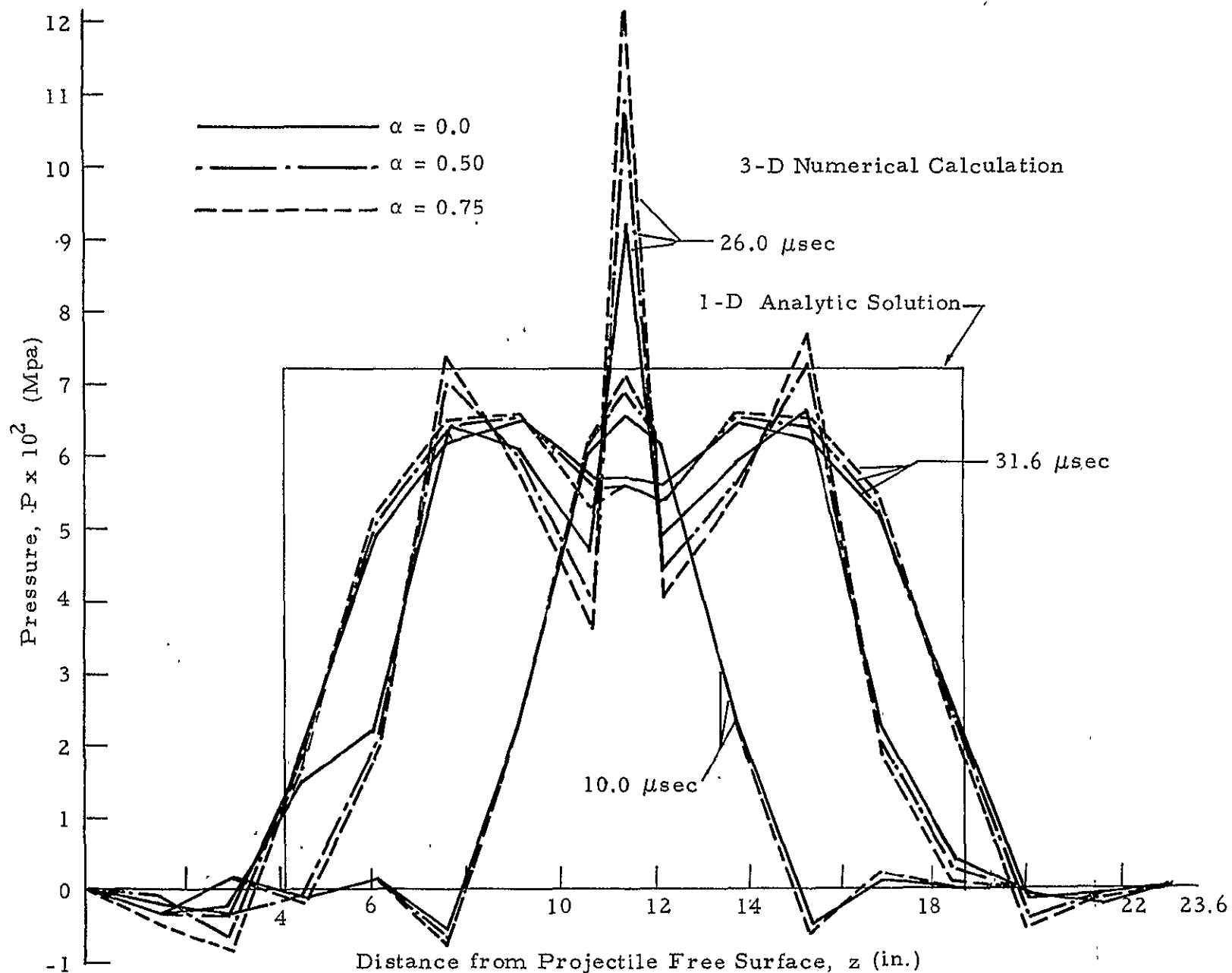


Fig. 7-13 - Pressure Distributions at Various Times
with 16 Linear Elements ($a = 2.0$)

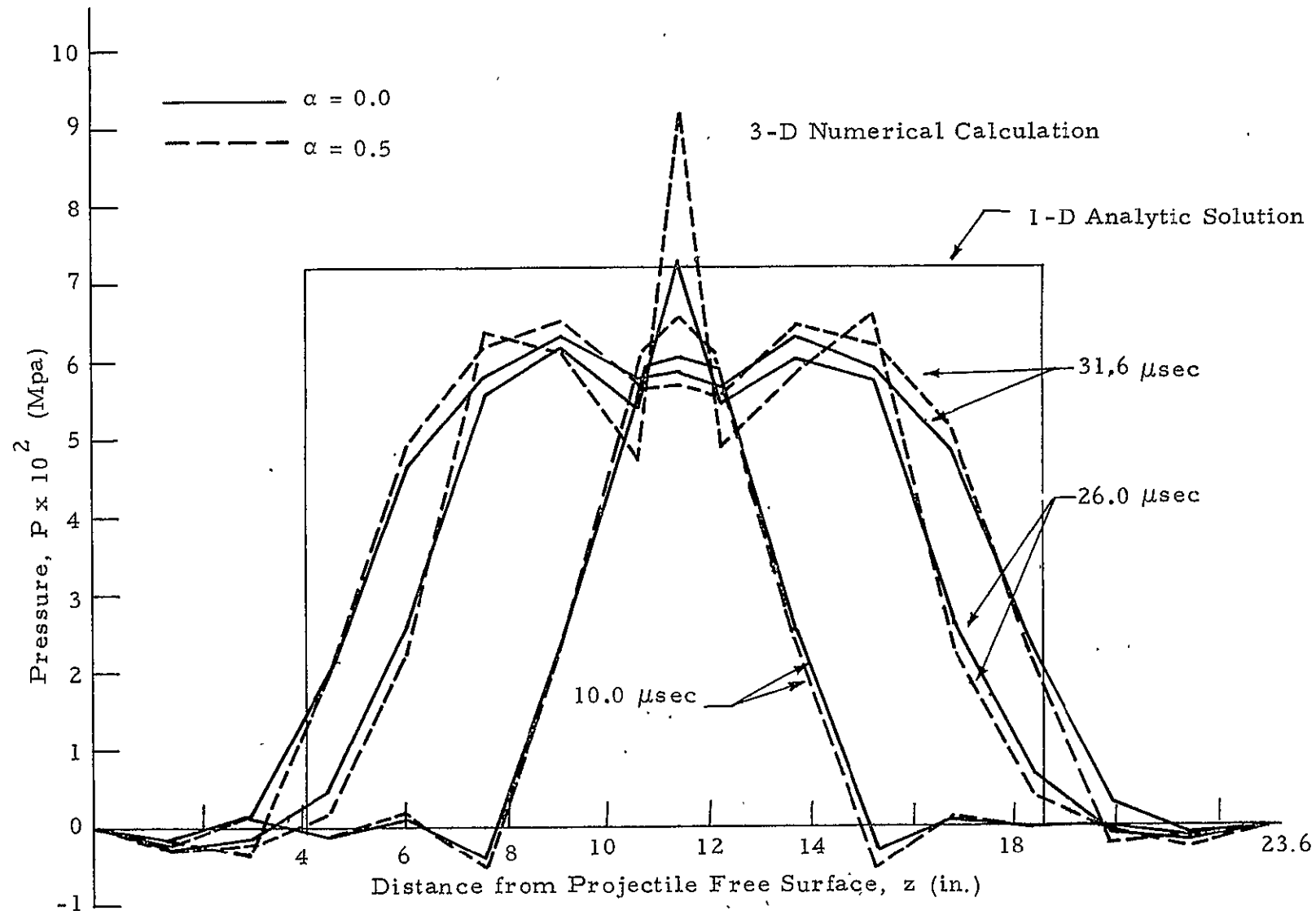


Fig. 7-14 - Pressure Distributions at Various Times
with 16 Linear Elements ($a = 4.0$)

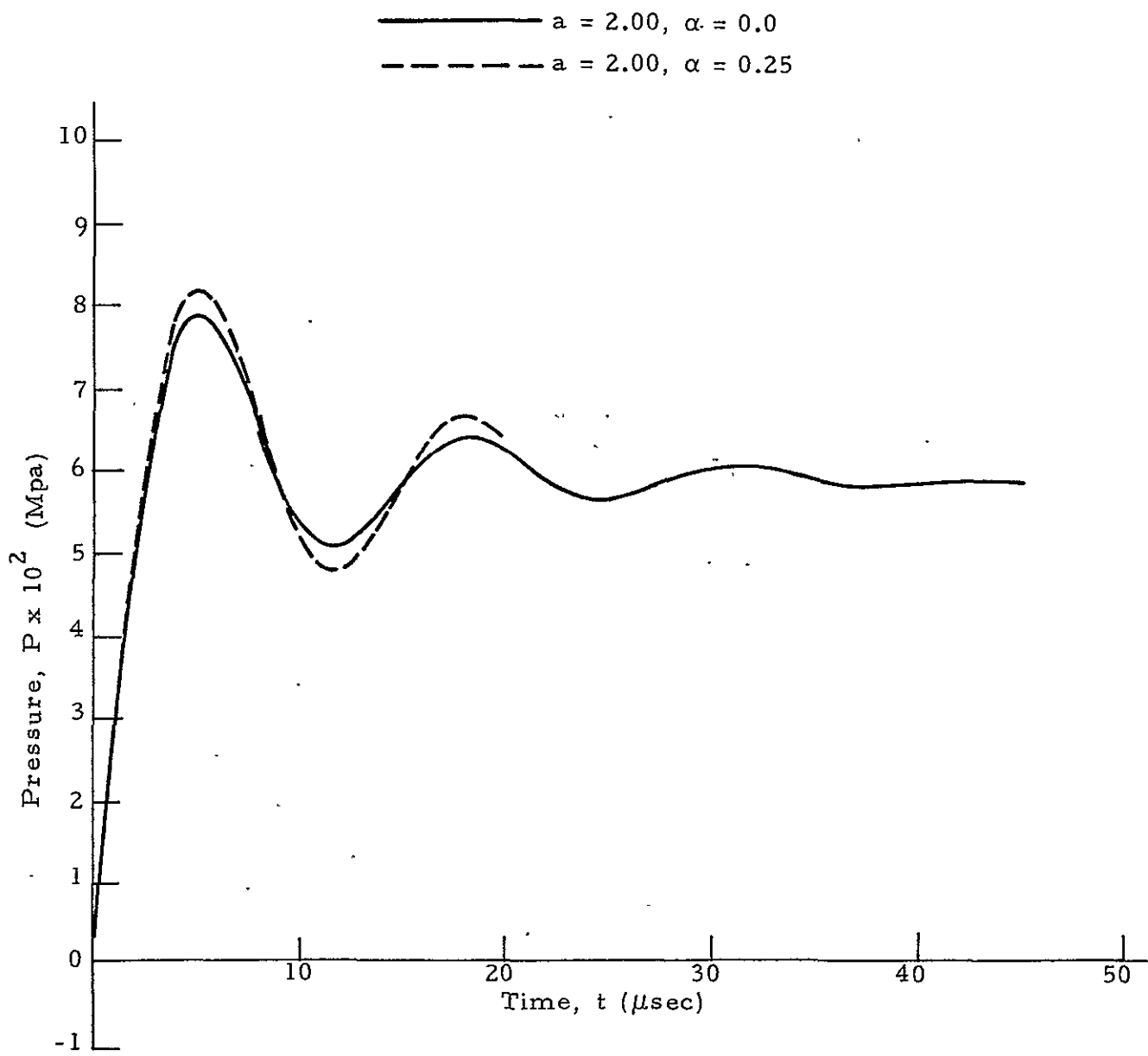


Fig. 7-15 - Pressure Development at the Interface Using 30 Linear Elements
 $(a = 2.0, \alpha = 0.0 \text{ and } 0.25)$

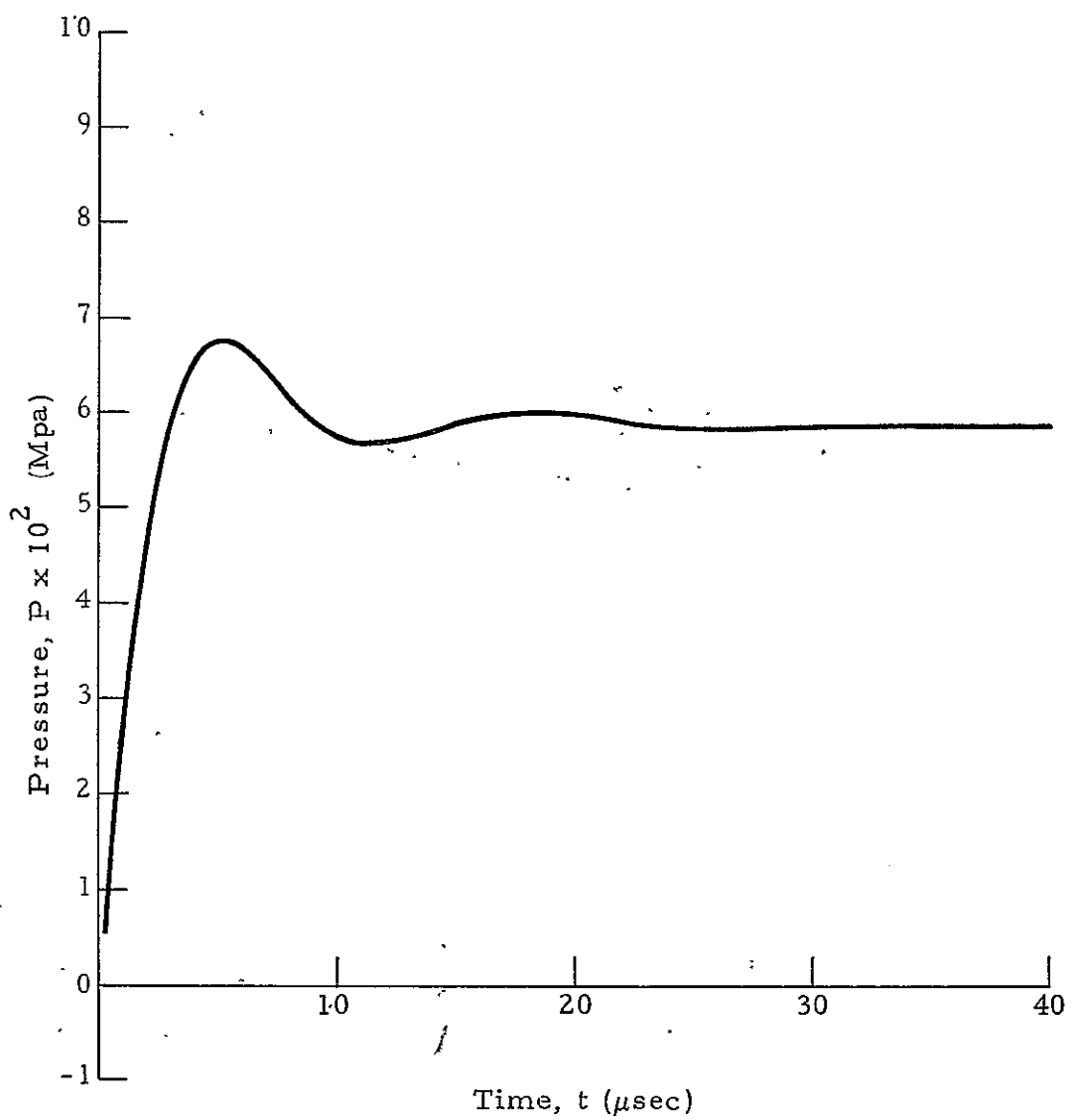


Fig. 7-16 — Pressure Development at the Interface Using
30 Linear Elements ($a = 4.0$, $\alpha = 0.0$)

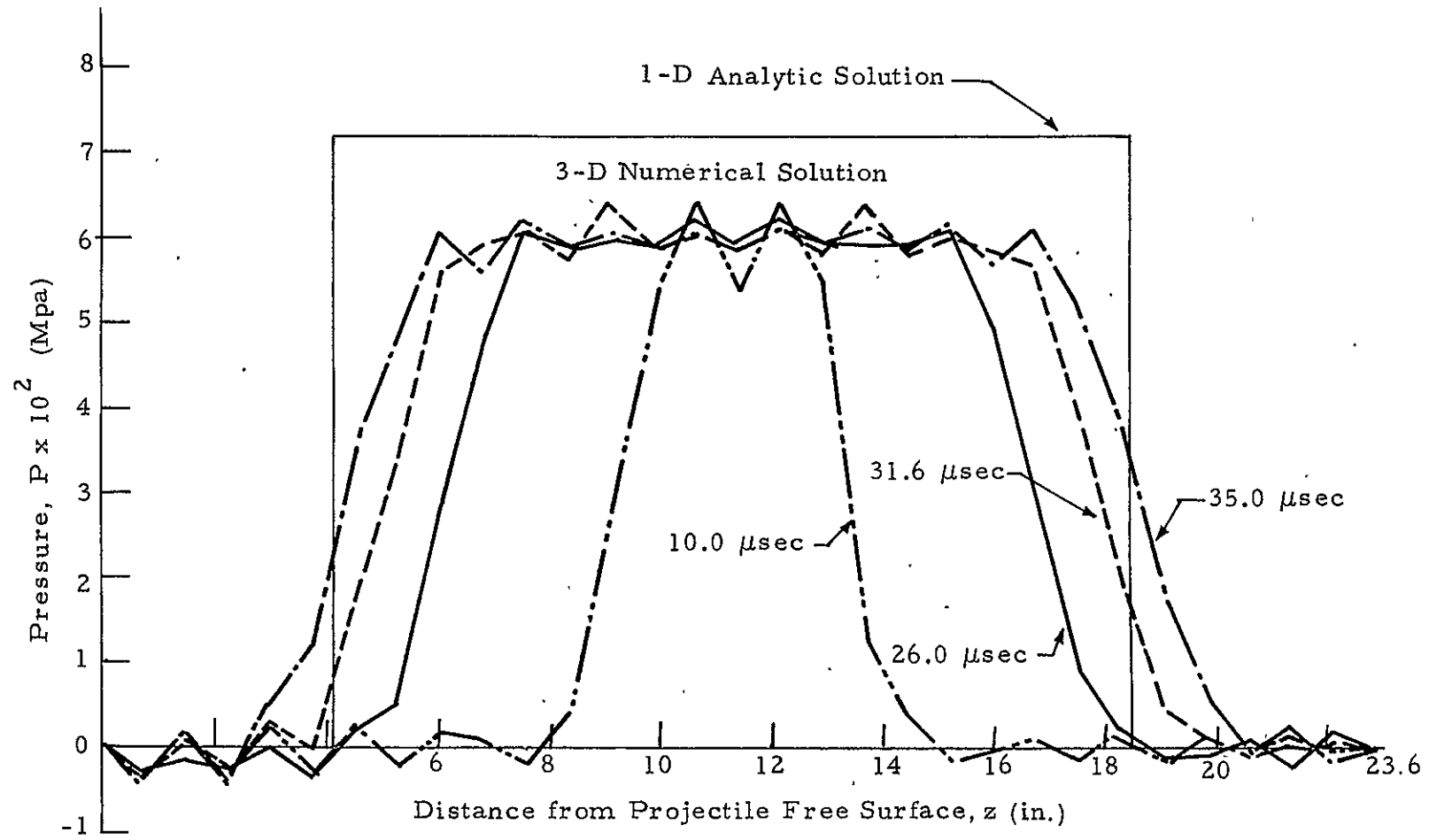


Fig. 7-17 - Pressure Distributions at Various Times Using 30 Linear Elements ($a = 2.0$, $\alpha = 0.0$)

7-23

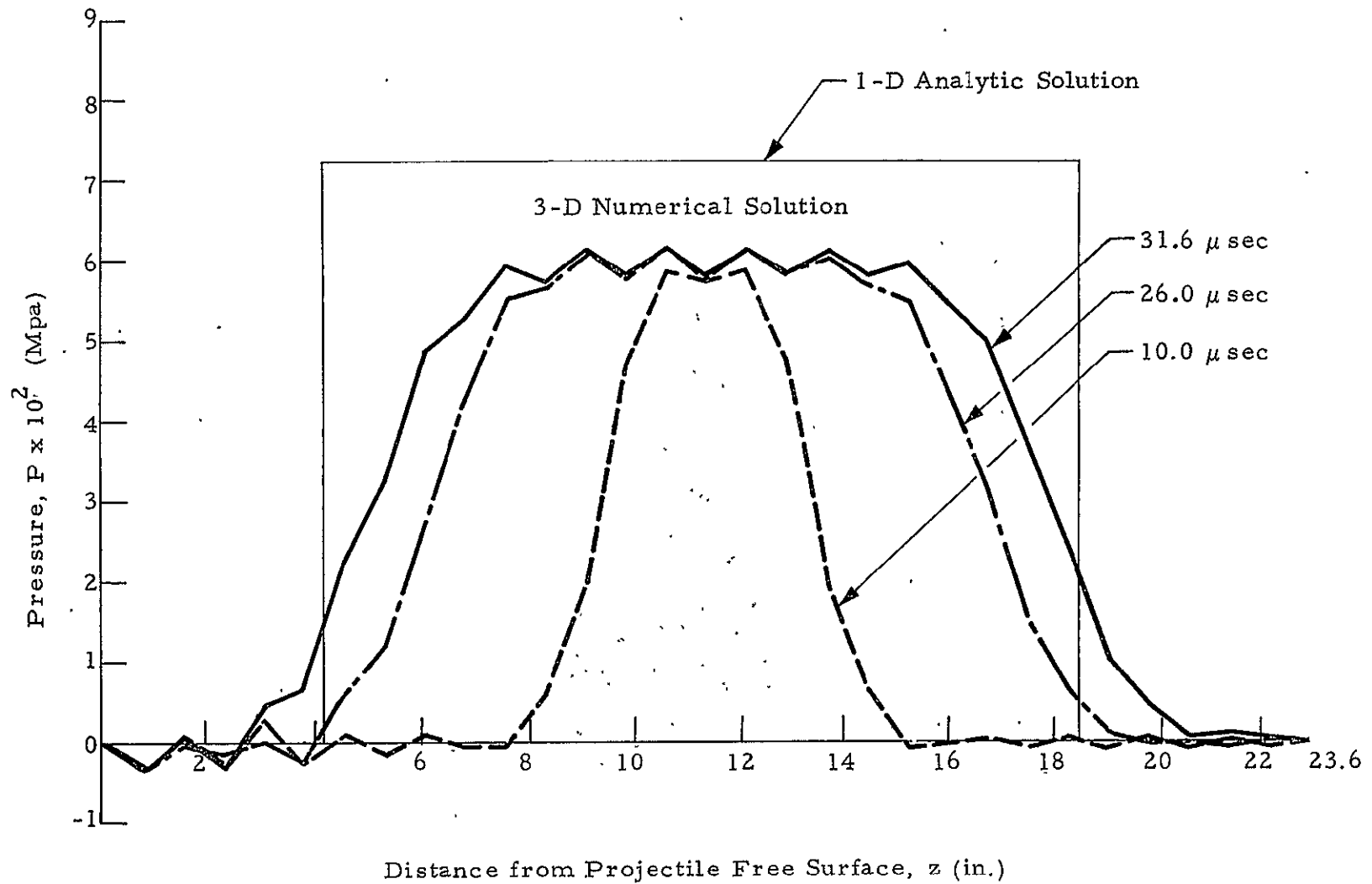


Fig. 7-18 — Pressure Distributions at Various Times Using 30 Linear Elements ($a = 4.0$, $\alpha = 0.0$)

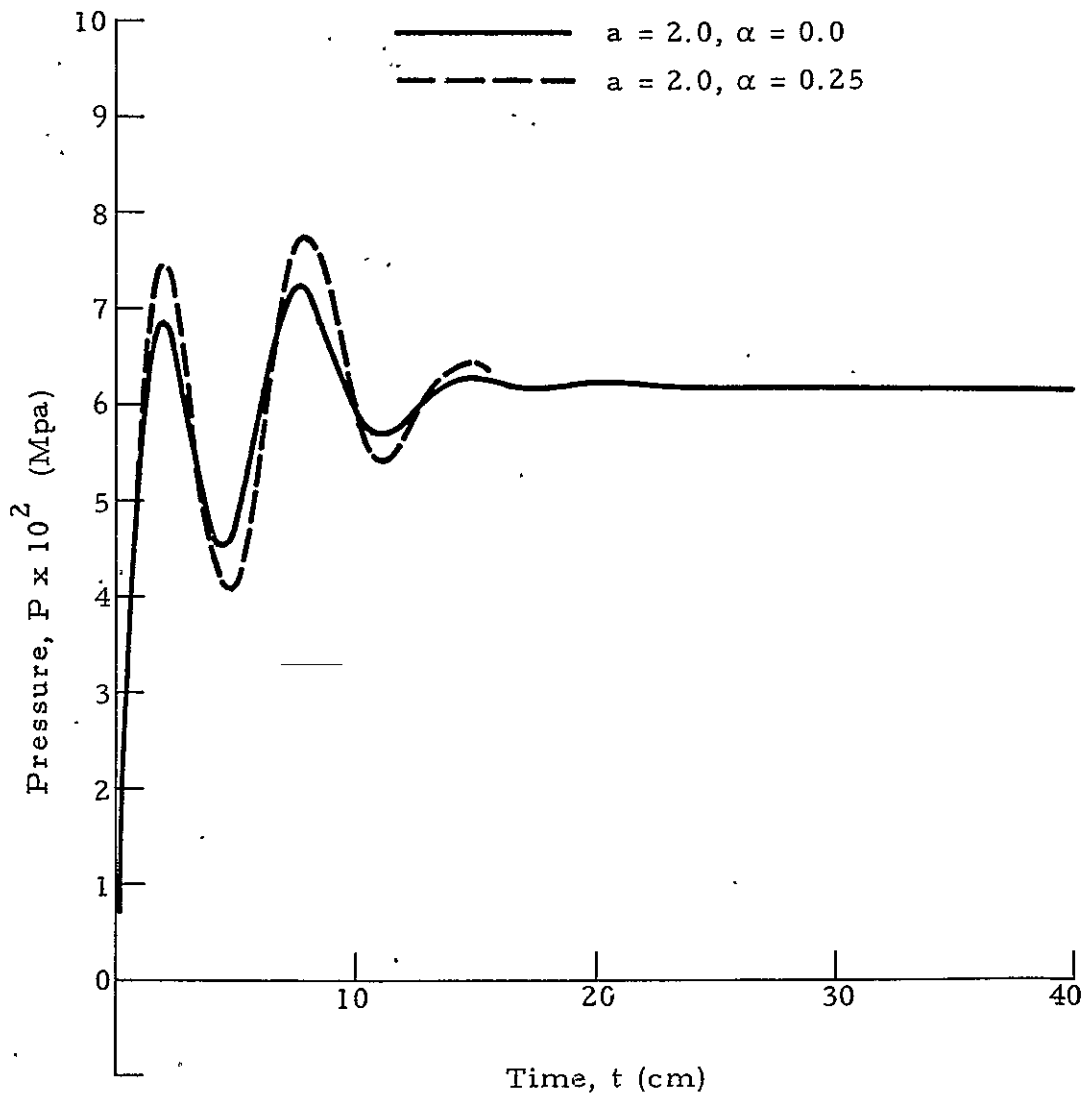


Fig. 7-19 — Pressure Development at the Interface
Using 16 Quadratic Elements
($a = 2.0, \alpha = 0.0$ and 0.25)

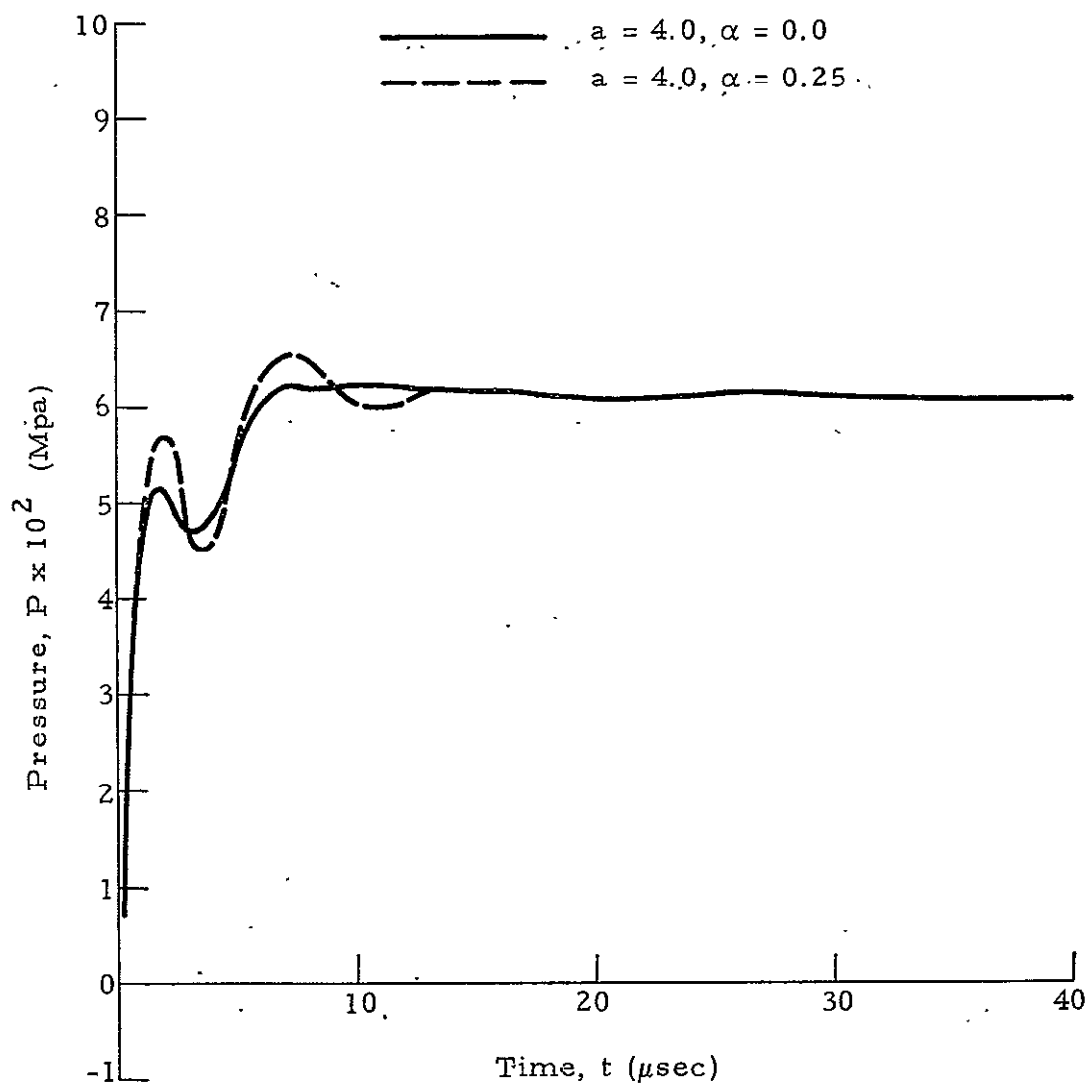


Fig. 7-20 — Pressure Development at the Interface
Using 16 Quadratic Elements
($a = 4.0, \alpha = 0.0$ and 0.25)

also be made for the pressure distributions (see, e.g., Figs. 7-13 and 7-14 for 16 linear elements, Figs. 7-17 and 7-18 for 30 linear elements, and Figs. 7-21 and 7-22 for 16 quadratic elements).

As is seen, all the cases seem to underpredict the peak pressure compared to the analytic solution. However, with the same given conditions and Los Alamos equation of state, the pressure computed by Rankine-Hugoniot relations is $P_s = 5.99868 \times 10^{-2}$ Mpa. This value is approximately equal to the average value as shown in Figs. 7-17 and 7-18 which indicates that our numerical results are quite reasonable. Accordingly, P_s should be the upper bound for the average pressure distribution in the material under high velocity impact, since the physical as well as numerical dissipative effects may actually reduce the pressure buildup in the material.

The speed of sound in a material can be obtained by the relation

$$C_s^2 = \left(\frac{\partial P}{\partial \rho} \right)_s \quad (7.7)$$

Following the Gibb's equation, one has

$$C_s^2 = \frac{P}{\rho^2} \frac{\partial P}{\partial \epsilon} + \frac{\partial P}{\partial \rho} \quad (7.8)$$

where ϵ is the specific internal energy which is now being considered as a function of total specific energy and the particle velocity. Thus the propagation speed of the pressure waves can be computed by substituting the nodal solution of the conservation equations and equation of state on the element containing the wave front into Eq. (7.8). The numerical values of C_s in the target obtained using Los Alamos equation of state at some typical times are shown in Table 7-1. It is seen that the values oscillate around the shock speed computed by Rankine-Hugoniot relation, i.e., $C_{sR-H} = 17575.1$ ft/sec. In elasto-dynamic theory, on the other hand, the sound speed is represented by

$$C_{sE\ell} = \sqrt{\frac{(1-\nu)E}{(1+\nu)(1-2\nu)\rho}} \quad (7.9)$$

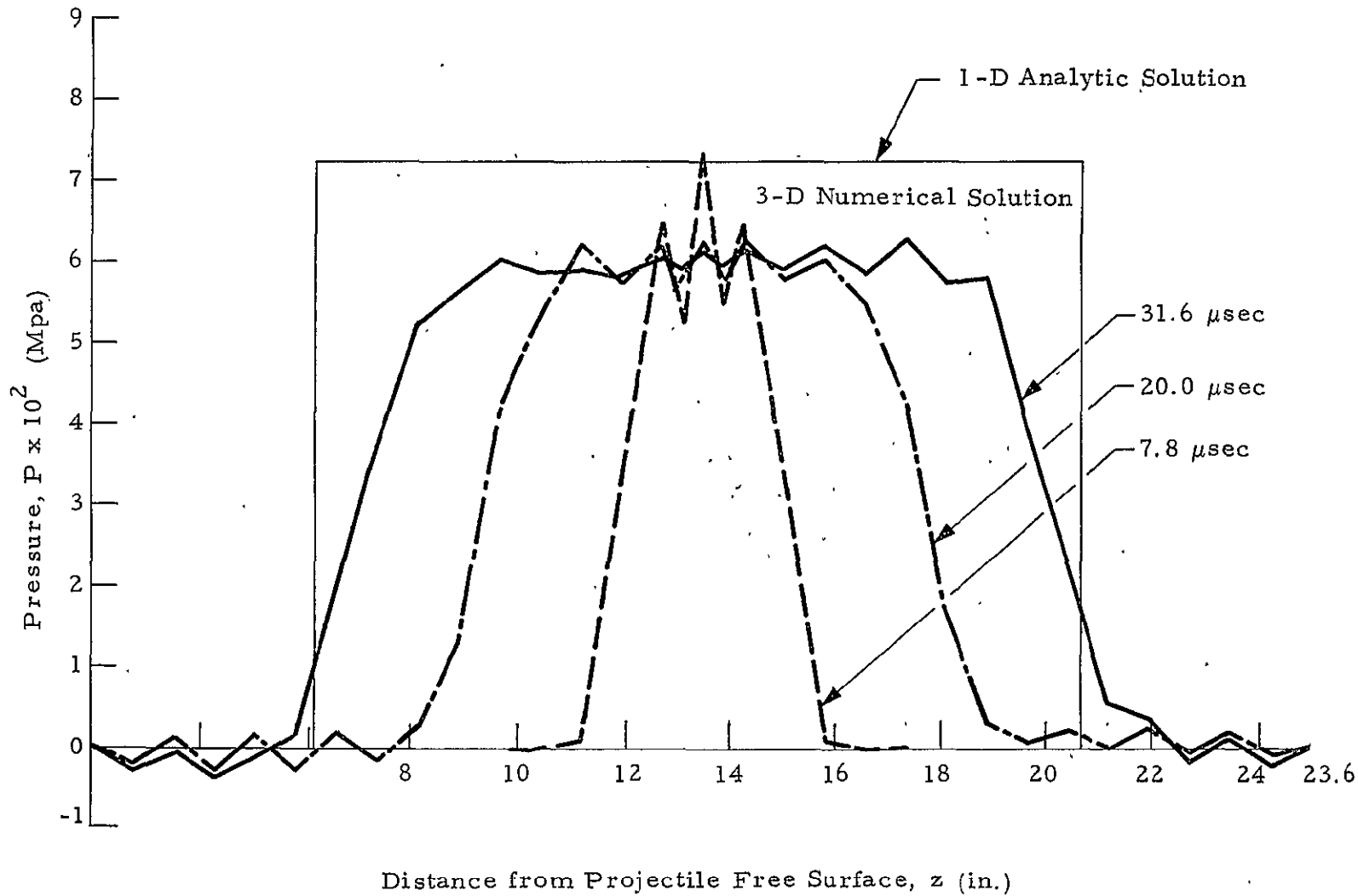


Fig. 7-21 — Pressure Distributions at Various Times Using 16 Quadratic Elements
($a = 2.0$, $\alpha = 0.0$)

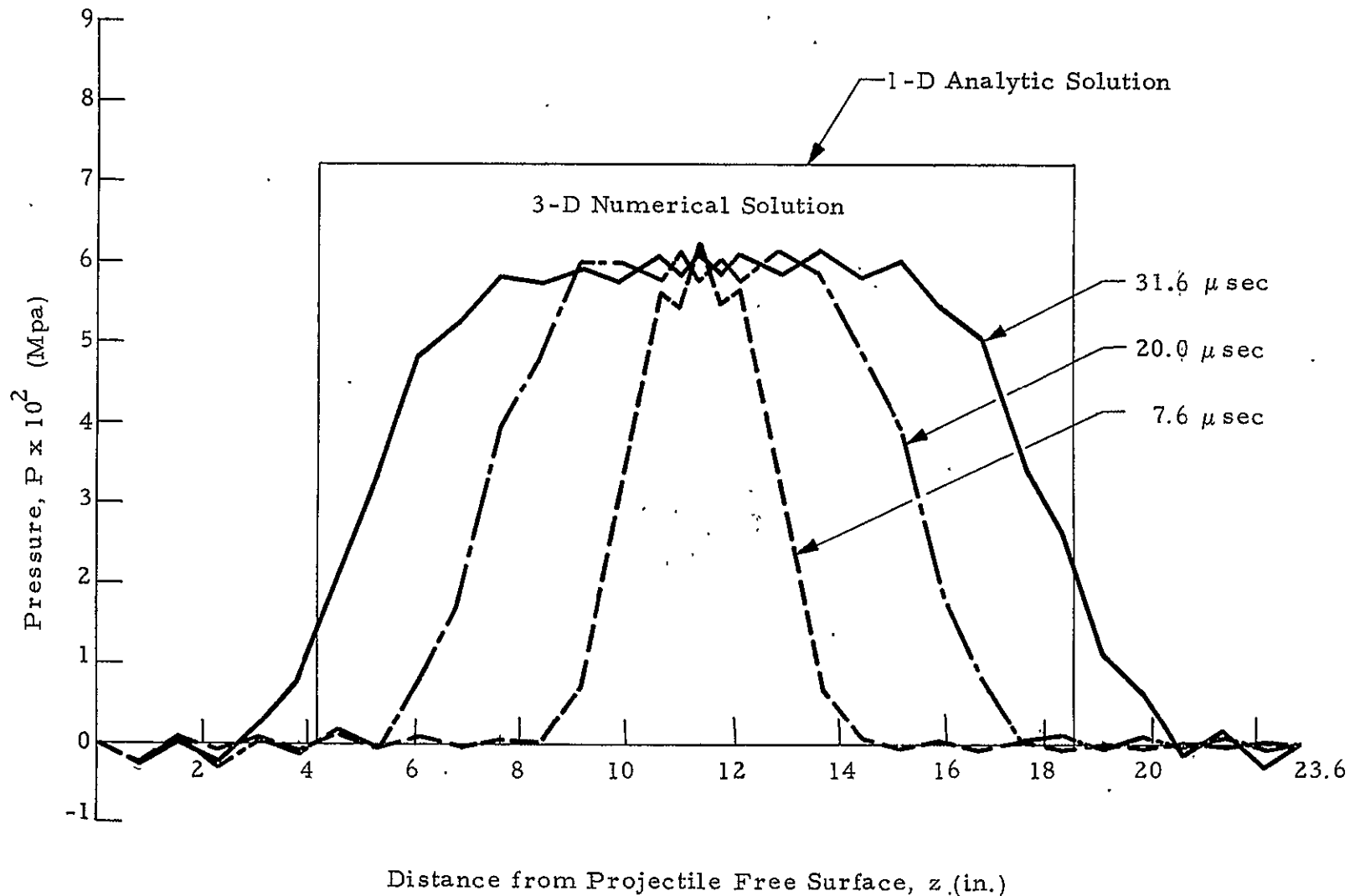


Fig. 7-22 — Pressure Distributions at Various Times Using 16 Quadratic Elements
($a = 4.0$, $\alpha = 0.0$)

Table 7-1
 PROPAGATION VELOCITY OF PRESSURE WAVES IN TARGET
 AT VARIOUS TIMES AFTER IMPACT
 (WITH 30 LINEAR ELEMENTS)

Poisson Ratio, $\nu = 0.33$; Young's Modulus, $E = 10^7$ psi;
 Impact Velocity, $V_o = -262.50$ ft/sec

Time, t(μsec)	0	5.0	10.0	18.0	26.0	31.6	35.0
Shock Speed, C _s (ft/sec)	17533.4	17756.9	17666.0	17677.2	17611.2	17651.2	17645.0

7-29

Rankine-Hugoniot — C_s = 17575.1 ft/sec

$$3\text{-D Elastic Waves} — C_s = \sqrt{\frac{(1-\nu)E}{(1+\nu)(1-2\nu)\rho}} = 19924.2 \text{ ft/sec}$$

where ν is the Poisson ratio and E is Young's modulus. With $\nu = 0.33$ and $E = 10^7$ psi for aluminum, Eq. (7.9) gives $C_{s_{El.}} = 19924.2$ ft/sec, which deviates from the values obtained by the present approach by about 10%. This implies that the compressibility effects play an important role in the dynamic response of materials under high velocity impact loads. In addition, although in the present hydrodynamic model the material is assumed to be inviscid, the dissipation resulting from the equation of state and numerical viscosity as well may affect the local speed of the pressure waves.

Momentum and Energy Distributions: Momentum and total energy distributions at $t = 30 \mu\text{sec}$ are depicted in Fig. 7-23 for 16 linear elements, Fig. 7-24 for 30 linear elements, and Fig. 7-25 for 16 quadratic elements. In these plots, the parameters $a = 2.0$ and $\alpha = 0$ are used. A better accuracy using 30 linear elements against 16 quadratic elements is obvious. In particular, as seen in the rarefaction region, the momentum and total energy distributions computed using 16 quadratic elements are severely distorted by the numerical instabilities. Hence, a larger parameter a is needed, although it is not so obvious from the plots of pressure distributions.

7.2 HYDROELASTO-VISCOPLASTIC MODEL

The crucial difficulties encountered in developing the CELFE code are caused by the following facts: (1) the occurrence of shock waves, and/or the local existence of large gradients in physical quantities; (2) the coupling procedure for global analysis; and (3) the massive computer storage and computation time required due to the three-dimensional nature. By excluding the latter two factors, the simple one-dimensional inviscid test problem discussed in Section 7.1.2 verified the success of the algorithm formulated in Section 5 in treating the shock propagation in the impact zone. A similar approach is applied in this subsection to demonstrate the actual simulation of the impact zone using the weak solution algorithm developed in Section 5.

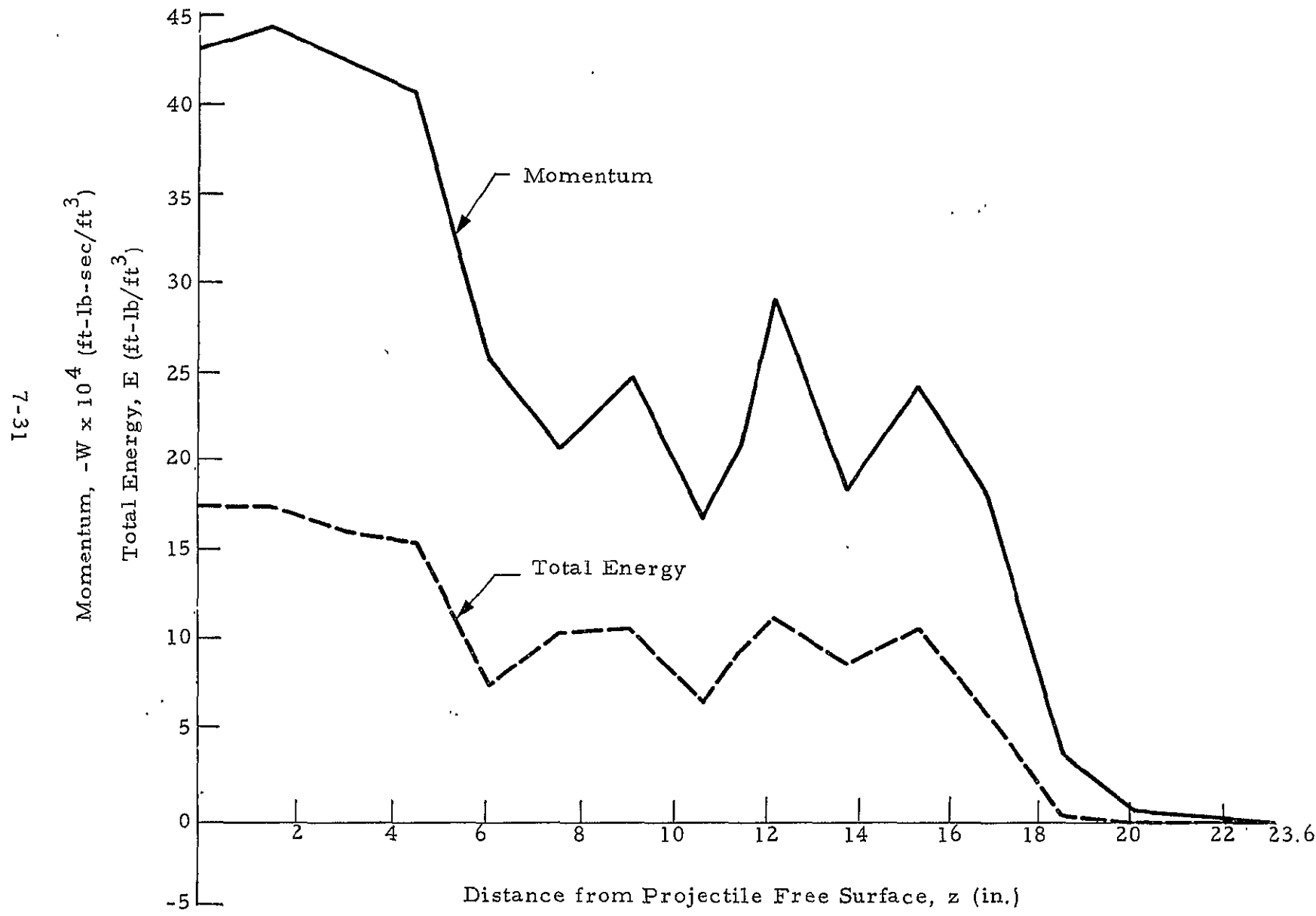


Fig. 7-23 — Momentum and Total Energy Distributions at $t = 30.0 \mu\text{sec}$
(16 Linear Elements; $a = 2.0$, $\alpha = 0.0$)

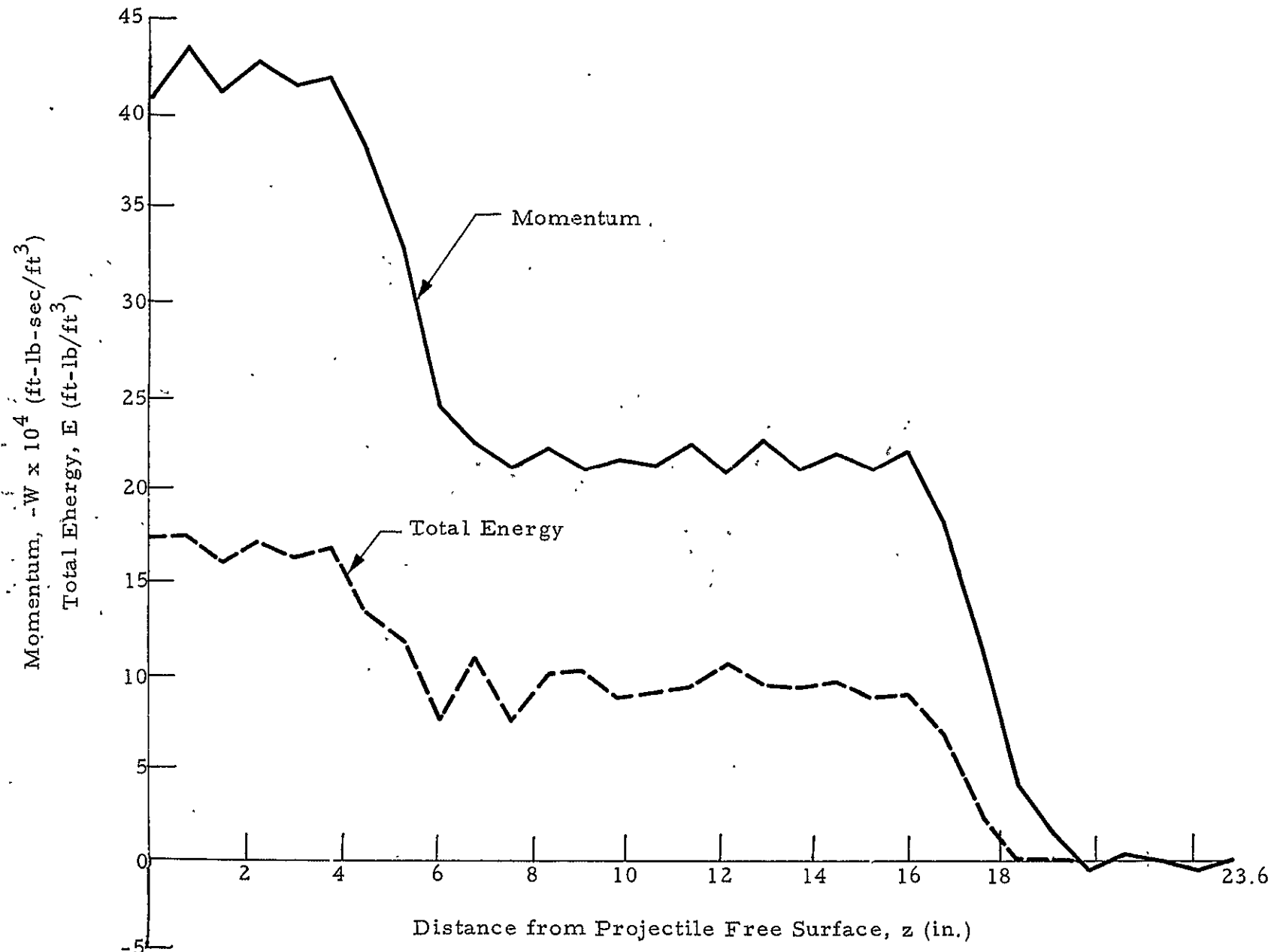


Fig. 7-24 — Momentum and Total Energy Distributions at $t = 30.0 \mu\text{sec}$
(30 Linear Elements; $a = 2.0$, $\alpha = 0.0$)

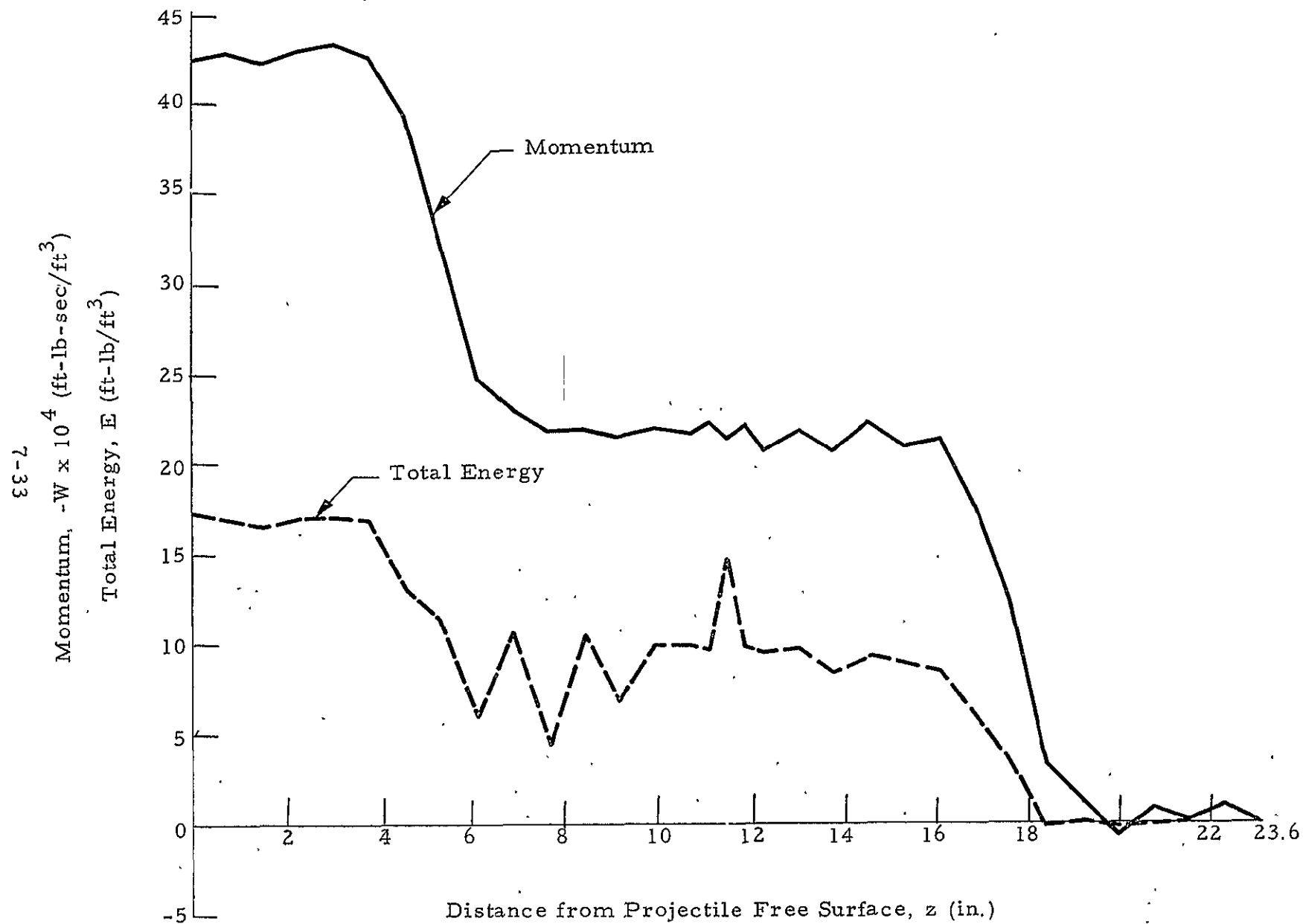


Fig. 7-25 — Momentum and Total Energy Distributions at $t = 30 \mu\text{sec}$
(16 Quadratic Elements; $a = 2.0$, $\alpha = 0.0$)

7.2.1 One-Dimensional Problem in Eulerian Mode

The one-dimensional impact problem discussed earlier is used also to test the present model. The problem description and the finite element mesh have been shown in Figs. 7-6a and 7-6b. In the computations, the material constants are assumed to be:

$$\begin{aligned} \text{Initial density, } \rho_0 &= 0.100 \text{ lb/in}^3 \\ \text{Shear modulus, } \mu &= 4.002 \times 10^6 \text{ psi} \end{aligned}$$

The impact velocity, $v_0 = 262.5 \text{ ft/sec}$, and Los Alamos equation of state are also used for the present problem.

In order to compare with the test problem in Section 7.1.2, the yielding prediction is not incorporated at first. Similar conclusions as discussed in Section 7.1.2 can be drawn from the present test case. Figure 7-26 illustrates the axial stress and pressure developments at the impact surface using 30 linear elements, with the values of $a = 4.0$ and $\alpha = 0.0$.

When the yield strength, $Y = 100.5 \text{ ksi}$, is taken into account, as depicted in Fig. 7-27, the stress and pressure buildups decrease due to the formation of viscoplastic flow. As time increases, however, the stress and pressure approaches the same values as shown in Fig. 7-26.

7.2.2 Two-Dimensional Test Case for Unidirectional Fiber Composites – Eulerian Mode

This test case was performed to examine the workability of the code for anisotropic materials. The configuration of the problem is depicted in Fig. 7-28, with target made of graphite HM/ERLA4617, and projectile of aluminum. The material properties are listed in Table 7-2. In these runs, the fibers are assumed to be parallel to the x-axis, and the projectile is isotropic.

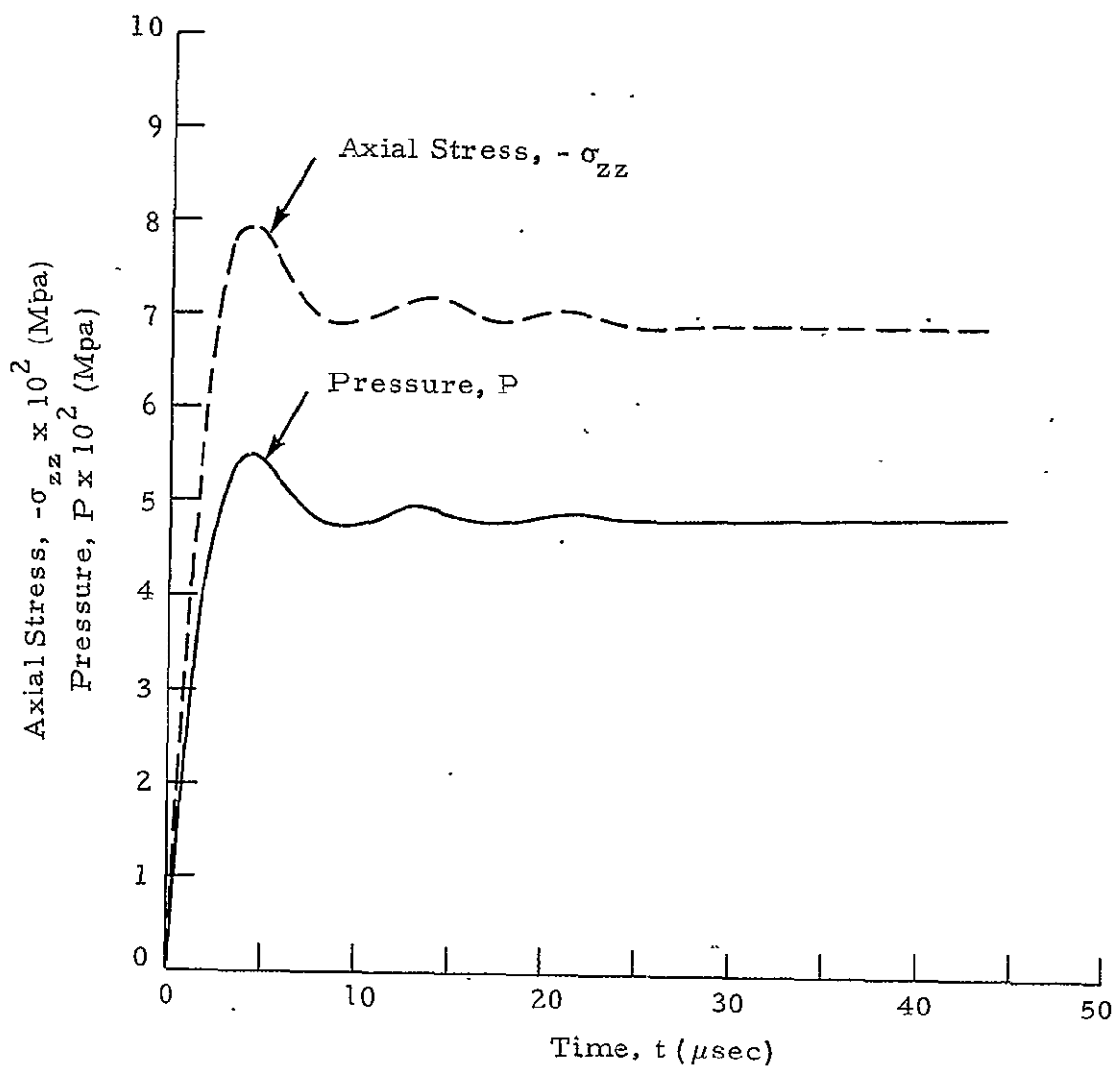


Fig. 7-26 - Axial Stress and Pressure Developments at the Interface Using 30 Linear Elements ($a = 4.0$, $\alpha = 0.0$) — Purely Elastic Case

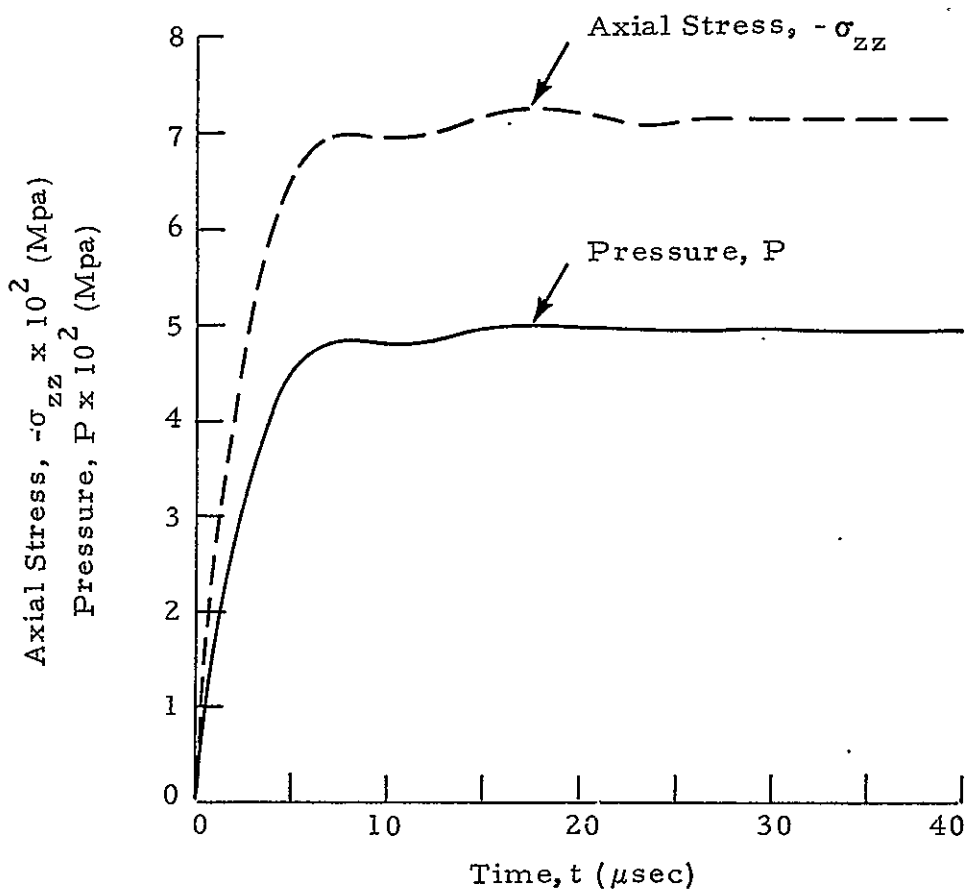


Fig. 7-27 - Axial Stress and Pressure Developments at the Interface
Using 30 Linear Elements ($a = 4.0$, $\alpha = 0.0$) — Viscoplastic Case

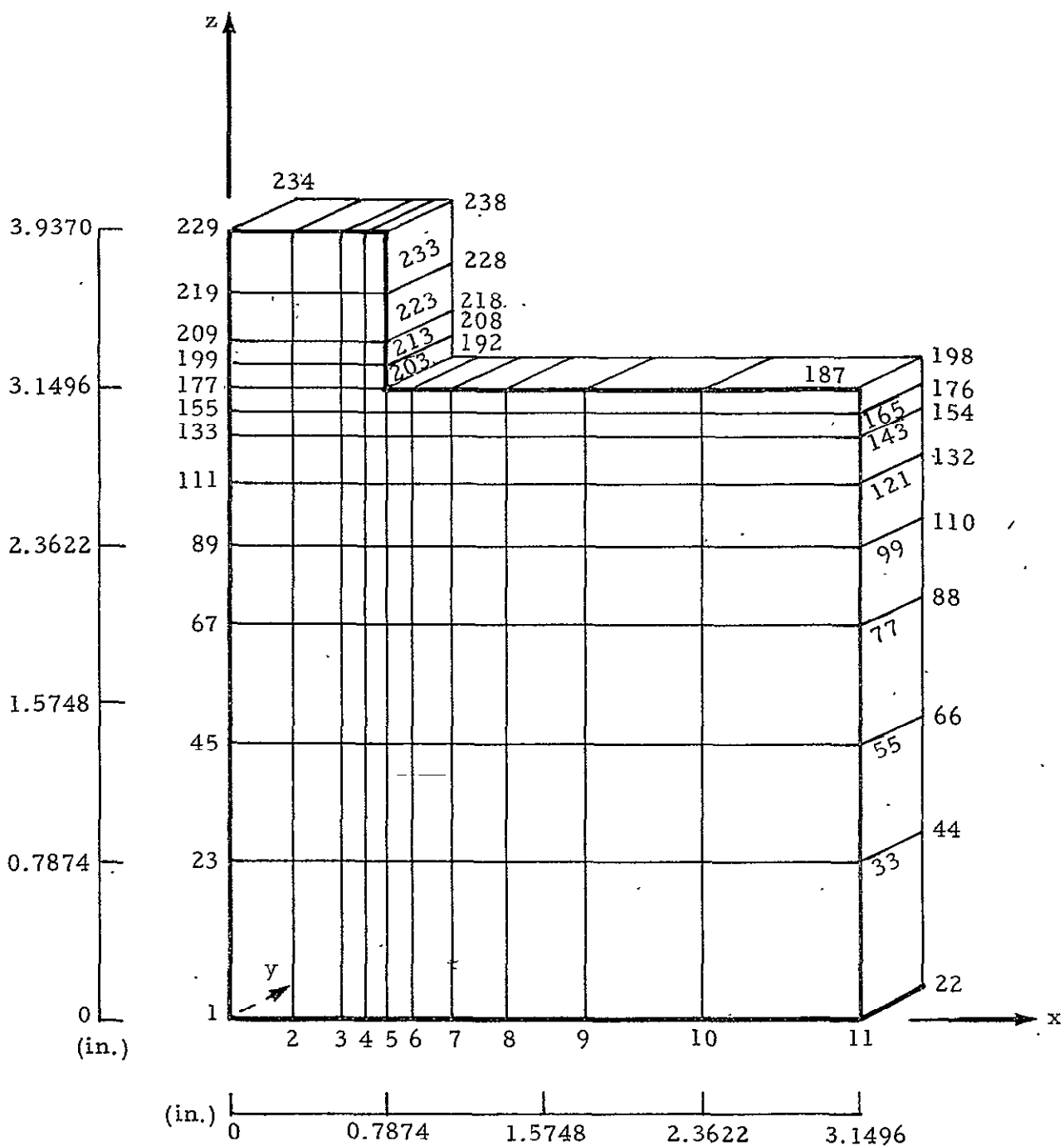


Fig. 7-28 - Finite Element Mesh and Node Numbering for a Two-Dimensional Problem (Using Three-Dimensional Elements)

Table 7-2
PHYSICAL PROPERTIES FOR A GRAPHITE
HM/ERLA 4617 TARGET HIT BY AN ALUMINUM
PROJECTILE

	Target	Projectile
Material	Graphite HM/ERLA4617	Aluminum
Density (lb/in ³)	0.056	0.101
Elastic Modulus (psi)	$E_{\ell 11} = 27.5 \times 10^6$ $E_{\ell 22} = E_{\ell 33} = 1.0 \times 10^6$	10.5×10^6
Shear Modulus (psi)	$G_{\ell 12}, G_{\ell 13} = 0.9 \times 10^6$ $G_{\ell 23} = 0.4 \times 10^6$	4.002×10^6
Poisson's Ratio	$\nu_{\ell 12}, \nu_{\ell 13} = 0.1$ $\nu_{\ell 23} = 0.4$	0.33
Uniaxial Failure Stresses (ksi)	$S_{\ell 11T} = 122.0$ $S_{\ell 11C} = 128.0$ $S_{\ell 22T}, S_{\ell 33T} = 6.1$ $S_{\ell 22C}, S_{\ell 33C} = 28.5$ $S_{\ell 12s}, S_{\ell 13s} = 8.9$ $S_{\ell 23s} = 5.6$	Static Yield: 40.0 Fracture Stress: 100.5

Figures 7-29 and 7-30 show the normal stresses and pressure developed versus time at nodes 155 and 177, respectively, with an impact velocity, $v_0 = 0.0192 \text{ cm}/\mu\text{sec}$ (630 ft/sec), normal to the target surface. The stress and pressure distributions at various sections for a given time are illustrated in Fig. 7-31a and b. The onset of the failure in the target is found around 0.06 μsec . The failure zone propagates outward uniformly as time increases.

Runs were also made for $v_0 = 24610.0 \text{ ft/sec}$. It was found that, with the mesh depicted in Fig. 7-28, the spurious oscillations are severe as shown in Fig. 7-32. This indicates that the mesh is too coarse for an impact velocity of this order of magnitude. Failure occurred almost immediately after the impact ($t = 0.02 \mu\text{sec}$), and the propagation of the failure zone is depicted in Fig. 7-33. As shown in Fig. 7-33a, the failure detected at nodes 77, 111 through 115 may be caused by the numerical instabilities. Thus, finer mesh is required for larger impact velocity.

7.2.3 Test Case for CELFE Code

During the development of the CELFE program, various runs of 1-D problems were repeated for debugging purposes. The mesh composed of 30 linear elements with a prescribed impact zone is shown in Fig. 7-34. The impact zone contains grids from 29 to 124. Notice that, in this particular case, we assigned all the grids to be Eulerian at $t = 0$, except those interface nodes 29 through 32, instead of using Lagrangian mesh (i.e., moving mesh with relative velocity $\Omega_k = 0$) as suggested in Section 6. Notice also in the Lagrangian zone, i.e., the grids 1 through 28, that similar 3-D linear elements are used, and can thus be regarded as the L_c zone.

Following the procedure discussed in Section 6, the weak solution formulation is used to analyze the impact zone, and the classical approach using 3-D solid elements is used to handle the L_c zone. The runs were

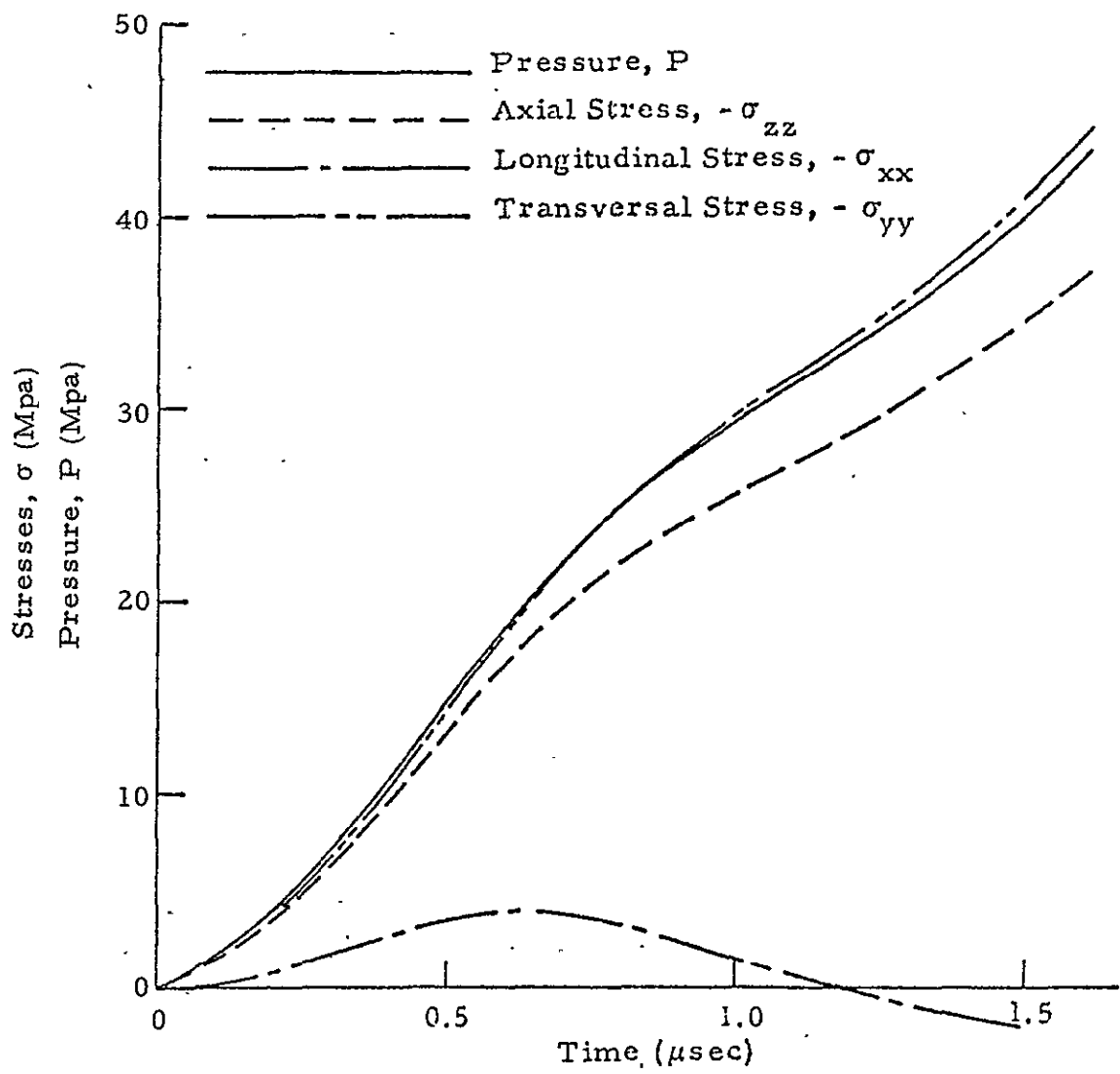


Fig. 7-29 - Stresses and Pressure Developments at Node No. 155 (Target - Graphite HM/ERLA4617, Projectile - Aluminum, $V_o = 630$ ft/sec)

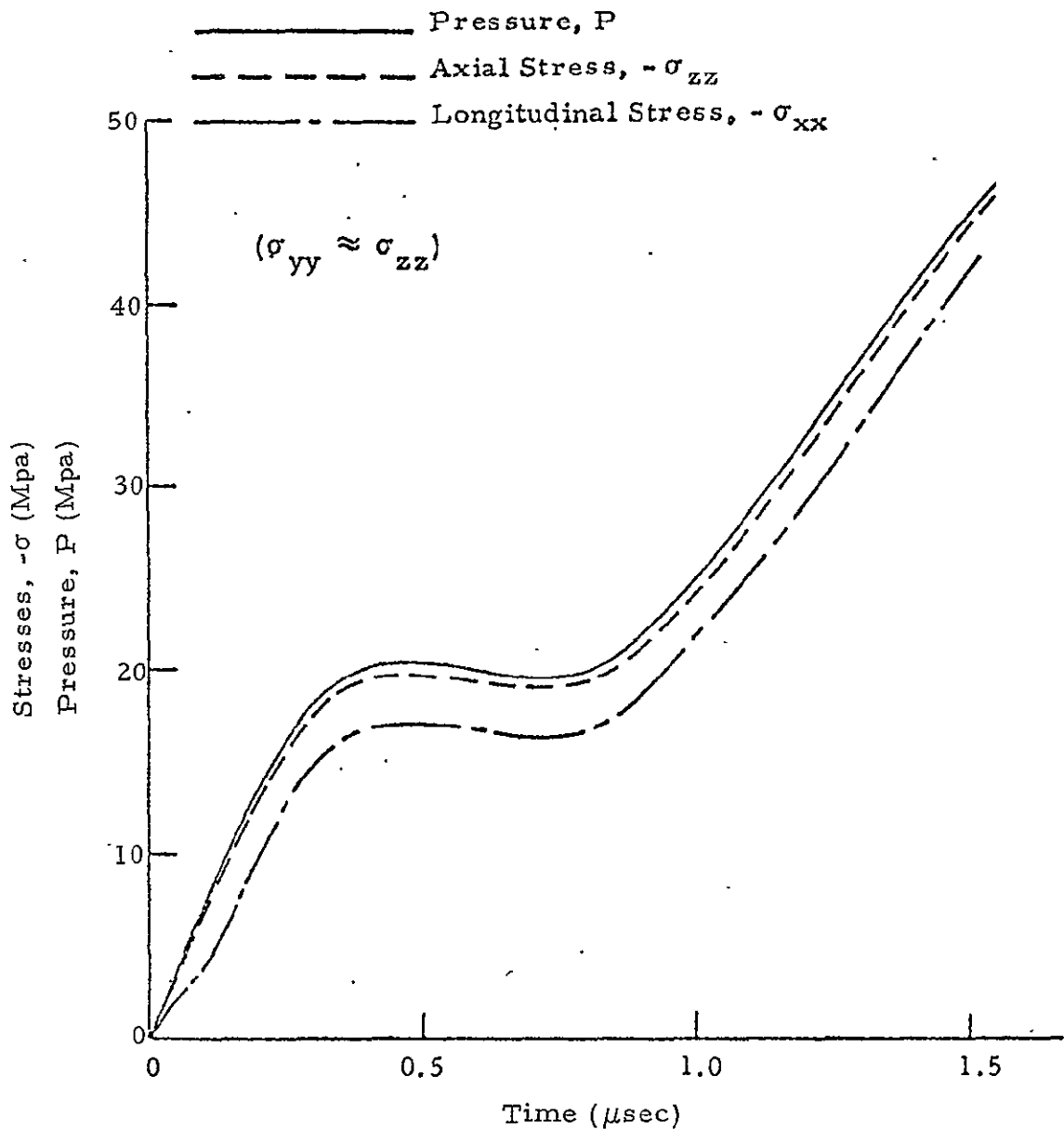


Fig. 7-30 - Stresses and Pressure Developments at Node No. 177 (Target – Graphite HM/ERLA4617, Projectile – Aluminum, $V_0 = 360 \text{ ft/sec}$)

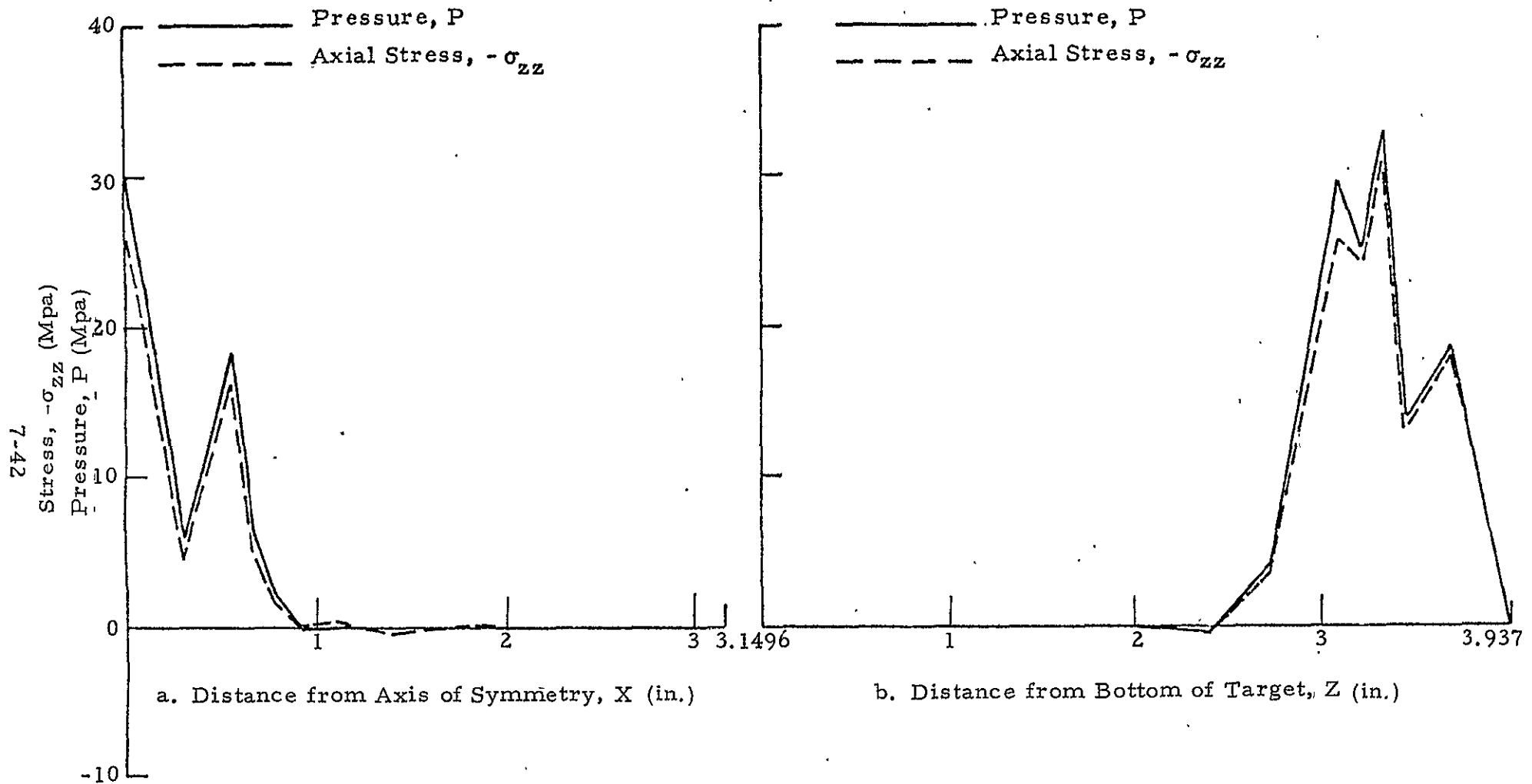


Fig. 7-31 - Axial Stress and Pressure Distributions at $t = 1.0 \mu\text{sec}$; (a) on (Y, Z) -Plane at $Y = 0$, $Z = 3.0315 \text{ in.}$; (b) on the Axis of Symmetry (i.e., $X = Y = 0$) (Target - Graphite HM/ERLA 4617, Projectile - Aluminum, $V_0 = 630 \text{ ft/sec}$)

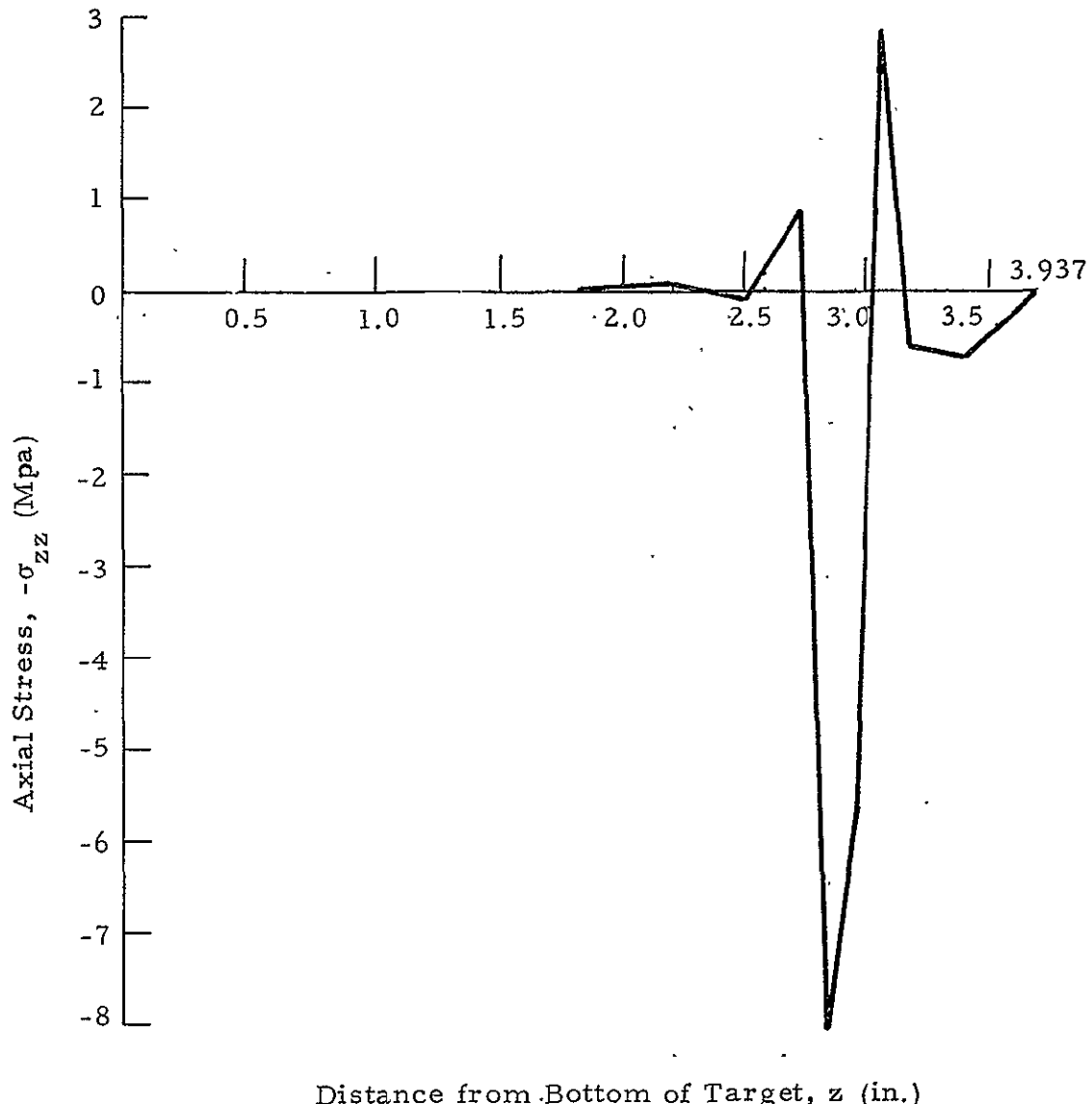
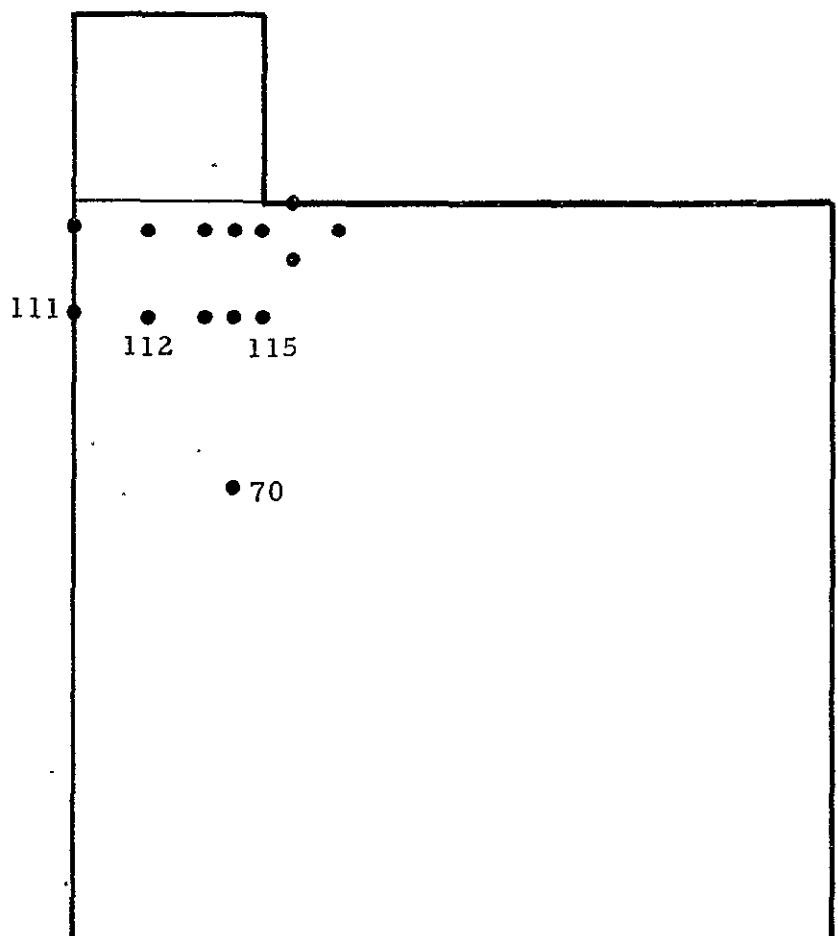


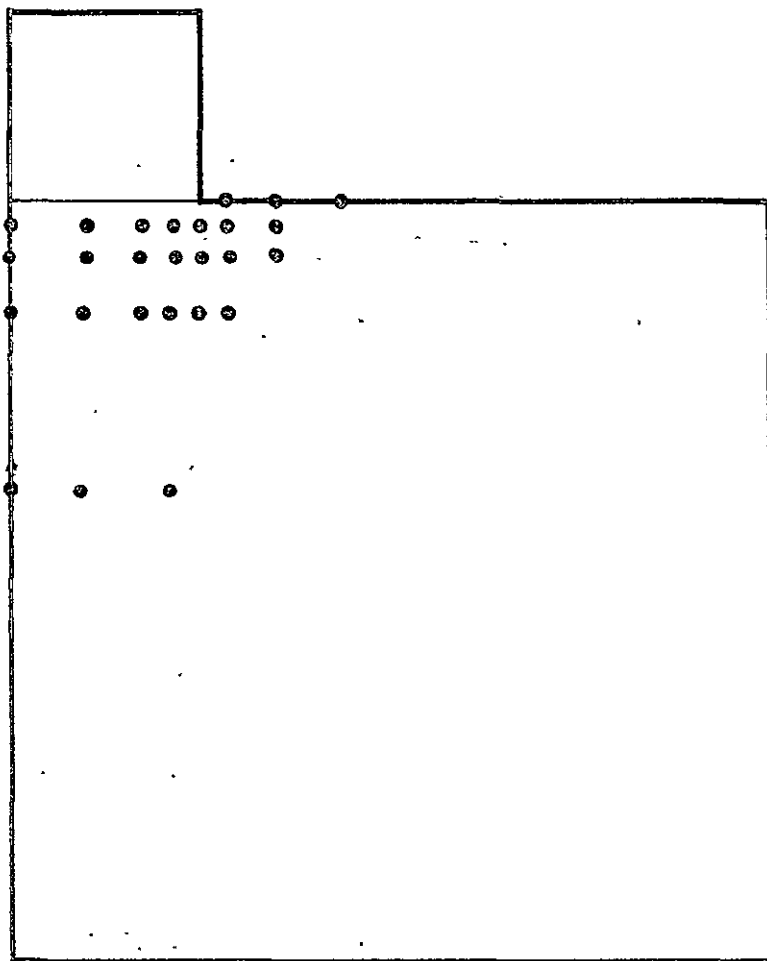
Fig. 7-32 - Axial Stress Distribution at Time $t = 0.2 \mu\text{sec}$
 $(V_o = 24610.0 \text{ ft/sec})$

● Predicted Fracture Zones



(a) $t = 0.02 \mu\text{sec}$

Fig. 7-33 - Predicted Fracture Failure of Unidirectional Composites
Due to High Velocity Impact ($V_0 = 24610.0 \text{ ft/sec}$)



(b) $t = 0.10 \mu\text{sec}$

Fig. 7-33 - (Concluded)

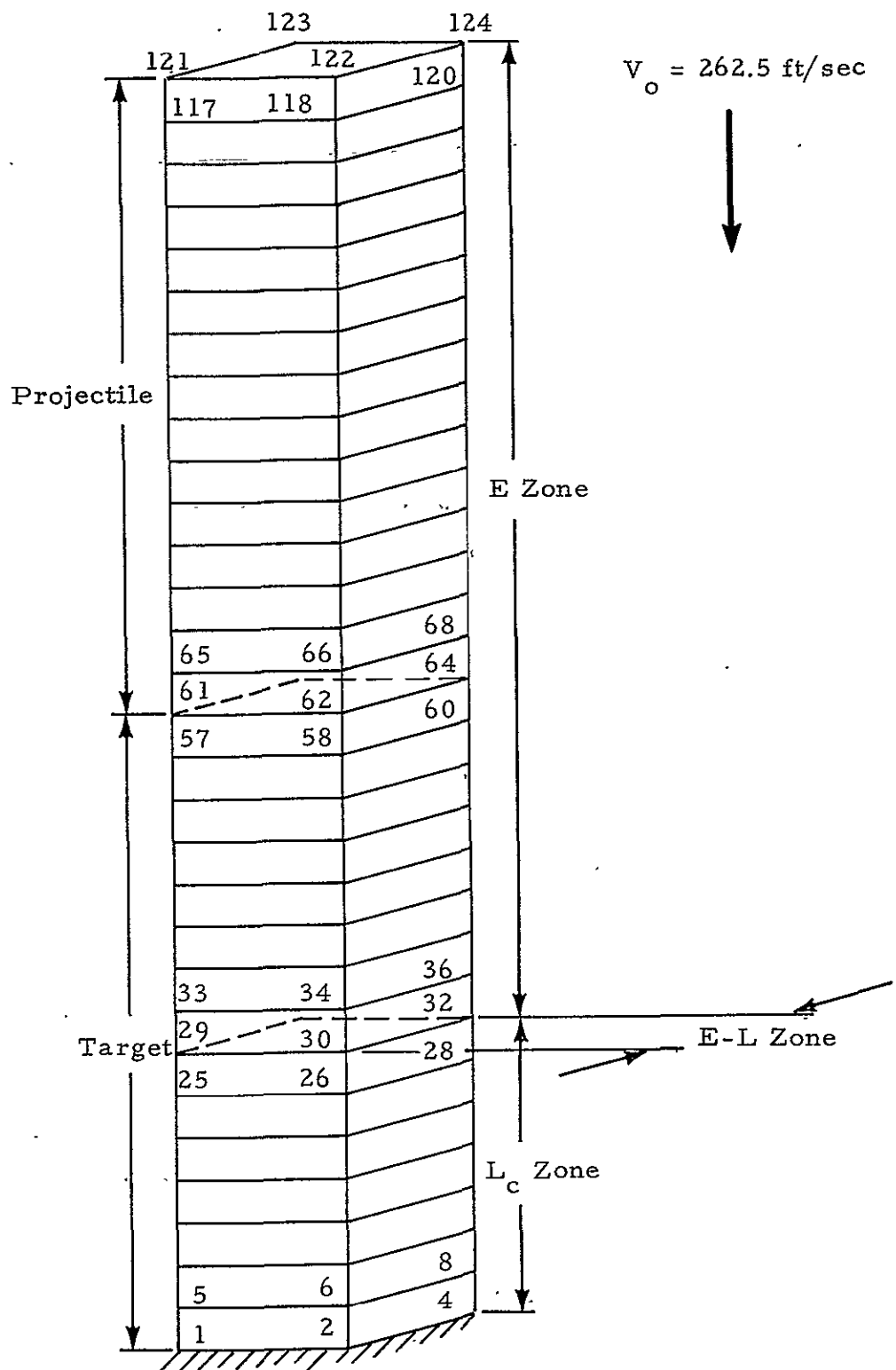


Fig. 7-34 - Finite Element Mesh of CELFE for 1-D Problem

made using the in-core CELFE option. The numerical results are illustrated by the axial stress distributions at various times in Figs. 7-35 and 7-36. The distributions are compared with the results solved by the Eulerian code as discussed in Sections 7.1 and 7.2, and the Lagrangian mode constructed using the classical approach for the L_c zone.

The results show that the CELFE solution is almost identical to the Eulerian solution at all times.

7.3. CELFE ANALYSIS OF THREE-DIMENSIONAL IMPACT PROBLEM

The results of a 3-D impact problem are discussed in this subsection to demonstrate the CELFE in-core as well as the CELFE/NASTRAN operation. The given condition of the example can be summarized as follows:

Target: Boron AVCO 5505 plate with dimensions:
9.75 in. x 8.75 in. x 0.082 in.

Projectile: Silastic with dimensions: $(0.30)^3$ in³

Impact
Velocity: 630 ft/sec normal to the plate

The geometric configuration is depicted in Fig. 7-37, and the physical properties for the materials are listed in Table 7-3. The boron epoxy target is assumed to be unidirectional with fibers parallel to the y-axis.

7.3.1 Numerical Results for CELFE In-Core Runs

Due to the symmetry, only a quadron of the plate is considered. The finite element mesh of the model is shown in Fig. 7-38, where the impact zone consists of the first 33 elements (nodes 1 through 76), with elements 26 through 33 (nodes 62 through 76) as the translation zone (E-L zone). The remaining are assigned to the L_c zone.

The computations show that the failure starts at 0.001 μ sec after the impact. The failure front propagates as the time increases as illustrated

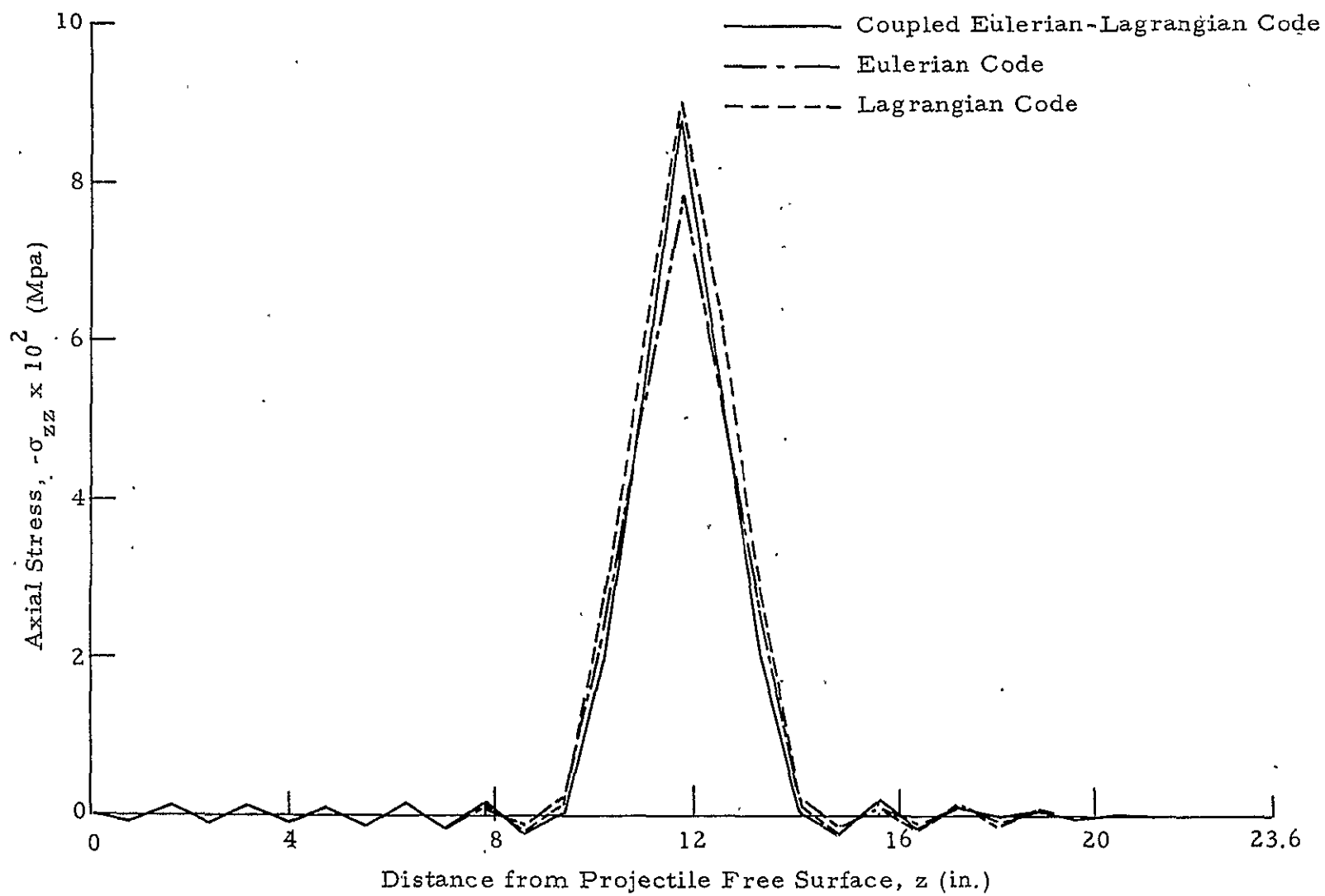


Fig. 7-35 - Axial Stress Distributions at $t = 5.0 \mu\text{sec}$ Using 30 Linear Elements

67-L

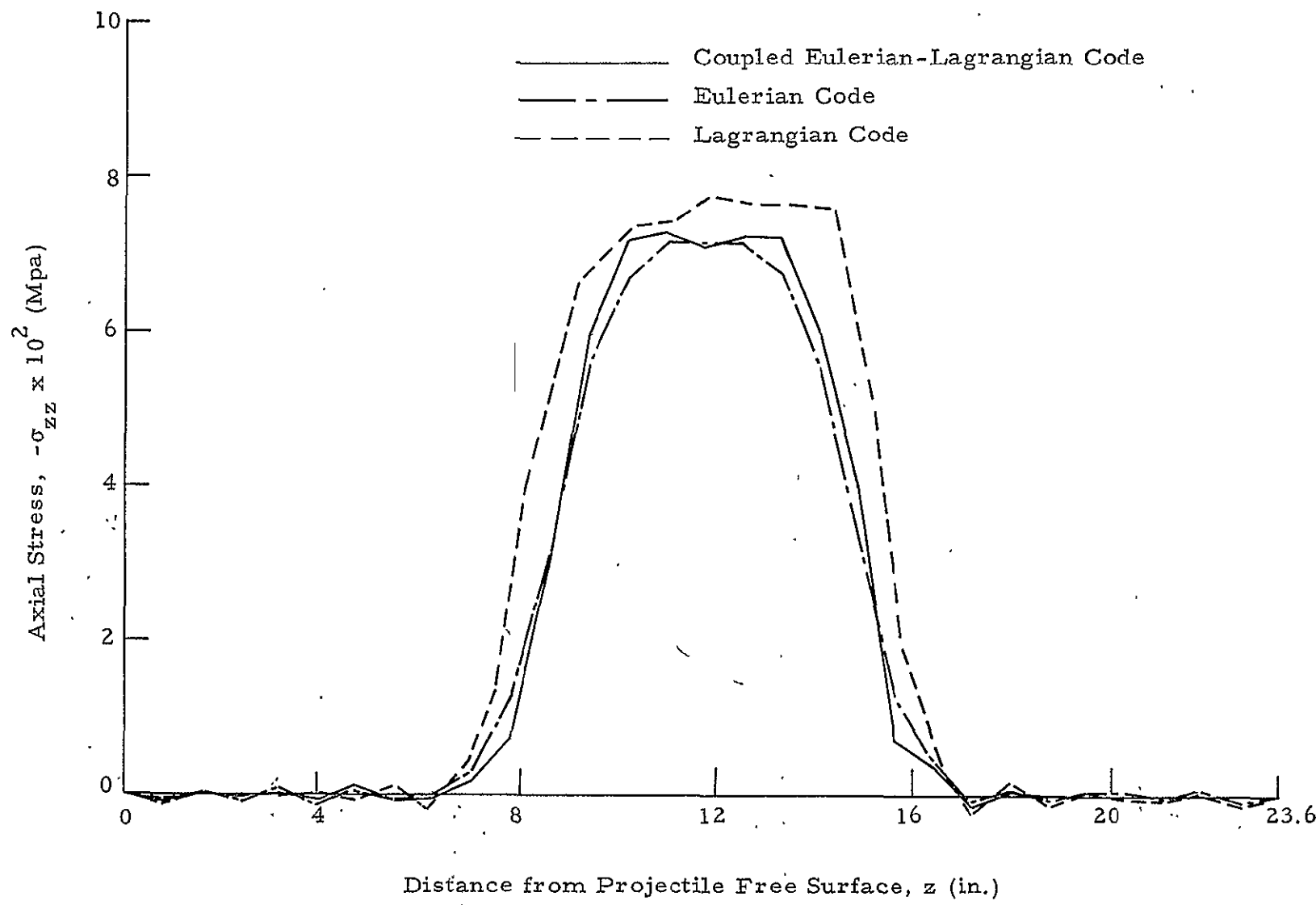


Fig. 7-36 - Axial Stress Distributions at $t = 12.0 \mu\text{sec}$ Using 30 Linear Elements

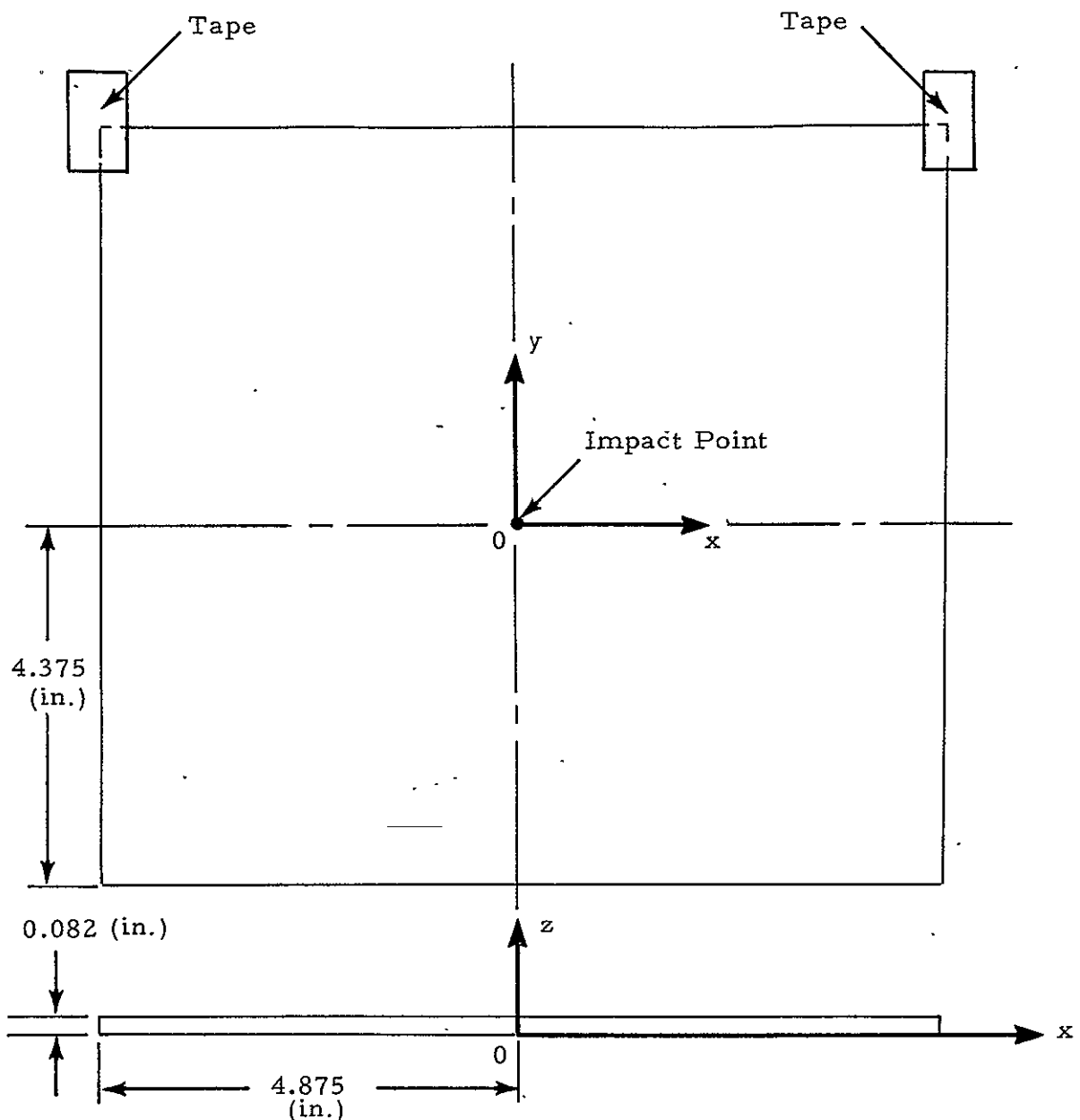


Fig. 7-37 - Sketch of Three-Dimensional Impact Problem of a Unidirectional Boron AVCO 5505 Composite by a Silastic Particle

Table 7-3
PHYSICAL PROPERTIES FOR A BORON AVCO 5505
PLATE HIT BY A SILASTIC PROJECTILE

	Target	Projectile
Material	Boron AVCO 5505	Silastic
Density (lb/in ³)	0.073	0.0512
Elastic Modulus (psi)	$E_{\ell 11} = 29.2 \times 10^6$ $E_{\ell 22} = E_{\ell 33} = 3.15 \times 10^6$	
Shear Modulus (psi)	$G_{\ell 12} = G_{\ell 13} = 0.78 \times 10^6$ $G_{\ell 23} = 0.6 \times 10^6$	0.6×10^6
Poisson's Ratio	$\nu_{\ell 12} = \nu_{\ell 13} = 0.17$ $\nu_{\ell 23} = 0.53$	
Uniaxial Failure Stresses (ksi)	$S_{\ell 11T} = 199.0$ $S_{\ell 11C} = 232.0$ $S_{\ell 22T} = S_{\ell 33T} = 8.1$ $S_{\ell 22C} = S_{\ell 33C} = 17.9$ $S_{\ell 12S} = S_{\ell 13S} = 9.1$ $S_{\ell 23S} = 8.9$	Yield: 2.7027

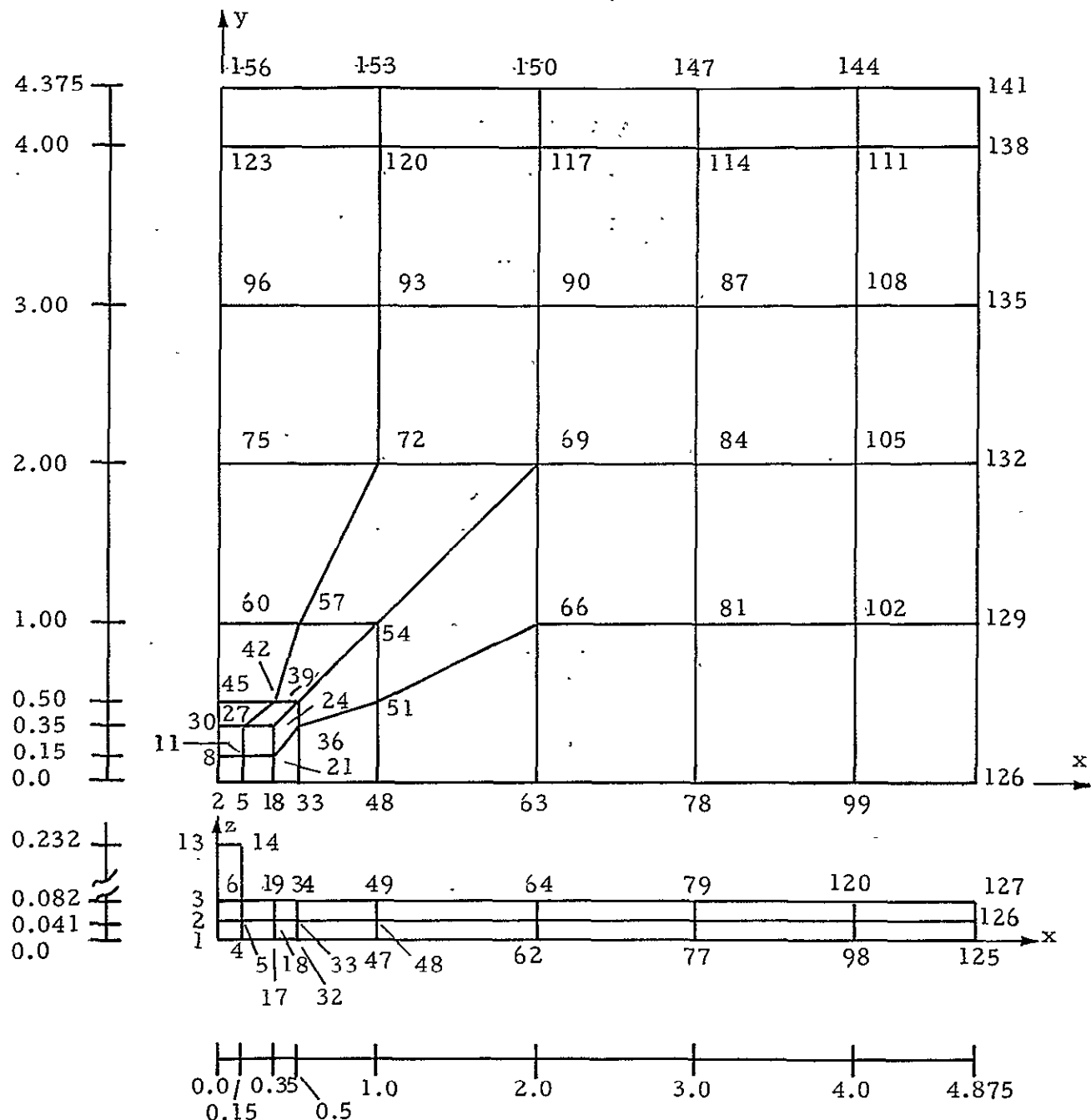


Fig. 7-38 - CELFE Finite Element Mesh for In-Core Model

in Fig. 7-39. The pressure development versus time and the normal stress distributions are shown in Figs. 7-40 and 7-41, respectively.

7.3.2 CELFE/NASTRAN Runs

The NASTRAN program adopted in the present development has been the 15.7 version from the NASA Lewis Center. During the development, the erroneous INPUTT2 and OUTPUT2 modules were corrected, and some subroutines were modified to make the interfacing procedures more efficient. The detailed discussions will be presented in Part II of this report.

In order to compare the results computed by CELFE in-core runs and CELFE/NASTRAN runs, the size of the elements for both cases are made similar. In the CELFE/NASTRAN model, the finite element mesh for the impact zone is identical to the CELFE in-core case, and is depicted in Fig. 7-42. It consists of the first 33 linear isoparametric elements. In the Lagrangian substructure, the L_c zone is assigned to be empty for simplicity, and all elements in the substructure are composed of NASTRAN general quadrilateral elements, i.e., L_N zone. The mesh is illustrated in Fig. 7-43. To ensure the displacement compatibility across the boundary, multipoint constraints (MPC) are employed to connect the CELFE and NASTRAN substructures. The connecting procedure can be illustrated as follows: A NASTRAN grid point is added to each CELFE mid-point grid lying on the E-L zone, which has now become the interface of the CELFE and NASTRAN substructure due to the empty L_c zone, e.g., the grids 163, 166, 169, 172 and 175 in the NASTRAN substructure (c.f., Fig. 7-43) are added, respectively, to the CELFE grids 63, 66, 69, 72 and 75 (Fig. 7-44). The mid-point grids are coupled by MPCs for the three translational degrees of freedom; rotational displacements are transmitted from the quadrilateral plate elements to the CELFE linear isoparametric elements by using rigid bars connected between the mid-point node, say, node 163 depicted in Fig. 7-44, and the top and bottom nodes of the solid, nodes 64 and 62, respectively.

The numerical results computed by the CELFE/NASTRAN model are found to be nearly identical to the CELFE in-core model. The deviation

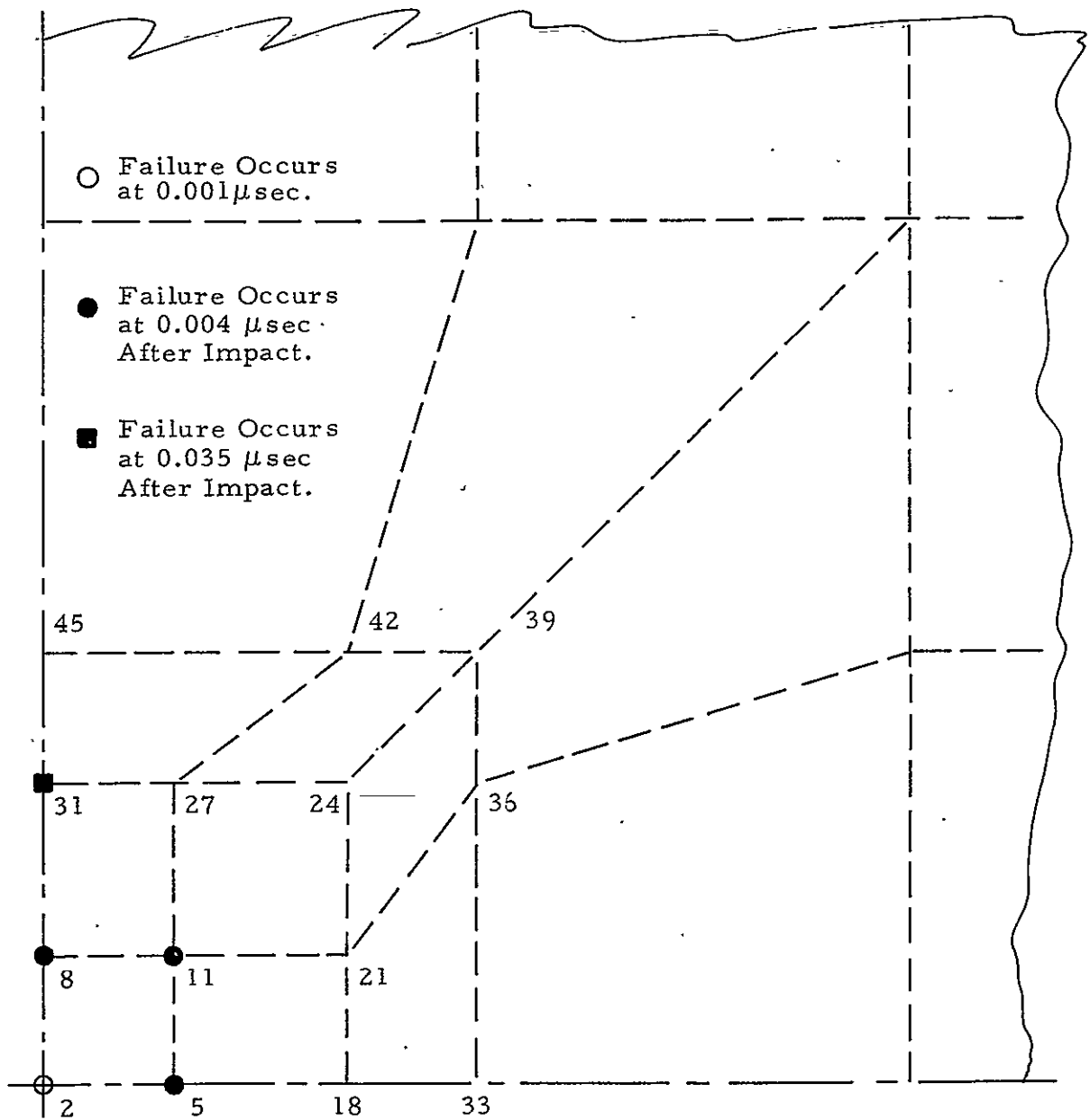


Fig. 7-39 - Propagation of Failure Front with Respect to Time
(Nodes shown are at mid-plane.)

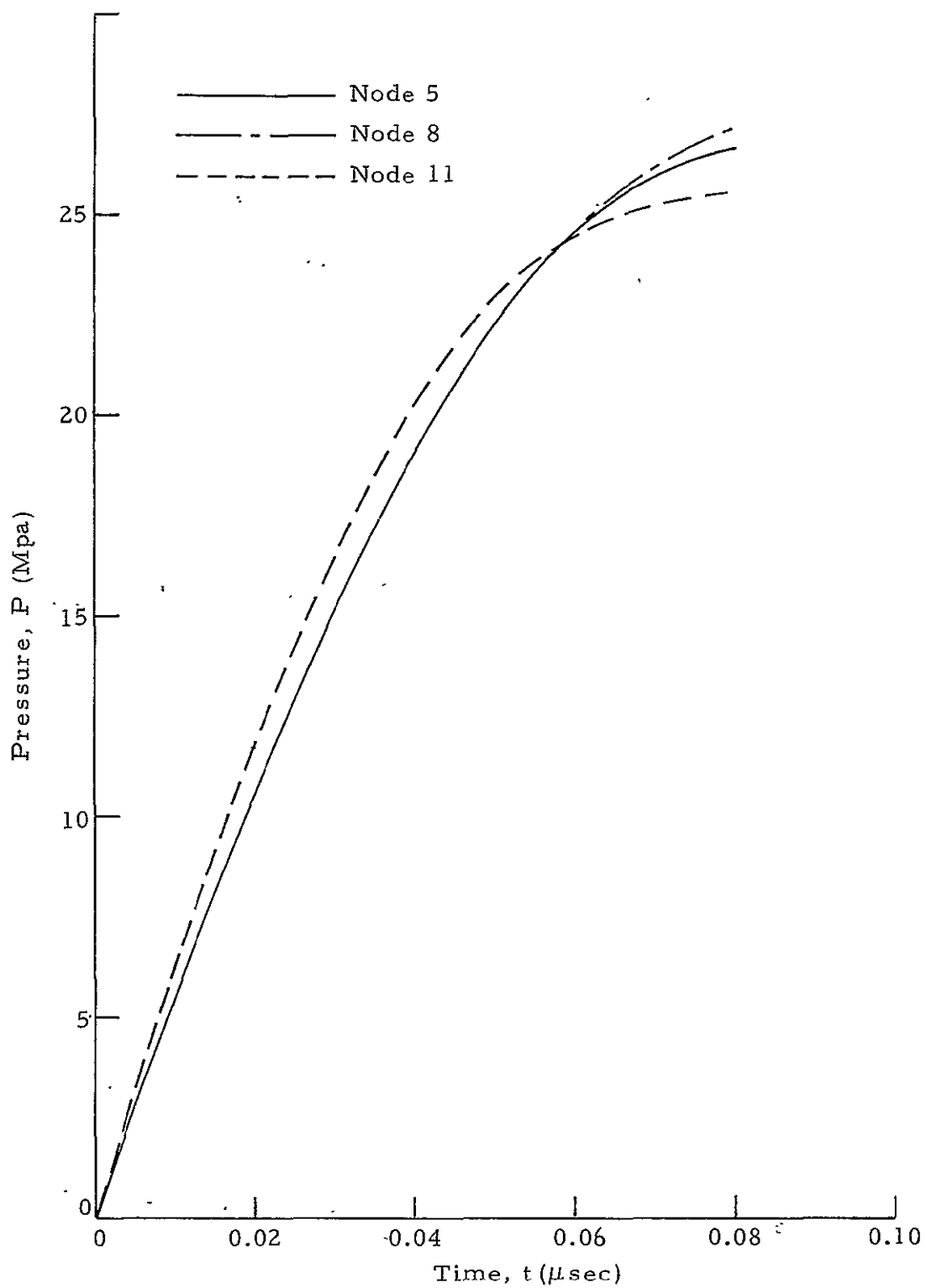


Fig. 7-40 - Pressure Developments at Various Nodal Points (Fig. 7-39)

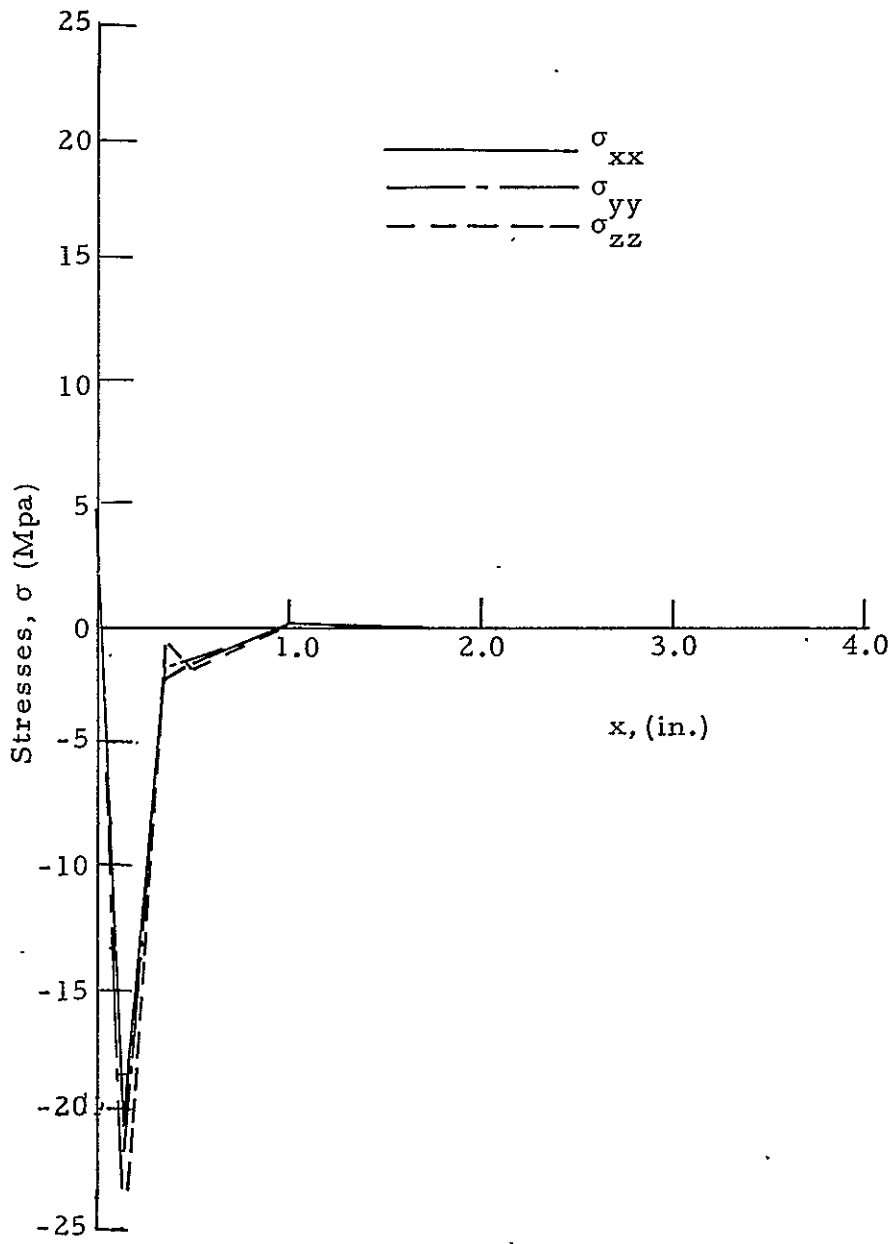


Fig. 7-41 - Stress Distributions Along x-Direction with $y = 0.0$,
 $z = 0.041$ (Fig. 7-38) at $t = 0.07 \mu\text{sec}$

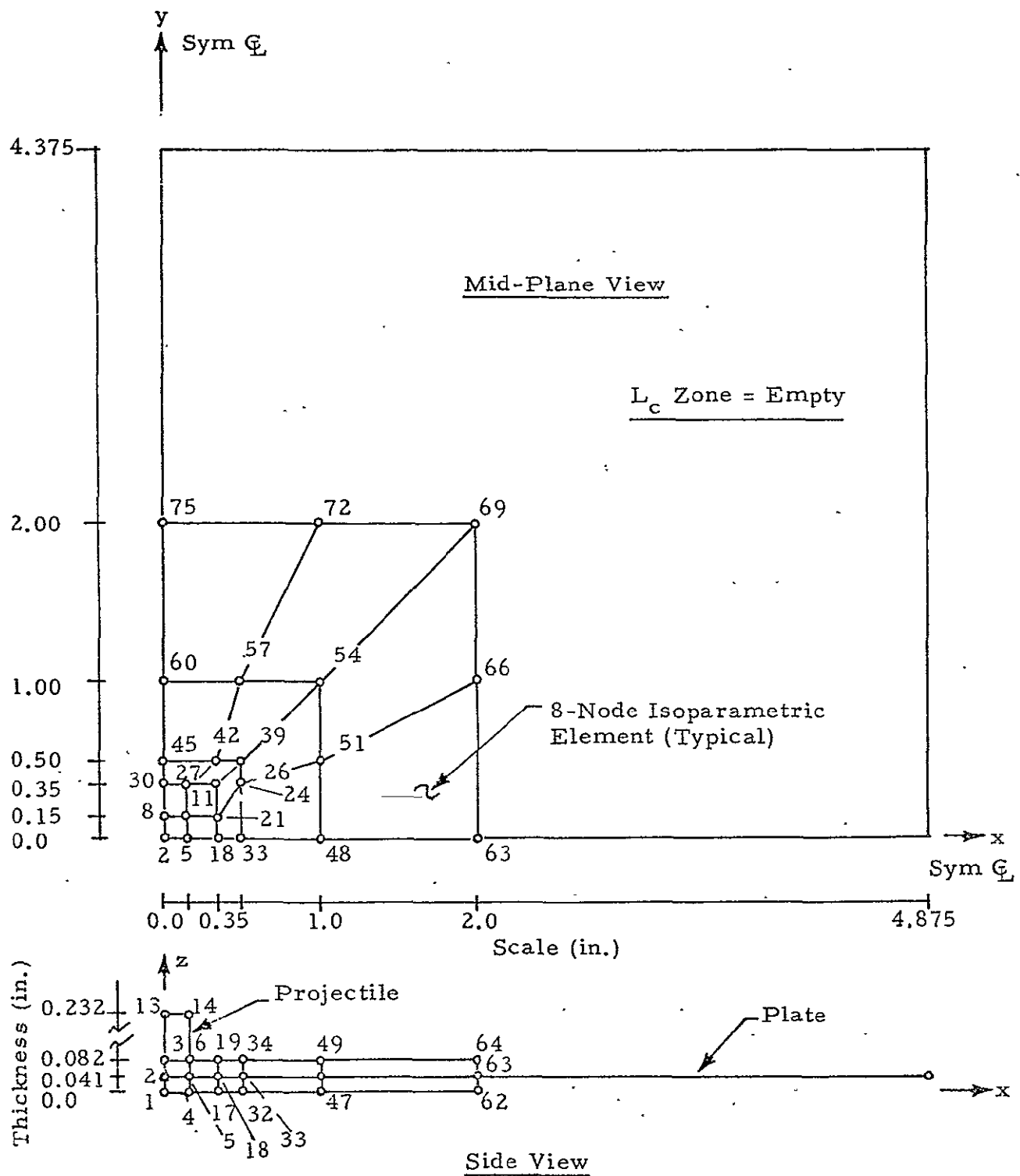


Fig. 7-42 - CELFE Finite Element Model in the CELFE/NASTRAN Runs

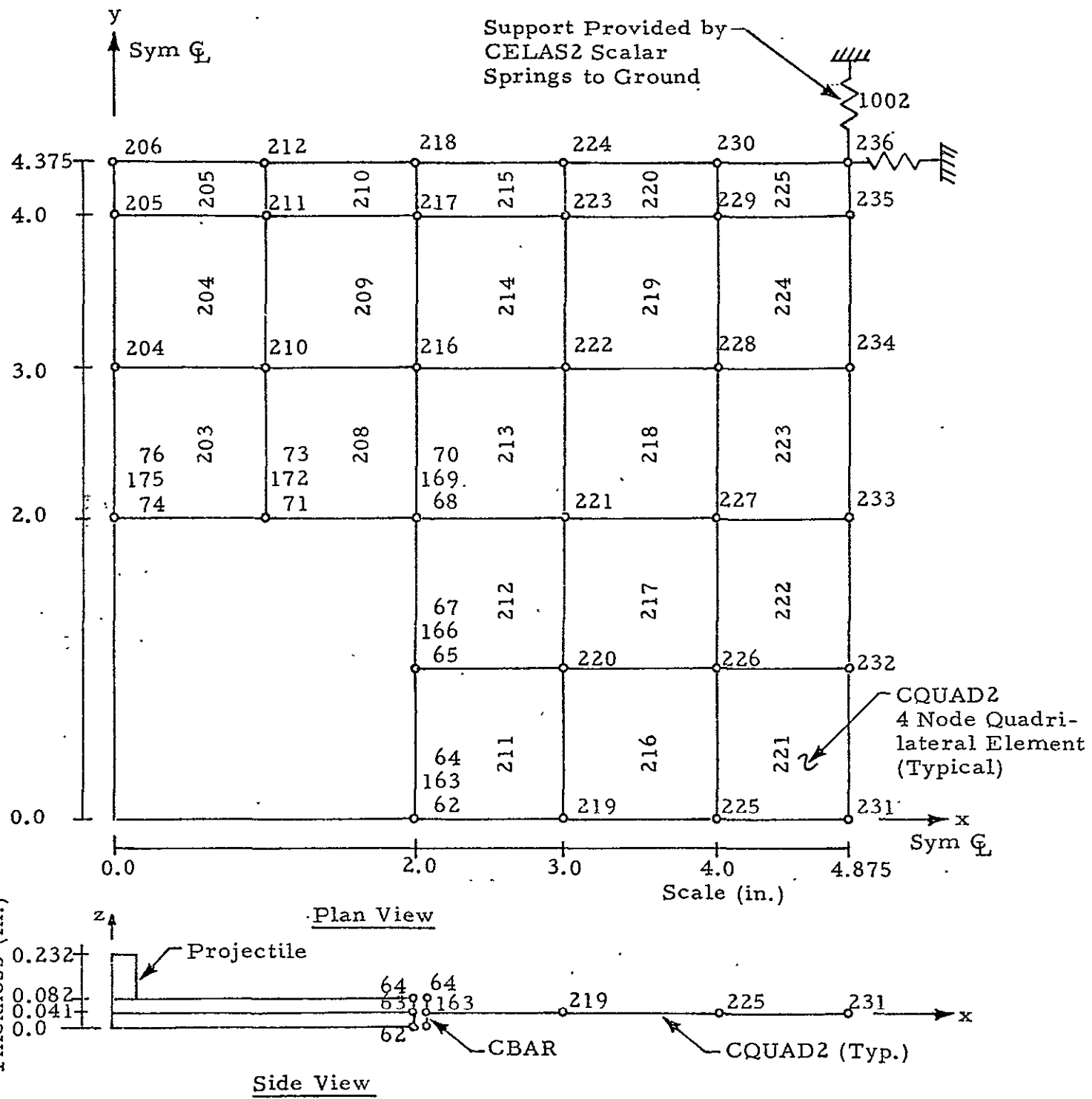


Fig. 7-43 - NASTRAN Finite Element Model in CELFE/NASTRAN Runs

MPC - Equations (typ)

$$\begin{array}{ll} X_{163} = X_{63} & X_{166} = X_{66} \\ X_{163} = Y_{63} & Y_{166} = Y_{66} \\ X_{163} = Z_{63} & Z_{166} = Z_{66} \end{array}$$

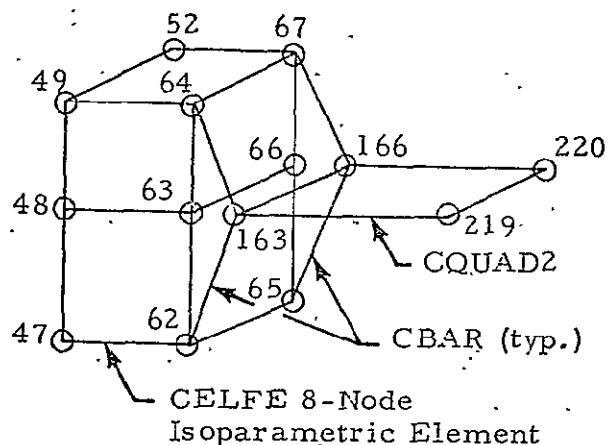


Fig. 7-44 - An Illustration of Connecting CELFE Model to NASTRAN Model

between the runs is of $0 (10^{-3})$. The spurious oscillations found in the CELFE/NASTRAN results, however, are slightly greater than the in-core runs.

7.3.3 Concluding Remarks

As mentioned previously, the numerical results obtained by CELFE in-core and CELFE/NASTRAN runs are almost identical, although in the formal case, 3-D linear isoparametric elements are used in the Lagrangian zone, and the later, 2-D plate elements are used. For the computing time, on the other hand, it requires approximately six minutes per time step for the in-core operation, in contrast to 30 minutes for the CELFE/NASTRAN operation. The substantial increase of run-time in CELFE/NASTRAN operation arises mainly due to the interfacing procedures between the CELFE and NASTRAN programs; yet the generality of the NASTRAN program may as well add some inefficiency in the computations.

During the CELFE/NASTRAN executions, it is found that the high-core is always required in the NASTRAN transient analysis module. For a 10-element (with 7 elements in the impact zone) model, 70K of core was required in the Univac 1108 system; for 16 elements, about 90K of core was set. In the present model of 54 elements (with 33 elements in the impact zone), 100K of core was assigned to the NASTRAN program. Apparently, there are inappropriate overlays and/or other errors in the transient module of the 15.7 version. This problem also added some inefficiency in the CELFE/NASTRAN executions.

It is noted that, in the present demonstration problem, the thickness of the plate is much less than the width of the plate; the ratio of the thickness to width (in both x- and y-axis) is $\epsilon = 0.082/5. = 0 (10^{-2})$. In the impact zone, the finite element mesh consists of elements with a thickness of 0.041 in., and width (in both x- and y-axis) varies from 0.15 in. to 1.0 in., i.e., the ratio varies from $\epsilon_h = 0 (10^{-1})$ to $\epsilon_h = 0 (10^{-2})$. Although isoparametric elements are used

in the impact zone where the mesh is mapped to unit cubes represented in the local coordinate system. With $\epsilon_h \ll 1$, the finite element approximation of the gradient of a physical quantity, say, ϕ , with respect to the global coordinate system, $\nabla\phi$, may still induce an error that may be magnified by $O(1/\sqrt{\epsilon_h})$. As a consequence, the mesh with ratio $\epsilon_h \ll 1$ may lead to the possibility of imposing a singular problem in the finite element approximation. This phenomenon is precisely the boundary layer type of problem encountered in dealing with high Reynolds number flows.

This phenomenon was demonstrated by the present problem in various numerical tests using various mesh arrangements. According to the experiment results conducted by I. M. Daniel and T. Liber [38], there is no failure under the impact conditions specified in this test problem. However, the numerical results computed using various mesh arrangements show that the failure occurs almost immediately after the impact. It is also shown that, for the 10-element model, (where the average mesh ratio $\epsilon_h = 0.041/0.15$) the failure front propagates faster than the other models with more regular mesh (including the in-core models), even though some measures were made to smear out the spurious oscillations. The results are improved when more elements in the impact zone become more regular, i.e., with ratio $\epsilon_h = O(1)$.

The discrepancy of the numerical results from the experiment data may partially be induced also by some other factors, such as the accuracy of the equation of state and the failure criteria. It is clear that these factors are equally or even more important than that of the singular mesh used in the impact zone to cause the inaccuracy in the computations. Hence, further investigations on this aspect is necessary in order to improve the accuracy of the CELFE program.

8. SUMMARY AND DISCUSSION

In the present study, a three-dimensional, coupled Eulerian-Lagrangian finite element (CELFE) program was developed for high velocity impact. The study was divided into two phases. Phase I was devoted to constructing a numerical algorithm for analyzing the local dynamic behavior in the vicinity of the impact point during the penetration process. The local analysis was based on a hydroelasto-viscoplastic model governed by conservation equations of mass, momentum and energy, an appropriate set of constitutive equations, and an equation of state. A computer code based on the theorem of weak solutions was developed in terms of the Eulerian mode.

In Phase II, the CELFE program was developed to extend the results obtained in Phase I to perform the global analysis of certain structures subjected to high velocity impact. The computer program was composed of three parts: the first part was generalized from the code developed in Phase I for handling the local analysis in the impact zone represented by a general moving coordinate system instead of the Eulerian system; the second part was a classical Lagrangian mode for handling the dynamic response of the remaining part of the structure induced by the impact; the third part was a coupling procedure to integrate the above two parts.

The coupling procedure, in turn, consisted of two parts. The first part was a procedure to smoothly translate the coordinate system, and thus the dynamic representation, from the Eulerian mode describing the dynamic behavior in the failure zone to the Lagrangian mode describing the dynamic response away from the impact zone. The procedure was incorporated in the CELFE program by the variation of the relative velocity with respect to the local velocity of material particles. The second part of the coupling procedure was constructed for interfacing the CELFE and NASTRAN programs

to remove any limitation of the size of the CELFE code due to excessive CELFE core storage requirements. The interfacing procedure consisted of several I/O routines installed in CELFE to read and write the matrices in NASTRAN INPUT2 OUTPUT2 formats. The large matrix equations for the conservation and constitutive equations, together with the data for the CELFE substructure to be coupled with the NASTRAN substructure, were then carried into the NASTRAN program to perform all the required manipulations using the standard NASTRAN Rigid Format 9.

During the development, various test cases were performed to investigate the validity and capability of the algorithm in various aspects. The numerical experiments show that the most difficult part in analyzing a structure subjected to high velocity impact, namely, the highly nonlinear, large deformation, and shock and failure propagation phenomena in the vicinity of the impact point, can be resolved using the finite element algorithm developed in Section 5. The massive computer core storage required for three-dimensional analysis has also been partly resolved by coupling the Eulerian and Lagrangian modes, and interfacing with NASTRAN (or any other large structural program).

As this is only the first stage of the development, the CELFE program will need further improvements and extensions. One of the immediate tasks would be a further reduction of the in-core storage by improving the arrays of existing variables in the program.

From the numerical experiments, it is found that the results will be sensitive to the equation of state. In addition, the effects of possible phase changes due to impact can be included via an appropriate equation of state. Thus, further studies on the thermodynamic aspects of the high velocity impact problem are necessary. Along this path, additional thermal effects can be incorporated into the program by modifying the governing equations.

Finally, as stated in Section 7.3.3, a substantial increase of run time (compared to the in-core execution) is needed in performing the CELFE/NASTRAN computations. This fact shows the inefficiency of using the interfacing procedure. Hence, for the long run, it is suggested that the CELFE program should be incorporated in the NASTRAN as a module.

9. REFERENCES

1. Rand Corp., Proceedings of the First Hypervelocity Impact Effects Symposium, Santa Monica, Calif., March 1955.
2. U. S. Naval Research Laboratory, Proceedings of the Second Hypervelocity Impact Effects Symposium, Washington, D. C., December 1957.
3. Arnold Research Foundation, Proceedings of the Third Symposium on Hypervelocity Impact, Chicago, February 1959.
4. U. S. Air Force, Proceedings of the Fourth Symposium on Hypervelocity Impact, Air Proving Ground Center, Eglin AFB, Fla., April 1960.
5. Colorado School of Mines, Proceedings of the Fifth Symposium on Hypervelocity Impact, Denver, October 1961.
6. Firestone Tire and Rubber Co., Proceedings of the Sixth Symposium on Hypervelocity Impact, Akron, April 1963.
7. Martin Company, Proceedings of the Seventh Hypervelocity Impact Symposium, Orlando, February 1965.
8. Proceedings of the AIAA Hypervelocity Impact Conference, AIAA, New York City, April 1969.
9. Kinslow, R., High-Velocity Impact Phenomena, Academic Press, New York, 1970.
10. Rosenblatt, M., "Analytical Study of Strain Rate Effects in Hypervelocity Impacts," NASA-CR-61323, 1970.
11. Hanagud, S., and B. Ross, "Large Deformation, Deep Penetration Theory for a Compressible Strain-Hardening Target Material," AIAA J., Vol. 9, pp. 905-911, 1971.
12. Chou, P. C., and A. K. Hopkins, Dynamic Response of Materials to Intense Impulsive Loading, Metals and Ceramics Division, Air Force Materials Laboratory, Wright-Patterson AFB, Ohio, 1973.

13. Fyfe, I. M., "Application of 'Hydrodynamic' Theory to the Low Stress Range of Hypervelocity Impact Problems," Proc. Fifth Symp. Hypervelocity Impact, Colorado School of Mines, 1961, pp. 299-305.
14. Olshaker, A. E., and R. L. Bjork, "Hydrodynamics Applied to Hypervelocity Impact," Proc. Fifth Symp. Hypervelocity Impact, Colorado School of Mines, 1961, pp. 185-239.
15. Walsh, J. M., and J. H. Tillotson, "Hydrodynamics of Hypervelocity Impact," Proc. Sixth Symp. Hypervelocity Impact, Firestone Tire and Rubber Co., Akron, Ohio, April 1963.
16. Ludloff, K. G., "A Hydrodynamic Model for Hypervelocity Impact," Ph.D. Thesis, University of California, Los Angeles, University Microfilms, Ann Arbor, Mich., 1967.
17. Halperson, S. M., "Comparisons Between Hydrodynamic Theory and Impact Experiments," Proc. Seventh Hypervelocity Impact Symposium, Martin Co., Orlando, Fla., February 1965.
18. Prater, R. F., "Hypervelocity Impact - Material Strength Effects on Crater Formation and Shock Propagation in Three Aluminum Alloys," AFML TR-70-295, Wright-Patterson AFB, Ohio, December 1970.
19. Riney, T. D., "Solution of Viscoplastic Equations for Axisymmetric Hypervelocity Impact," Second Summary Report, 3 November 1961 - 2 November 1962, APGC TDR-62-74, AD 294 959 (December 1962).
20. Riney, T. D., "Theoretical Hypervelocity Impact Calculations Using the PICWICK Code," Interim Report, 24 June 1963 - 23 December 1963, ATL-TDR-64-8, AD 434 220 (March 1964).
21. Kraus, H., "Two-Dimensional Analysis of Hypervelocity Impact on Viscoplastic Plate," Proc. Sixth Symp. Hypervelocity Impact, Firestone Tire and Rubber Co., Akron, Ohio, April 1963.
22. Thomson, R. G., "Hypervelocity Perforation of Viscoplastic Solid - Effects of Target Material Yield Strength," NASA-TR-R-221, 1965.
23. Aprahamian, R., and J. Piechocki, "Theoretical Analysis of One-Dimensional Impact Including Elastic/Plastic Effects," LMSC-B130200, Lockheed Missiles & Space Company, Hardening Technology Studies, Vol. V, Final Report, 1966.

24. Leimbach, K. R., and R. J. Prozan, "Study of Hypervelocity Impact on Orbital Space Stations," LMSC-HREC TR D306582, Lockheed Missiles & Space Company, Huntsville, Ala., April 1973.
25. Adams, D. F., "Elastoplastic Behavior of Composites," Composite Materials, L. J. Broutman and R. K. Krock (eds.), Vol. 2, Mechanics of Composite Materials, G. P. Sendeckyj (ed.), Academic Press, New York, p. 170-208.
26. Chamis, C. C., "Micro and Structural Mechanics and Structural Synthesis of Multilayered Filamentary Composite Panels," Div. Solid Mechanics, Structures, and Mechanical Design, Rpt. No. 9, Case Western Reserve University, 1967.
27. Chamis, C. C., "Failure Criteria for Filamentary Composites," NASA TN D-5367, 1969.
28. Chamis, C. C., private communication, 1975.
29. Prager, W., "An Elementary Discussion of Definitions of Stress Rate," Q. Appl. Math., Vol. 18, p. 403, 1961.
30. Vicario, A. A., Jr., and R. H. Toland, "Failure Criteria and Failure Analysis of Composite Structural Components," Composite Materials, L. J. Broutman and R. K. Krock (eds.), Vol. 7, Structural Design and Analysis, Part I, C. C. Chamis (ed.), Academic Press, New York, 1975, pp. 52-97.
31. Tillotson, J. H., "Metallic Equations of State for Hypervelocity Impact," General Atomic Report, GA-3216, 1962.
32. Richtmyer, R. D., and K. W. Morton, Difference Methods for Initial Value Problems, 2nd ed., Interscience, New York, 1967.
33. Lax, P., "Weak Solutions of Nonlinear Hyperbolic Equations and Their Numerical Computation," Comm. Pure and Appl. Math., Vol. 7, 1954, pp. 159-193.
34. Oleinik, O. A., "Discontinuous Solutions of Nonlinear Differential Equations," Uspekhi Mat. Nauk, Vol. 12, 1957, pp. 3-73.
35. Przemieniecki, J. S., Theory of Matrix Structural Analysis, McGraw-Hill, New York, 1968.
36. MacNeal, R. H., (ed.), The NASTRAN Theoretical Manual, NASA SP-221, 1969.
37. Zienkiewicz, O. C., The Finite Element Method in Engineering Science, McGraw-Hill, New York, 1971.
38. Daniel, I. M., and T. Liver, "Wave Propagation in Fiber Composite Laminates," NASA CR-135086, 1977.

Appendix
RANKINE-HUGONIOT RELATIONS

Appendix

During the short period of time in which the projectile impacts on the target, a plane shock wave is generated in the projectile as well as in the target. Due to the extremely high pressure behind the shock front, the materials can essentially be assumed to behave as inviscid, compressible fluids. The problem, including the geometric development of the impact shock, can then be treated as an unsteady, supersonic flow resembling a moving shock.

Assuming that the hemispherical shockwave profile is steady in time, the Rankine-Hugoniot relations relating the pressure, P , internal energy, ϵ , and density, ρ , behind the shock to the same quantities in front of the shock are applied. These equations express the conservation of mass, momentum, and energy in terms of the shock velocity, v_s , and particle velocity, v_p :

$$\rho_o v_s = \rho(v_s - v_p) \quad (A.1)$$

$$P - P_o = \rho_o v_s v_p \quad (A.2)$$

$$[(\epsilon - \epsilon_o) - v_p^2/2] \rho_o v_s = P_o v_s \quad (A.3)$$

where the subscript o refers to the initial (or undisturbed) values. The product $\rho_o v_s$ is called the shock impedance. Using (A.1) and (A.2), (A.3) can be written as

$$\epsilon - \epsilon_o = \frac{1}{2} (P + P_o) \left(\frac{1}{\rho_o} - \frac{1}{\rho} \right) \quad (A.4)$$

Solving for v_s and v_p from (A.1) and (A.2), we obtain

$$v_s = \sqrt{\frac{1}{\rho_o} \frac{(P_o - P)}{(\rho_o/\rho - 1)}}, \quad v_p = \sqrt{\frac{1}{\rho} (P - P_o) (\rho/\rho_o - 1)} \quad (A.5)$$

The initial pressure, P_0 , is generally very small and can be neglected in comparison with P . If shock velocity and particle velocity are known at a point on the shock front, the pressure can be computed using (A.2). One more relation is needed to solve the flow across a shock, namely, the equation of state; a specific form of the equation of state is given in Subsection 3.4.

FINAL REPORT DISTRIBUTION LIST

NASA CR 159395 and 159396

CELFE: COUPLED EULERIAN-LAGRANGIAN FINITE ELEMENT FOR HIGH VELOCITY IMPACT
PART I THEORY AND FORMULATION; PART II PROGRAM USER'S MANUAL

CONTRACT NAS 3-18908
LOCKHEED MISSILES AND SPACE COMPANY, INC.

	<u>Copies</u>
Advanced Research Projects Agency Washington DC 20525 Attn: Library	1
Advanced Technology Center, Inc. LTV Aerospace Corporation P. O. Box 6144 Dallas, TX 75222 Attn: D. H. Petersen	1
Air Force Flight Dynamics Laboratory Wright-Patterson Air Force Base, OH 45433 Attn: Everett Bailey (TBP) G. P. Sendeckyj (FBC) L. Berke T. Norbut (TBP) R. S. Sandu	1 1 1 1 1
Air Force Materials Laboratory Wright-Patterson Air Force Base, OH 45433 Attn: G. P. Peterson (LC) S. W. Tsai (MBM) N. J. Pagano J. M. Whitney (MBM)	1 1 1 1
Air Force Office of Scientific Research Washington DC 20333 Attn: J. F. Masi (SREP)	1
Air Force Office of Scientific Research 1400 Wilson Blvd. Arlington, VA 22209 Attn: SIGL	1
Air Force Rocket Propulsion Laboratory Edwards, CA 93523 Attn: Library	1

2
Copies

Bell Aerospace Company
Buffalo, NY 14240
Attn: R. A. Gellatly

1

Bell Helicopter Company
P. O. Box 482
Ft. Worth, TX 76101
Attn: H. Zinberg

1

The Boeing Company
P. O. Box 24346
Seattle, WA 98124
Attn: R. Miller
M. Aarnes

1

The Boeing Company
Vertol Division
Morton, PA 19070
Attn: R. A. Pinckney

1

Batelle Memorial Institute
Columbus Laboratories
505 King Avenue
Columbus, OH 43201
Attn: E. F. Rybicki

1

California Research & Technology, Inc.
6269 Vaviel Ave.
Woodland Hills, CA 91364
Attn: K. N. Kreyenhagen

1

Commander
Natick Laboratories
U. S. Army
Natick, MA 01762
Attn: Library

1

Commander
Naval Air Systems Command
U. S. Navy Department
Washington DC 20360
Attn: E. McQuillen

1

Commander
U. S. Navy Department
2823 TTNS RDC
Annapolis, MD 21402
Attn: F. Braun

1

Commander
Naval Ordnance Systems Command
U. S. Navy Department
Washington DC 20360
Attn: B. Drimmer, ORD-033 1

Cornell University
Dept. Theoretical & Applied Mech.
Thurston Hall
Ithaca, NY 14853
Attn: F. C. Moon
R. H. Gallagher 1 1

Department of the Army
U. S. Army Material Command
Washington DC 20315
Attn: AMCRD-RC 1

Department of the Army
U. S. Army Aviation Materials Laboratory
Ft. Eustis, VA 23604
Attn: I. E. Figge, Sr. 1

Department of the Army
U. S. Army Aviation Systems Command
P. O. Box 209
St. Louis, MO 63166
Attn: R. Vollmer, AMSAV-A-UE 1

Department of the Army
Plastics Technical Evaluation Center
Picatinny Arsenal
Dover, NJ 07801
Attn: H. E. Pebly, Jr. 1

Department of the Army
Watervliet Arsenal
Watervliet, NY 12189
Attn: W. E. Lofensen 1

Department of the Army
Watertown Arsenal
Watertown, MA 02172
Attn: A. Thomas 1

Department of the Army
Redstone Arsenal
Huntsville, AL 35809
Attn: Library 1

4
Copies

Department of the Navy
Naval Ordnance Laboratory
White Oak
Silver Spring, MD 20910
Attn: Library

1

Department of the Navy
U. S. Naval Ship R&D Laboratory
Bethesda, MD 20034
Attn: P. Matula

1

Drexel University
32nd & Chestnut
Philadelphia, PA 19104
Attn: R. Mortimer
P. C. Chou

1

E. I. DuPont DeNemours and Co.
DuPont Experimental Station
Wilmington, DE 19898
Attn: C. H. Zweben

1

General Dynamics
P. O. Box 748
Ft. Worth, TX 76100
Attn: M. E. Waddoups

1

General Dynamics/Convair
P. O. Box 1128
San Diego, CA 92112
Attn: J. L. Christian

1

General Electric Co.
Evendale, OH 45215
Attn: C. Salemme
R. Ravenhall
S. Levy
M. L. Roberts (MD K69)
R. Stabrylla

1

1

1

1

General Motors Corporation
Detroit Diesel-Allison Division
Indianapolis, IN
Attn: M. Herman

1

Georgia Institute of Technology
School of Aerospace Engineering
Atlanta, GA 30332
Attn: L. W. Rehfield

1

5
Copies

Grumman Aerospace Corporation
Bethpage, Long Island, NY 11714
Attn: H. A. Armen, Jr.

1

Hamilton Standard Division
United Aircraft Corporation
Windsor Locks, CT 06096
Attn: W. A. Percival
R. A. Cornell

1

1

Hercules, Inc.
Allegheny Ballistics Laboratory
P. O. Box 210
Cumberland, MD 21052
Attn: A. A. Vicario

1

IIT Research Institute
10 West 35 Street
Chicago, IL 60616
Attn: I. M. Daniel

1

Illinois Institute of Technology
10 West 32 Street
Chicago, IL 60616
Attn: L. J. Broutman

1

Jet Propulsion Laboratory
4800 Oak Grove Drive
Pasadena, CA 91103
Attn: R. Levi

1

Lawrence Livermore Laboratory
P. O. Box 808, L421
Livermore, CA 94550
Attn: T. T. Chiao

1

Lockheed Palo Alto Research Labs
Palo Alto, CA 94304
Attn: B. O. Almroth

1

MacNeal-Schwendler Corp.
7442 North Figueroa Street
Los Angeles, CA 90041
Attn: R. MacNeal

1

MARC Analysis Research Corporation
260 Sheridan Ave., Suite 314
Palo Alto, CA 94306
Attn: P. V. Marcal

1

6
Copies

McDonnell Douglas Aircraft Corporation
P. O. Box 516
Lambert Field, MO 63166
Attn: J. C. Watson

1

McDonnell Douglas Aircraft Corporation
3855 Lakewood Blvd.
Long Beach, CA 90810
Attn: L. B. Greszczuk

1

Massachusetts Institute of Technology
Cambridge, MA 02139
Attn: Prof. J. F. Mandell
Prof. T. Pian
Prof. J. Mar

1

1

1

Material Sciences Corporation
1777 Walton Road
Blue Bell, PA 19422
Attn: B. W. Rosen

1

NASA-Ames Research Center
Moffett Field, CA 94035
Attn: L. Ericson

1

NASA-Flight Research Center
P. O. Box 273
Edwards, CA 93523
Attn: A. L. Carter

1

NASA-George C. Marshall Space Flight Center
Huntsville, AL 35812
Attn: R. L. McComas

1

NASA-Goddard Space Flight Center
Greenbelt, MD 20771
Attn: J. B. Mason

1

NASA-Langley Research Center
Hampton, VA 23365
Attn: H. G. McComb
D. J. Weidman
M. C. Card
M. Stein

1

1

1

1

7
Copies

NASA-Lewis Research Center
21000 Brookpark Road
Cleveland, OH 44135

Attn: Contracting Officer M.S. 500-313	1
Tech. Report Control M.S. 5-5	1
Technology Utilization, M.S. 3-19	1
AFSC Liaison, M.S. 501-3	1
Rel. and Quality Assur. M.S. 500-211	1
M&S Contract File M.S. 49-1	1
R. H. Johns, M.S. 49-3	1
C. C. Chamis, M.S. 49-3	17
Library, M.S. 60-3	1
P. Manos, M.S. 86-2	1
J. F. Kring, M.S. 86-2	1
M. T. Cunningham, M.S. 86-2	1
B. Gross, M.S. 49-1	1

NASA-Lyndon B. Johnson Space Center
Houston, TX 77001
Attn: W. W. Renegar

NASA-Headquarters
Washington DC 20546
Attn: G. C. Deutsch Code RW-3

NASA Scientific & Tech. Information Facility
P. O. Box 33
College Park, MD 20740
Attn: Acquisitions Branch

National Aeronautics & Space Administration
Office of Advanced Research and Technology
Washington DC 20546
Attn: M. I. Salkind, Code RWS-3
T. Amos, Code RWS-3

National Aeronautics & Space Administration
Office of Technology Utilization
Washington DC 20546

National Bureau of Standards
Eng. Mech. Section
Washington DC 20234
Attn: R. Mitchell

Northrop Space Laboratories
3401 West Broadway
Hawthorne, CA 90250
Attn: R. M. Verrette

Copies

National Science Foundation
Engineering Division
1800 G Street, NW
Washington DC 20540
Attn: Library

1

Pratt and Whitney Aircraft
East Hartford, CT
Attn: T. Zupnik
G. Fulton

1

Physics International Company
2700 Merced Street
San Leandro, CA 94577
Attn: D. L. Orphal

1

Purdue University
331 Grissom Hall
West Lafayette, IN
Attn: C. T. Sun

1

Rockwell International
Los Angeles Division
International Airport
Los Angles, CA 90009
Attn: L. M. Lackman

1

Sandia Corporation
Analytical Development Division, 1541
Albuquerque, NM 87115
Attn: R. E. Hickell

1

Sikorsky Aircraft Division
United Aircraft Corporation
Stratford, CT 06602
Attn: Library

1

Southwest Research Institute
8500 Culebra Road
San Antonio, TX 78284
Attn: P. Francis

1

Space & Missile Systems Organization
Air Force Unit Post Office
Los Angeles, CA 90045
Attn: Technical Data Center

1

Swanson Analysis Systems, Inc.
Elizabeth, PA 15037
Attn: J. A. Swanson

1

9
Copies

Texas A&M University
Dept. of Aerospace Engineering
College Station, TX 77843
Attn: R. A. Schapery

1

United Technologies Research Center
East Hartford, CT 06108
Attn: C. P. Van Dine

1

University Analytics, Inc.
7151 West Manchester Ave.
Los Angeles, CA 90045
Attn: E. I. Field

University of California, Berkeley
Dept. of Civil Engineering
Berkeley, CA 94720
Attn: R. W. Clough
E. L. Wilson

1

1

University of California, Los Angeles
Dept. of Civil Engineering
Los Angeles, CA
Attn: W. C. Hurty
L. A. Schmit

1

1

University of Dayton Research Institute
Dayton, OH 45409
Attn: F. K. Bogner

1

University of Delaware
Mechanical and Aerospace Engineering
Newark, DE 19711
Attn: R. B. Piper

1

University of Illinois
Dept. of Theoretical and Applied Mechanics
Urbana, IL 61801
Attn: R. W. Kim

1

University of Wyoming
Dept. of Mechanical Engineering
University Station,
Box 3295
Laramie, WY
Attn: D. F. Adams
D. W. Oplinger

1

1

University of Oklahoma
School of Aerospace Mechanical & Nuclear Engineering
Norman, OK 73069
Attn: C. W. Bert

1

10

Copies

U. S. Army Materials & Mechanics Research Center
Watertown Arsenal
Watertown, MA 02172
Attn: E. M. Lenoe

1

V. P.I. and S.U.
Dept. of Eng. Mech.
Blacksburg, VA 24061
Attn: R. H. Heller
H. J. Brinson

1
1

Westinghouse Electric Corporation
Waltz Mill Site
Box 158
Madison, PA 15663
Attn: R. H. Mallett

1